Towards measuring the microscopic origin of $1/f$-flux noise using nanowire transmons subject to a magnetic field

Elmore Vaal

Technische Universiteit Delft

TU Delft

Towards measuring the microscopic origin of $1/f$-flux noise using nanowire transmons subject to a magnetic field

by

E. Vaal

to obtain the degree of Master of Science in Applied Physics
at the Delft University of Technology, to be defended publicly on Monday August 5, 2019 at 13:00 PM.

Student number:	4310160	
Project duration:	November 1, 2018 – August 5, 2019	
Thesis committee:	Prof. dr. L. DiCarlo,	TU Delft, supervisor
	Dr. A. Endo,	TU Delft
	Dr. S. Dobrovitski,	TU Delft
	Dr. A. Akhmerov	TU Delft
Daily supervisor:	Ir. T. Stavenga	TU Delft

An electronic version of this thesis is available at `http://repository.tudelft.nl/`.

QUTech

TU Delft

Abstract

Superconducting-normalconducting-superconducting (SNS) transmons with 2-facet Al-shell nanowires are qubits compatible with magnetic fields above 10 mT. There are important correlations of the room temperature nanowire resistance with the chance of the qubit being measurable: at a resistance of $2-3\,\mathrm{k}\Omega$, the qubit is almost guaranteed to work. The chance of success halves every $2-3\,\mathrm{k}\Omega$ increase. This information can be used to increase the yield. The flux noise power spectral density (PSD) of a model spin-1/2 fluctuator has been investigated as a function of the magnetic field using the Zeeman interaction. Not only the fluctuations parallel to the magnetic field contribute, but also the fluctuations perpendicular to the magnetic field. Cross-terms cancel out. The flux noise PSD of the SQUID is a linear combination of these spin PSDs when the spins are spatially uncorrelated. The magnetic field suppresses the parallel spin-axis noise PSD contribution as $\cosh^{-2}\left(\frac{\mu_B B}{k_B T}\right)$. The magnetic field changes the perpendicular spin-axis PSD contribution due to the Larmor precession frequency peak $2f_Z \sim \mu_B B$, but does not influence the PSD contribution at frequencies higher that the Larmor precession frequency. When rotational asymmetry in the SQUID geometry is present, the PSD contributions of the perpendicular and parallel components can be separated.
In our setup, a perpendicular coil is used to align the magnetic field with the transmon plane. The alignment procedure of maximizing the resonator frequency vs. the perpendicular coil field has been verified. To measure the flux noise, the perpendicular coil is first used to change the flux bias by large amounts. Then a dedicated flux bias is used to make a fine-grained sweep over the flux without flux-jumps, to calibrate the magnetic field at the SQUID. We have found a signal of the flux noise at zero field and at field. A flux noise amplitude of $\sqrt{A} \sim 1000\,\mu\Phi_0$ has been found at zero magnetic field.

Contents

1 Introduction 7
1.1 Qubits. . . . 7
1.2 Transmons 7
1.3 Qubit-resonator coupling 8
1.4 Resonator readout 8
1.5 Qubit tunability through a flux bias 8
1.6 Flux noise 9
1.7 Goal and outline of thesis 9

2 Nanowire transmon with an in-plane magnetic field 11
2.1 Why nanowires?. . . . 11
2.2 SNS junction Hamiltonian 12
2.3 SNS Hamiltonian in a magnetic field 12
2.4 Alignment to transmon plane 12
2.5 Qubit coherence at field. . . . 14
2.6 Qubit at an in-plane magnetic field angle 15
2.7 Second qubit in an in-plane magnetic field at an angle 17
2.8 Alignment during an angle scan. . . . 19

3 Flux noise and its microscopic origin 23
3.1 Introduction 23
3.2 History of flux noise. . . . 23
3.3 Measurements of flux noise 24
3.4 Possible microscopic origins of the flux noise 24

4 Spin fluctuator noise in a magnetic field 27
4.1 Coupling of the spin fluctuations to the SQUID flux. . . . 28
4.2 Spin fluctuator model 28
4.2.1 Power spectral density of $S_{zz}(f,B)$ 29
4.2.2 Power spectral density of $S_{xx}(f)$ 30
4.2.3 Other (cross-)spectra. . . . 33
4.3 Ensemble of fluctuators 33
4.4 The flux vector $\mathbf{F}$ 34
4.5 The nature of flipping rates 36
4.6 Tying everything together: a $S = 1/2$-electron example 36
4.7 Further research and outlook 37

5 Flux tunable nanowire transmon in a magnetic field 39
5.1 Flux tunability 40
5.1.1 Method for determining a quickly changing qubit frequency 40
5.1.2 Flux tunability at field 41
5.2 Stable magnetic fields: magnet current source noise 42
5.3 Measurement of a continuous frequency arc vs. flux 44
5.3.1 Flux jumps 45
5.3.2 Flux jumps due to a superconducting loop in the system 45
5.3.3 Flux jumps due to a vortex in the superconductor 47
5.4 Flux noise measurements 47

6 Statistical analysis of nanowire junction room temperature resistances 49
6.1 Data analysis . . . 49
6.2 Probability distribution of resistances . . . 50
6.3 Prediction of qubit measurability . . . 51
6.4 Batch differences . . . 52
6.5 Effect of airbridge fabrication . . . 53
6.6 Effect of aging . . . 54
6.7 Other effects . . . 54
6.8 Further research . . . 55

7 Conclusions and prospects 57
7.1 Future research . . . 58

Bibliography 61

A Nanowire transmon physics 65
A.1 Nanowire subband Hamiltonian . . . 65
A.2 Possible measurements using a (nanowire) transmon . . . 66

B Experimental setup 67
B.1 Magnets and magnet current sources . . . 68
B.2 Magnet current source upgrade . . . 68
B.3 Qubit device . . . 69

C Chip design 71
C.1 Shape of the resonator transmission . . . 71
C.1.1 Measuring the coupling quality factor . . . 71
C.2 Chip design . . . 73
C.2.1 Abrikosov vortices . . . 73
C.3 Targeting the coupling quality . . . 74
C.4 Finalized chip design . . . 75

D Multiple damped oscillator Ramsey analysis 77
D.1 Finding f_i and T_i . . . 77

E Collection of chip design parameters 79

F Derivation of the spin-fluctuator spectrum 83

G Derivation of the linear spectrum contributions of the spin PSD 85

H Derivation of the Flux vector F 87

I Derivation of the ensemble of spin fluctuators PSD 89

J Magnet use: issues and step-by-step checklist 91

1 Introduction

The basic building blocks for scalable quantum computers are being developed right now. The building block is the prototypical qubit. While an ideal qubit is a simple system to explain, it doesn't paint the full picture: there are many noise sources that break the carefully prepared state of a qubit. We can split these up in relaxation processes, where energy loss happens, and dephasing processes, where phase information is lost. This is still a limiting factor for fault-tolerant quantum computing. The current state-of-the art circuit quantum electrodynamics (cQED) devices relax in timescales of $\sim 100\,\mu s$ and decohere in timescales of $\sim 100\,\mu s$.
Coherence of the prepared state is essential for multiple-qubit gates, which can create entanglement, a necessary ingredient for quantum speedup over classical algorithms. This coherence for superconducting devices using Superconducting QUantum Interference Devices (SQUIDs) is currently limited by flux noise in superconducting rings, in which a flux can determine the qubit energy spectrum, which is necessary for a scalable quantum chip. There have been investigations on the origin of this noise to be able to suppress it [6],[39],[27]. As of writing the thesis, its origin has not been shown conclusively. This thesis aims to determine the effects of a magnetic field on the flux noise by using a nanowire SNS junction [33], so that we can rule out or gain confidence in the proposed noise models.

1.1. Qubits

The qubit is the basic building block of a quantum computer, just as a bit is the basis for a (classical) computer. A qubit can be seen as a system with two levels (just like a bit), undergoing quantum mechanics. What this means is that the qubit can be in the $|1\rangle$ and the $|0\rangle$ state, like a normal bit. However, the qubit can also be a complex linear combination of these two, so we can write them as:

$$\big|\psi\big\rangle = a\,|0\rangle + b\,|1\rangle$$

where $a, b \in \mathbb{C}$ complex numbers satisfying $|a|^2 + |b|^2 = 1$. The energy required to excite the qubit from the $|0\rangle$ state to the $|1\rangle$ state is denoted at $E_{01} = \hbar\omega_{01} = h f_{01}$.

1.2. Transmons

A transmon can form a qubit following the theory of circuit quantum electrodynamics. The prototypical transmon can be modeled as in [24] by the following Hamiltonian

$$\hat{H} = 4E_C(\hat{n} - n_g)^2 - E_J\cos\big(\hat{\phi}\big) \tag{1.1}$$

where E_C is the charging energy given by the capacitance betweeen the transmon pads, $\hat{n}$ is the number of Cooper pairs transferred between the leads, n_g is the charge offset in the system and E_J is the Josephson junction energy. The ϕ is the phase difference between the wavefunctions of the two superconducting leads $\psi_1 \propto e^{i\phi_1}$ and $\psi_2 \propto e^{i\phi_2}$. We can also write $\hat{n}$ as $-i\frac{\partial}{\partial\hat{\phi}}$ so that the commutation relation $[\hat{\phi}, \hat{n}] = i$ holds.
This Hamiltonian is solvable in the limit $\hat{\phi} \to 0$ and the transmon requirement $E_J \gg E_C$. In this regime, any charge (offset) noise n_g effect on the energy levels is exponentially suppressed. The found energies for the

m'th energy level is

$$E_m \approx -E_J + \left(m + \frac{1}{2}\right)\sqrt{8E_C E_J} - \frac{E_C}{12}(6m^2 + 6m + 3) \qquad m = 0, 1, 2, 3, \ldots \tag{1.2}$$

From this equation, a couple of important parameters can be deduced. The qubit excitation energy $E_{01} = E_1 - E_0 \approx \sqrt{8E_C E_J} - E_C$ and the 0-2 transition energy $E_{02} = E_2 - E_0 \approx 2\sqrt{8E_C E_J} - 3E_C = 2(E_{01}) - E_C$. The energies E_{01} and $E_{02}/2$ need to be different, such that we do not excite higher modes using the same frequency.

1.3. Qubit-resonator coupling

To read out the qubit, we need to connect it to a more accessible system for readout than the state of a plasmon. We do this by coupling the transmon capacitively to a resonator. A natural choice is the $\lambda/4$ quarter-wave resonator, since it is smaller in length than a full wavelength resonator and its properties are well understood. This coupling can be represented by the Jaynes-Cummings Hamiltonian[36]

$$\hat{H}_{JC} = \hbar\omega_q \frac{\sigma_z}{2} + \hbar\omega_r(\hat{a}\hat{a}^\dagger + \frac{1}{2}) + \hbar g(\hat{a}\sigma_+ + \hat{a}^\dagger\sigma_-) \tag{1.3}$$

where $\omega_q = \frac{E_{01}}{\hbar}$ from the transmon energy levels found in Section 1.2, ω_r is the resonant frequency of the resonator, g the coupling constant dependent on the capacitance between transmon and resonator and $\hat{a}$ ($\hat{a}^\dagger$) is the annihilation (creation) operator for the bosonic photons in the resonators.
To determine the effects of the qubit on the resonator frequency, we apply the rotating wave approximation (RWA) which implies the requirement that $\Delta = |\omega_q - \omega_r| \ll \omega_q + \omega_r$. We also assume we are in the dispersive limit ($g \ll \Delta$). These imply that the coupling constant must be smaller than typical qubit and resonator frequencies, while also being smaller than the difference of the qubit and resonator frequencies. Using these assumptions, we can solve the Hamiltonian to give the resonator frequency in the rotating frame which shifts depending on the state of the qubit following

$$\omega_{r,load} = \omega_{r,unload} \pm \frac{g^2}{\Delta} \tag{1.4}$$

where $\omega_{r,unload}$ is the resonator frequency were there no qubit. The $\pm$ differs given by the state of the qubit. This means that measuring $\omega_{r,load}$ indicates the state of the qubit. However, even if the qubit frequency is low such that $\frac{\omega_q}{\omega_r} < 0.5$ and the RWA does not apply anymore, the resonator still experiences a shift depending on the qubit state[58].

1.4. Resonator readout

We use the resonator as a way to read out the state of the qubit. We first find the resonator without interacting with the qubit. This is the resonator frequency when the qubit is in the ground state. We now realize that the dispersive shift is dependent on the qubit state. So when the qubit is excited, the resonator frequency changes. We keep reading out at the ground state resonator frequency, but now we are resonating less effectively. This can be seen in the transmission, as less power is retained in the resonator. Qualitatively, the resonator would perform better when the dip in the transmission is as close to 0 as possible. Then the response for a dispersive shift is large. However, sometimes the dispersive shift is small, and for that we want to make the dip as thin as possible, so that the sensitivity become larger. We can tune both of these things as will be discussed in Section C.

1.5. Qubit tunability through a flux bias

First of all, to make a quantum computer with many qubits, we could make all the qubits a fixed frequency, spaced evenly from each other. We could use a method called cross-resonance to create 2-qubit gates. However, due to imprecision in fabricating the qubit frequency and stringent requirements on the relation of two qubits interacting with each other, this method is not scalable. A solution is to be able to tune the frequency of the transmon by adding a SQUID. A SQUID is a superconducting loop that houses two Josephson junctions, one on each branch of the loop. The current changes in the junctions as a function of the flux penetrating the SQUID. A current flows through the junctions to maintain flux quantization, creating a flux bias on a SQUID. This can be used to tune the qubit frequency to a desired frequency. To find out the qubit transmon

Hamiltonian of two Josephson Junctions in a SQUID loop, we write:

$$\hat{H} = 4E_C\hat{n}^2 - E_{j1}\cos(\phi_1) - E_{j2}\cos(\phi_2) \tag{1.5}$$

where E_C is the charging energy, E_{j1}, E_{j2} the Josephson energies of junction 1 and junction 2 respectively and ϕ_1 and ϕ_2 the gauge invariant phase differences of the superconductor wave function for junction 1 and junction 2. For a SQUID loop, the flux quantization constraint dictates that $\phi_1 - \phi_2 = 2\pi n + 2\pi\frac{\Phi}{\Phi_0}$ with $\Phi_0 = \frac{h}{2e} \approx 2.07 \cdot 10^{-15}$ Wb We can rewrite the equation as [24]

$$\hat{H} = 4E_C\hat{n}^2 - E_{j,tot}\cos\left(\frac{\pi\Phi}{\Phi_0}\right)\sqrt{1 + d^2\tan^2(\frac{\pi\Phi}{\Phi_0})}\cos(\hat{\phi} - \phi_0) \tag{1.6}$$

where $d = \frac{E_{j1}-E_{j2}}{E_{j1}+E_{j2}}$ is the energy asymmetry, $E_{j,tot} = E_{j1} + E_{j2}$ the equivalent Josephson energy, $\hat{\phi} = \frac{\phi_1+\phi_2}{2}$ the phase operator and $\phi_0 = d\tan\left(\frac{\pi\Phi}{\Phi_0}\right)$ the offset phase. This method has as advantage, that we can tune the frequency reliably by sending a flux bias through the SQUID. Also, we can create 2-qubit gates called conditional phase gates with flux pulses[14]. However, a disadvantage of this qubit is the additional unknown flux noise that the SQUID exhibits, which limits coherence when $\phi \neq \phi_0$.

1.6. Flux noise

Flux tunable transmons and flux qubits are currently being limited by flux noise. Qubit control can still be improved by having more accurafte and faster hardware, but there are limitations inherent to the fabrication of the qubit itself. The effects can often be measured by the T_1 and T_2 times of the qubit, called the relaxation and decoherence time respectively. Relaxation is caused by loss of the excited state of the qubit due to loss channels. Energy can be exchanged with these channels at the qubit frequency. The decoherence time can be split into two contributions[38, 48]:

$$T_2^{-1} = T_\phi^{-1} + (2T_1)^{-1} \tag{1.7}$$

where T_ϕ is the dephasing time. So not only is the coherence time dependent on the relaxation, the qubit is also affected due to the phase changing undesirably. The phase evolution is dependent on the qubit frequency. Thus dephasing is an effect of the qubit frequency fluctuating [34]. In a flux tunable transmon, there are be several ways that this could happen. The main effect investigated is the flux noise, due to fluctuations in the magnetic field as sensed by the SQUID. Other effects would be photon number fluctuations in the resonator or the critical current noise of the Josephon junction. This SQUID is used by the qubit as a knob to tune the qubit frequency, so any noise in the sensed magnetic field creates noise in the flux measured by the SQUID and thus creates fluctuations in the qubit frequency. Ideally these noise sources do not increase the dephasing such that $T_\phi \ll 2T_1$, making the T_2 be $2T_1$-limited. Qubits are preferentially used at the sweetspot: the flux bias where the qubit frequency is first-order insensitive to the flux. During two-qubit gates, flux pulses are used to tune the qubits frequencies off-sweetspot and the qubit coherence times will decrease to flux noise. This can limit the 2-qubit-gate fidelity [8]. Our nanowire transmons have the possibility of being voltage tunable using a voltage bias gate, or being flux tunable by embedding the wire in a SQUID. Of these two, only the flux tunable transmon is sensitive to flux noise.[33]. More on the flux noise will be covered in Section 3.

1.7. Goal and outline of thesis

This thesis project had as goal measuring the $1/f$-flux noise of a flux tunable nanowire transmon as a function of the magnetic field to try to gain more information about the microscopic origin of the this $1/f$-flux noise.
The thesis is structured as follows:
In Section 2 we look at a nanowire transmon (not flux tunable) in a magnetic field, and look at the behaviour of these transmons at an angle.
In Section 3 we discuss what flux noise is, what might be its microscopic origin and how we would measure the flux noise with nanowire transmons.
In Section 4, a model of a noisy spin near a SQUID in a magnetic field is described. An extensive example is worked out for the flux noise caused by an ensemble of spin 1/2-particles on the SQUIDs surface in a magnetic field due to the Zeeman interaction.
In Section 5, a flux tunable nanowire transmon in a magnetic field is discussed. We explore several obstacles

and find a way around them.
In Section 6, we try to find the cause of the low yield of qubits by using room temperature resistance data from chips fabricated in the period January 2018 to June 2019.
In the Appendix, other topics are handled, such as the measurement setup, the chip design, tabulated chip design parameters and several derivations for the spin fluctuator example.

2

Nanowire transmon with an in-plane magnetic field

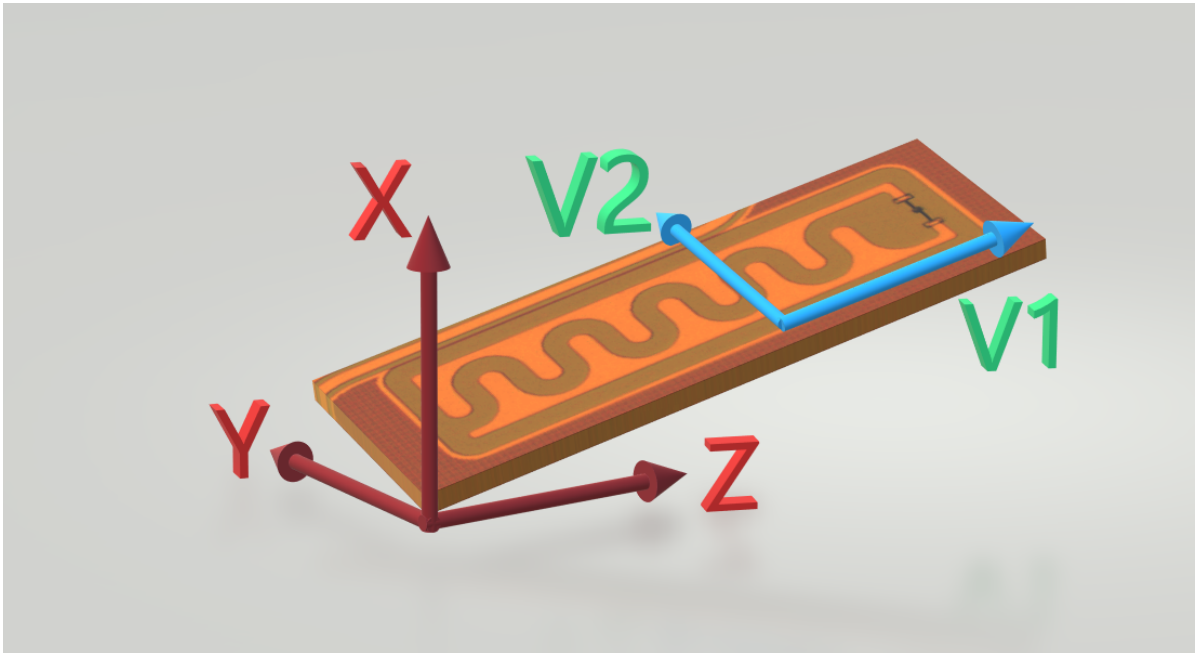

Figure 2.1: The coordinate system used to control the magnetic field. X refers to the axis in the direction of the perpendicular coil, which is also used as a qubit flux bias. Y and Z correspond to two physical magnets axes controlling the in-plane magnetic field. Due to misalignment with this plane (exaggerated in this figure), we find virtual vectors $V1$ and $V2$ and use them to control the field to prevent an out-of-plane magnetic field component.

Applying an in-plane magnetic field to the transmons requires careful alignment to maintain measurable qubits. In the following sections, we will demonstrate the alignment procedure while ramping the magnet fields and showing T_1 and T_2-times during ramping.

2.1. Why nanowires?

The conventional SIS junctions described in Section 1.2 are incompatible with high magnetic fields. Only fields of 10 mT are sustained by the typical Al-AlOx-Al junctions. One solution is to use a superconducting-normal conducting-superconducting (SNS) junction, where due to Andreev bound states (ABS), there is a transmission of Cooper pairs through the normal conducting material. However, a typical metal has a continuum of states, which causes a near infinite amount of conductance channels for the ABS, which facilitates dissipation. So we would like to use systems in which there is a limited number of conductance channels

available. One such system is a semi-conducting nanowire. Nanowires have been investigated for their interesting effects coming from their 1D nature. Their diameters are usually on the order of (tens of) nanometers. Due to the semiconductor gap, no states are available, except for states caused by the one-dimensionality of the nanowire. These states create the lateral energy quantization of the electrons travelling through the nanowire. This is further explored in Section A.1. The nanowires we use are InAs nanowires, since they can form Schottsky-barrier-free contacts providing high electron transparency.

2.2. SNS junction Hamiltonian

The nanowire can be described by the charging energy E_C created on a transmon chip and the Josephson energy E_J described by the Superconducting-Normalconducting-Superconducting (SNS) junction. Instead of Equation (1.1), we generalize the Hamiltonian to

$$H = 4E_C(\hat{n} - n_g)^2 + V(\hat{\phi}) \tag{2.1}$$

where the Josephson energy in a few-channel (N small), ABS dominated regime is given by [33]

$$V(\hat{\phi}) = -\Delta \sum_{i=1}^{N} \sqrt{1 - T_i \sin^2(\phi^2/2)} \tag{2.2}$$

where T_i is the transmission coefficient for each channel, which is determined by the density of quasiparticles present in the nanowire and other scatterers present. ϕ is the phase difference between the superconducting leads and Δ is the superconducting gap of the proximitized nanowire.

2.3. SNS Hamiltonian in a magnetic field

Due to the in-plane magnetic field, the Andreev Bound state (ABS) energies will follow Equation (2.2) where in this case, we find that the superconducting gap closes as $\Delta = \Delta(B_{||})$. For BCS superconductors, far below the critical temperature ($T \ll T_c$), this takes the form [44]

$$\frac{\Delta(B_\parallel)}{\Delta_0} = \frac{E_{ABS}(B_\parallel)}{E_{ABS}(B=0)} \approx \sqrt{1 - \left(\frac{B_\parallel}{B_c}\right)^2} \tag{2.3}$$

where B_c is the critical field and $B_{||}$ is the applied in-plane field. From Equations (2.3) and (1.2) we can find

$$f_{01}(B_{||}) \approx \frac{\sqrt{E_C E_J}}{h}\left(1 - \left(\frac{B_\parallel}{B_c}\right)^2\right)^{1/4} - \frac{E_C}{h}. \tag{2.4}$$

2.4. Alignment to transmon plane

The chip and magnets might be misaligned during processing and installing the qubit chip onto the PCB or in the fridge, see Figure 2.1. Ideally, the chip lies in the YZ-plane. Otherwise, when ramping in the Y or Z direction, we could misalign the field and cause a perpendicular field $B_\perp$ on the superconducting CPW and superconducting pads of the transmon. Above a critical field, these will form Abrikosov vortices, trapping flux and lowering the Q_i. We want to prevent this from happening. One solution is adding holes in the resonators as described in Section C.2.1, increasing the critical field before vortices are formed. However, this alone does not prevent vortices at a perpendicular field on the order of 10 mT or less[2], due to focusing of the field.
Another way to prevent a perpendicular field, is using the flux bias coil as a magnet in the X-direction to correct for this, instead of only as a flux source. A couple of resonator variables are affected by the perpendicular field: the resonator frequency f_{res} and the Q_i. Sweeping the X-magnet vs. the Q_i to find a X-field of maximum Q_i fails, since every sweep, a couple of vortices are formed every time the field is swept, which are irreversible to a certain extent[9]. Another method is to sweep the X-field vs. the resonator frequency f_{res}, which is more sensitive to any perpendicular field, as visible in Figure 2.2. While a good parabole-like dependence is visible, we also see jumps due to vortex formation.

In Figure 2.3 we can see this alignment procedure for a rampup. For the other rampups and rampdowns, the trend is similar. We can conclude that the resonator frequency is aligned. Also, when the resonator frequency is measured afterwards, it is on or near the measured maximum of the parabola. In Figure 2.4 a rampup and rampdown of the field is depicted, where for every in-plane field strength, we show the swept values of the perpendicular coil, and the best aligning perpendicular coil current, maximizing the resonator

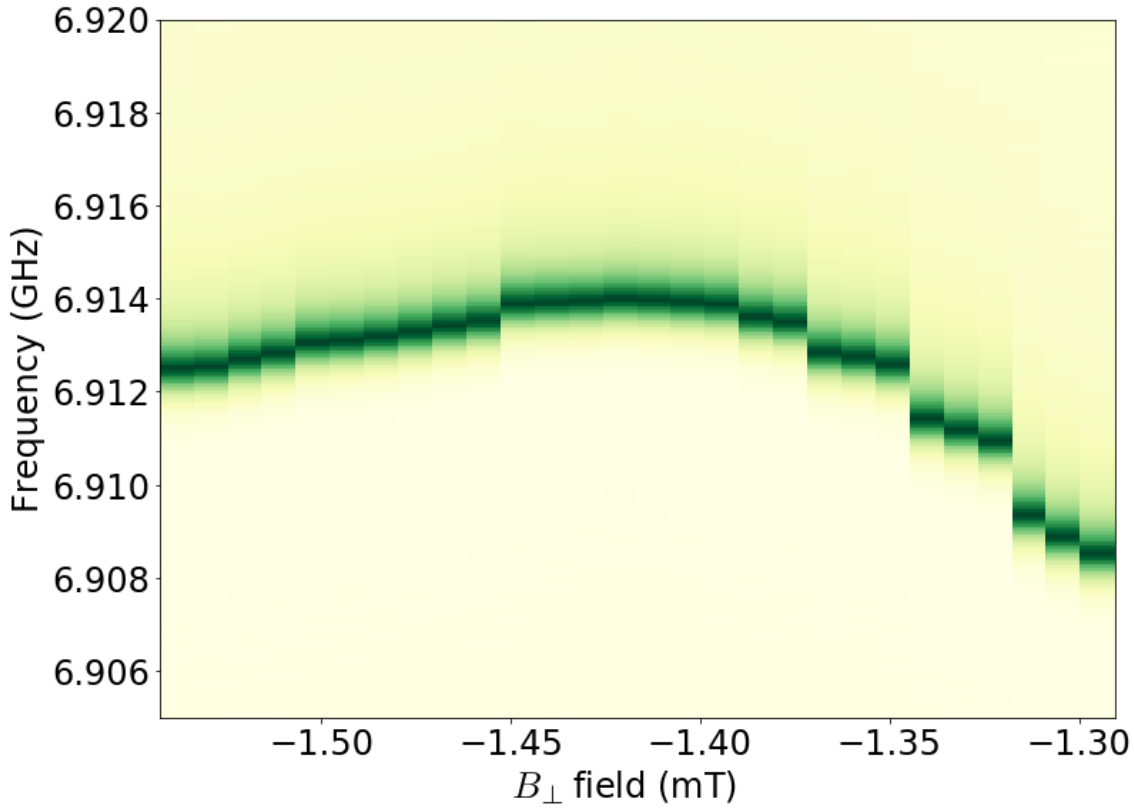

Figure 2.2: The resonator frequency as a function of the flux bias coil serving as X-axis magnet. This is a snapshot during ramping down the second time and was at an in-plane field of 245 mT. We can see a clear maximum.

frequency. There are interesting features visible. At first, we see that during the rampups, no misalignment seems present until a certain threshold field, $\sim 50-120$ mT for this rampup (and around 100 mT – 200 mT in general). After that the aligning field changes a lot. Since rampup and rampdown are done on a resonator in the middle of the chip. For another rampup and rampdown on the same chip, but on a resonator on the side we can see that the directions of the misalignment changes. This might be due to an inhomogeneous field as the perpendicular coil is smaller than the chip.
The misalignment, were it geometrical, would be $\tan(\theta) \approx \frac{2.5\,\text{mT}}{250\,\text{mT}} \rightarrow \theta = 0.6°$ for the visible rampup and $\tan(\theta) \approx \frac{-1.5\,\text{mT}}{250\,\text{mT}} \rightarrow \theta = -0.3°$ for the other rampup.
When ramping down, we get a feature, where the optimal aligned X-magnet strength goes even further up than before. After that then goes down linearly as expected until it crosses $B_X = 0$ and even shoots over to $\pm 500\,\mu$T. These two effects might be due to hysteresis effect in the resonator due to the magnetic field or due to flux trapping.

The most important question is: does the alignment actually prevent vortices to form in big numbers? Measuring the Q_i of the resonator in question suggests: yes. This is shown in Figure 2.5 the aligned resonator. On different rampups and rampdowns we find $\frac{Q_{i,before}}{Q_{i,after}} \approx 1.5$.
However in Figure 2.6 we see a the Q_i of a selected group of resonators, and it seems the X-magnet produces an inhomogeneous field and as such, aligning one resonator does not align the field for all resonators. The numbering follows the convention as shown in Figure B.2. Resonator 6 and 8 retain their Q_i after rampup and rampdown. They are spatially close to the aligned resonator (resonator 6). Resonator 1 and resonator reside on the edges of the chip and are the furthest away from the aligned resonator (resonator 6). The Q_i drops as a result. We also did the experiment aligning on a resonator on the edge (not shown). We saw that the resonator closest retain their Q_i and the resonator furthest do not. Due to this, we cannot ramp up to one qubit aligning on a neighbouring resonator, ramp down again and ramp up on another qubit without decreasing its Q_i and the goodness of readout. A solution to decrease the inhomogeneity, is to increase to coil diameter

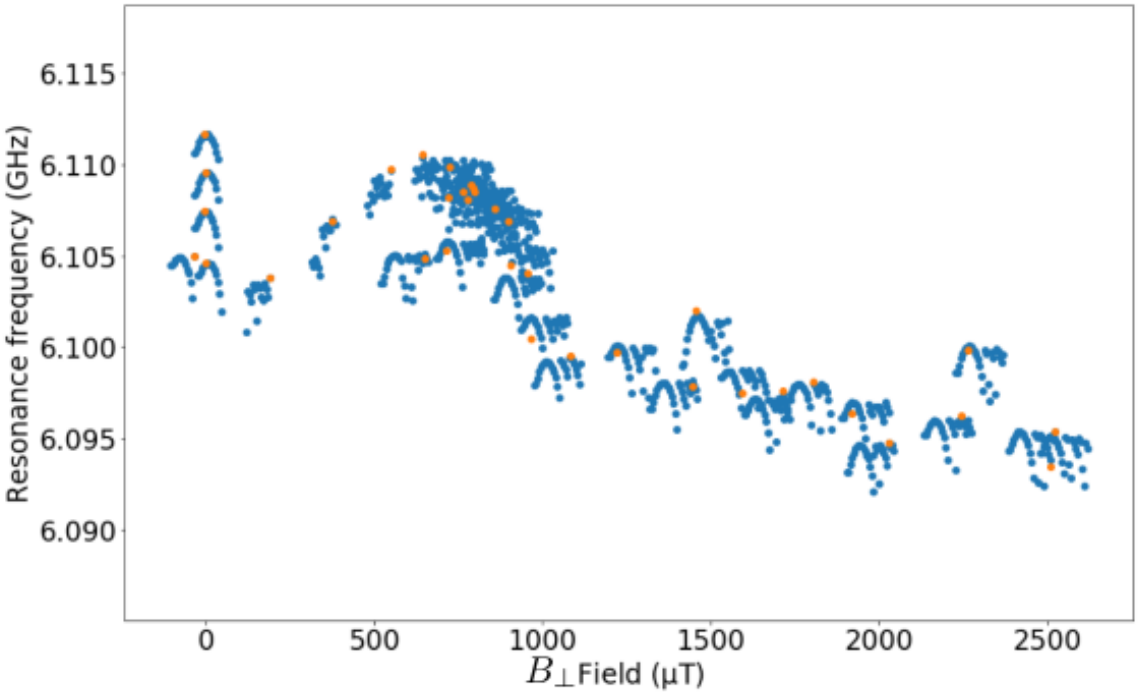

Figure 2.3: The resonator frequency frequency as the X-magnet field is swept for every field ramped to a rampup. Clear parabolas are visible for every field strength The orange dots are the resonator frequencies after setting the X-coil to the maximum before starting qubit spectroscopy.

of the perpendicular coil.

2.5. Qubit coherence at field

After aligning to resonator to ensure a purely in-plane field, we can measure the qubit. We will combine equation (2.3) and (2.1) to fit the qubit frequency spectrum numerically. The qubit frequency is shown in Figure 2.7. We have also found the anharmonicity to be a constant −90 MHz during rampup and −120 MHz during rampdown.

After a rampup to 250 mT, the qubit frequency spectrum follows a BCS-like line, as described in Equation (2.3) and the $f_{02}/2$-transition only contained one peak. The anharmonicity only drifts about 5% while ramping down. Between the first and second rampup, the sample was recondensed.

During second rampup and rampdown, the qubit frequency response stayed similar during rampup and rampdown, no qubit frequency jumps were observed. The spectrum looked similar to the BCS fit of the first rampdown, with a different starting frequency.

From Figure 2.8, we can see the relaxation and coherence times for different rampups and rampdowns to 250 mT. These have similar features, which we will address individually. First of all, the most important thing to deduce from the plots is that we still can measure coherence, even at 250 mT. At 250 mT, we can measure a clear T_2^* of $\sim$ 200 ns. We also notice that during both rampups, a significant drop in T_1, T_2^e and T_2^* appears at around 100 mT . We do not know why this happens, but it may be misalignment due to the nanowire not being completely parallel to the V_1-axis as we see during the angle scan.

We also see a return of the coherence at 200 mT (rampup 1) or 160 mT (rampup 2). We do not know what is the cause of this.

During the rampdowns, we see an increase in the coherence and relaxation times until it reaches $\sim$ 50 mT and the T_1, T_2^e drop again, even to zero field. We also do not know the origin of this process.

Another interesting aspect is the ratio of T_1 to T_2^e, in which we see that $T_1 > T_2^e$ for fields $B_{||} < 100$ mT and $T_1 = T_2^e$ for $B_{||} > 200$ mT. The exact moment of crossing over lies in between 100 mT $< B <$ 200 mT, but differs every rampup or rampdown. However, T_2^e is not $2T_1$-limited yet.

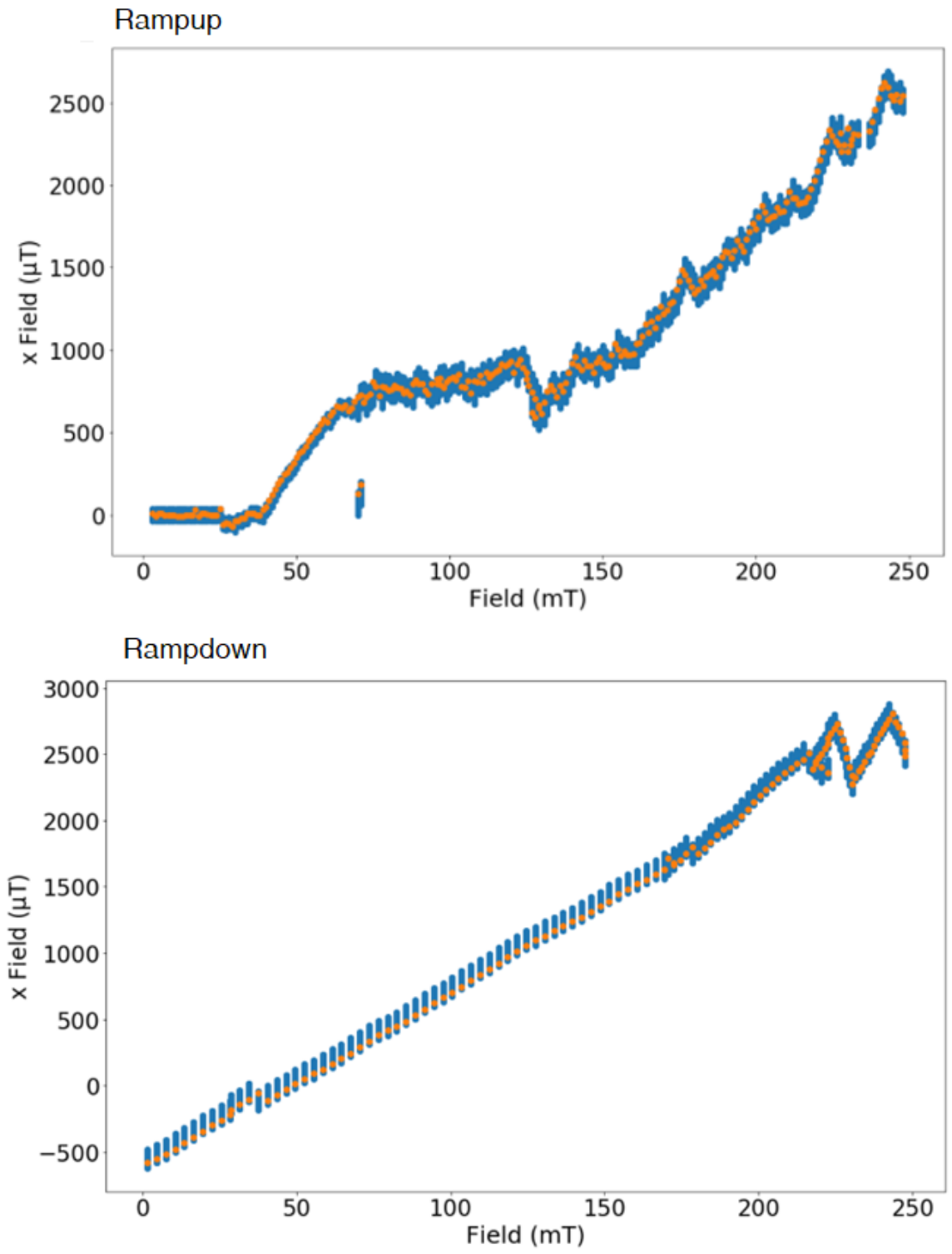

Figure 2.4: The orange dots are chosen as the maximum of the parabolas as shown in Figure 2.3. From top to bottom: Rampup 1 (aligned on resonator 6), Rampdown 1, Rampup 2 (aligned on resonator 10), Rampdown 2.

2.6. Qubit at an in-plane magnetic field angle

After ramping up the field in the $V1$-direction (as defined in Figure 2.1), we might be interested if other physical effects happen in the $V1-V2$-plane, since the nanowire is not rotationally symmetric in this plane. Turning on the Y-magnets, we ramp up to 25 mT and scan from $\Theta = -90°$ to $\Theta = +90°$ with Θ being the left-handed

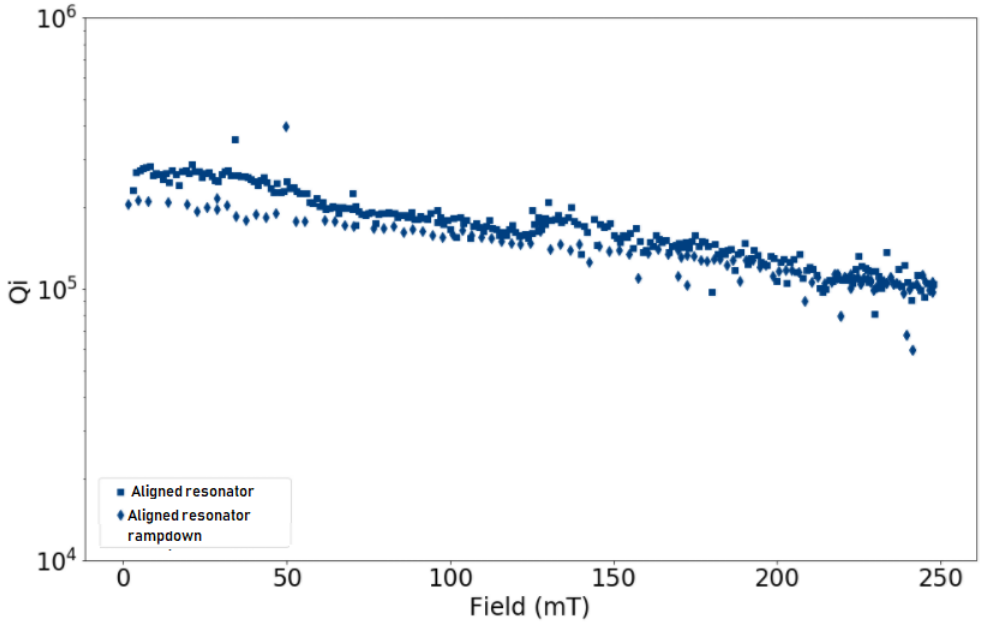

Figure 2.5: The Q_i of the resonator on which was aligned during rampup and rampdown to 250 mT.

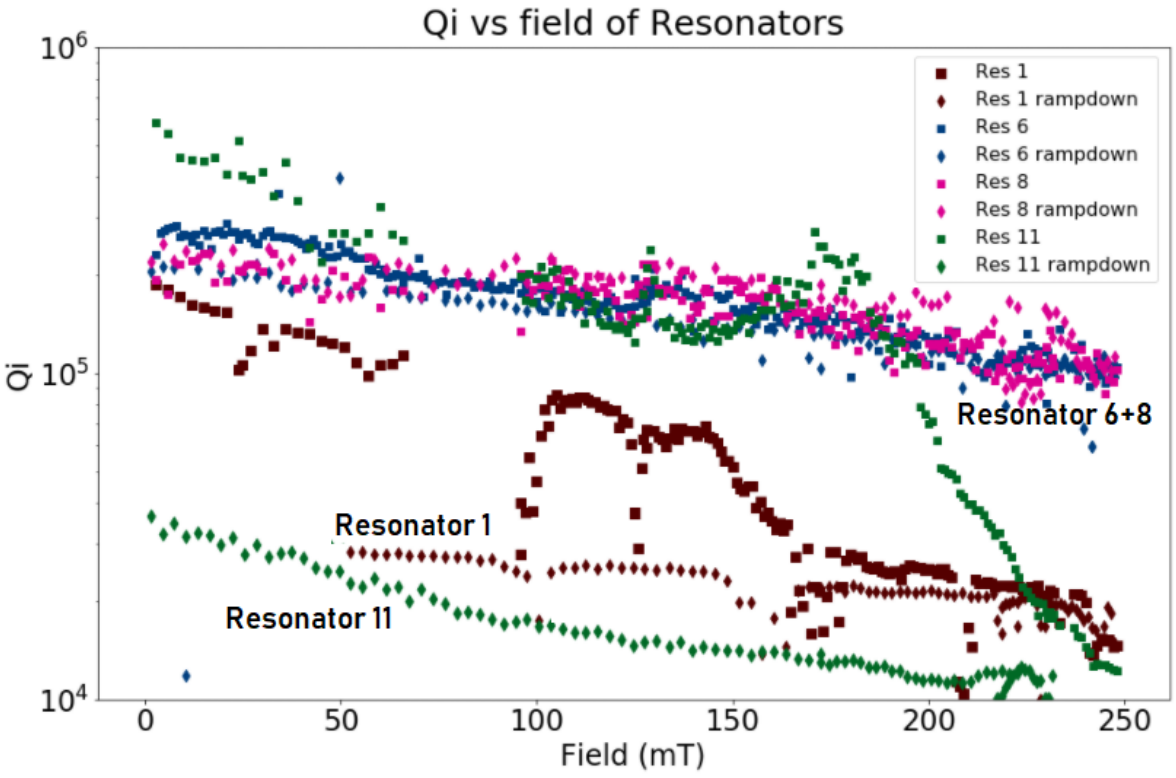

Figure 2.6: The Q_i's of selected resonators during rampup and rampdown, while being aligned on resonator a resonator in the middle of the chip. See Figure B.2 for the numbering convention.

angle to $V1$ in the $V1-V2$-plane. Angles below $-90°$ and $+90°$ were not possible to measure due to time constraints. However, it is expected that these measurements are similar to the measured semi-circle due to mirror-symmetry.
The alignment, as has been described in Section 2.4, has been done while ramping up and while sweeping the angle, to ensure V_1 and V_2 were correctly defined at every measurement.

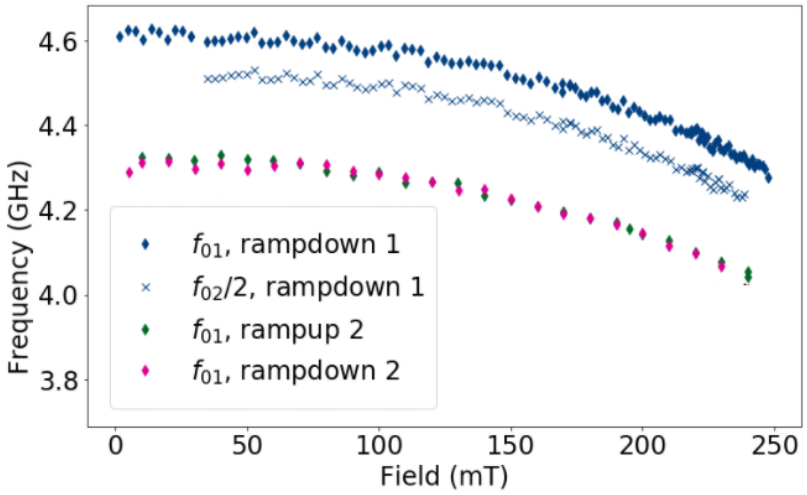

Figure 2.7: Results for the measured qubit f_{01} (diamonds) and $f_{02}/2$ (crosses) frequency as a function of the field for different rampups and rampdowns aligning the X-coil to different resonators. The first rampup and rampdown to 250 mT is aligned on a resonator in the middle (resonator 6). The second rampup and rampdown is aligned on a resonator on the edge (resonator 10).

The nanowire transmon measured had the nanowire nearly perfectly parallel to the $V1$-axis with an error of $\Theta = 0.57°$, as visible in Figure 2.9. It was designed as a flux tunable qubit, but it was not flux tunable.
In Figure 2.10 the results of the qubit frequency as a function of the angle is shown. We find that the qubit frequency is influenced by the angle at which the in-plane field is applied. With the field parallel to the nanowire (and in this case direction $V1$, so $\Theta \approx 0$), we find a maximum of the qubit frequency. We also discern certain dips at which the qubit is not measurable due to peak broadening. Here we cannot perform time domain measurements. I do not know the origin of these dips, however they are visible in a previous rampup on another chip as well. The $f_{02}/2$ frequency peak is only measurable for a limited range of angles most parallel to the nanowire. The anharmonicity is constant to within 5%, and might correlate with f_{01} (not shown).
As for the time domain relaxation and dephasing measurements of the qubit graphed in Figures 2.11 and 2.12, we again see that there is an optimal angle for every field strength to optimize the the coherence. This angle varies from $\Theta = -5°$ to $+10°$. The coarse resolution of the angle scan poses limits on knowing the best T_1 possible at higher fields, but is at least $\geq 6\,\mu$s at 100 mT.
Measurements of T_2^* shows a similar trend, except that for 25 mT, a double beating pattern can be observed and extracted $T^*_{1,split}$ are correlated with the Δf_{split} of the fit with the two exponentially damped oscillator fits (see Appendix D).
A double beating pattern could not be observed after the first dip.

2.7. Second qubit in an in-plane magnetic field at an angle

Another fine-grained 360° angle scan has been made to make sure we have cylindrical symmetry. We find that this symmetry is broken. To determine the qubit frequency at the magnetic field, we find that the critical field is not the same at every angle, due to the rotational asymmetry of the nanowire. This means it will be angle dependent and Equation (2.3) will be described approximately by

$$f(B,\theta) = f(B=0)\left(1-\left(\frac{B}{B_c(\theta)}\right)^2\right)^{1/4} \tag{2.5}$$

This means we can characterize the critical field by

$$B_c(\theta) \approx \frac{B}{\sqrt{1-\left(\frac{f(B,\theta)}{f(B=0)}\right)^4}} \tag{2.6}$$

In Figure 2.13 we see that the qubit frequency peaks when it is aligned with the nanowire axis at an in-plane angle $\theta_0 = -11°$ to $V1$. This is due to the Meissner effect having less of an effect on the Al-shell head-on. We

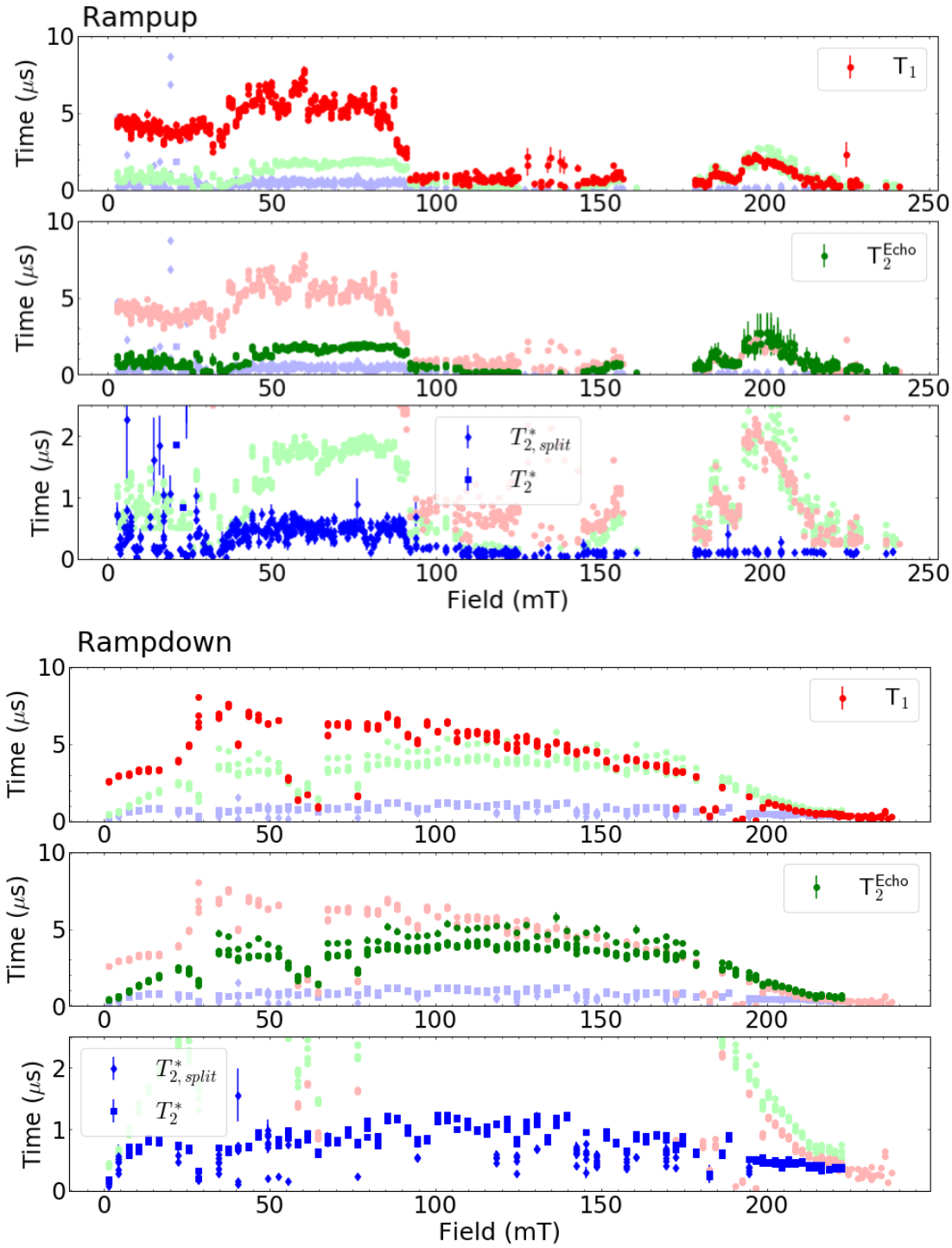

Figure 2.8: Collection of T_1, T_2^E and T_2^* measurements as a function of field for different rampups and rampdowns. The first rampup and rampdown is a sweep from 0 to 250 mT while using the alignment procedure. Both plots are divided in three plots to clearly separate the values of T_1, T_2^e and T_2^* during that rampup or rampdown.

also see an asymmetry for angles θ and $\pi-\theta$. This might be a result of the 2-facet shell facing only one side. We capture this phenomenologically through the equation:

$$f(B,\theta) = f(B=0)\left(1-\left(\frac{B\cos(\theta-\theta_0)}{B_{c,good}}-\alpha_{good}\right)^2-\left(\frac{B\sin(\theta-\theta_0)}{B_{c,bad}}-\alpha_{bad}\right)^2\right) \tag{2.7}$$

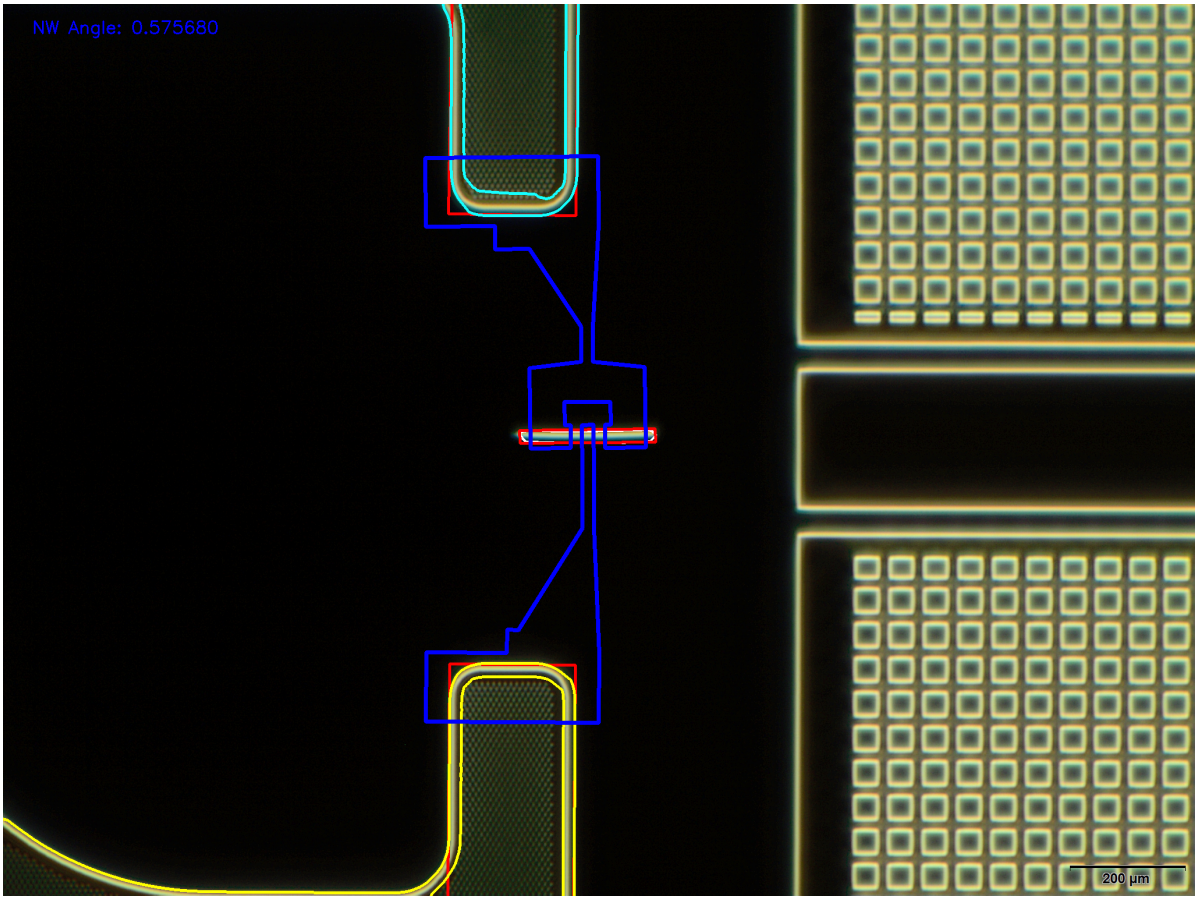

Figure 2.9: Image created by the image recognition software made by Thijs Stavenga [42] to create the contacts holding the placed nanowire. The nanowire in this figure is the nanowire observed in this section. It is almost perfectly aligned to the V_1 axis ($\Theta = 0.57°$)

which implies that the $B/B_c(\theta)$ forms a scaled and translated ellipse around origin (α_{good},α_{bad}). Due to the f_{max} not being explicitly known, we have too many unknown to known to retrieve the correct values for $B_{c,good}$, $B_{c,bad}$, α_{good} and α_{bad}. We only know α_{good} is positive and α_{bad} is negative.

2.8. Alignment during an angle scan

The alignment follows the same idea as Section 2.4, however, here we have to account for two different virtual vectors at once. This can cause several problems. First of all, this causes the problem if we do not know both basis axes $V1$ and $V2$ before starting the angle scan. we would re-adjust the angle of the field wrongly. Example: say we have been aligned on the $Z/V1$-axis, and its alignment corresponds to $B_x = 0.01B_z$. We do not know the alignment for $Y/V2$, so we assume $B_x = 0B_y$. However the true value might be $B_X = 0.02B_y$. This would mean that the closer the angle gets closer to the $Y/V2$-axis, the stronger it tries to apply the $B_x \to 0$ constraint, while we want to align it as $B_x \to 0.02B_y$. This can be solve by making an excursion in both the Z and Y-axes, or by calculating $V2$ by using the known value of $V1$ and the current aligned X-field.
Second of all, the alignment does depend on some hysteresis effect. Our alignment could fail making a circle. We see in Figure 2.14 that when $V1$ and $V2$ are known (here at angles $\theta = 0$ and $\theta = 90°$ respectively), that the aligning perpendicular coil fields our found on the curve. This means our procedure is verified in the case of angle scans. In fact, the Q_i, Q_c and f_{res} stay constant over the whole angle scan (not shown), except for a dip in Q_i at $\sim 78°$, perpendicular to the nanowire axis.

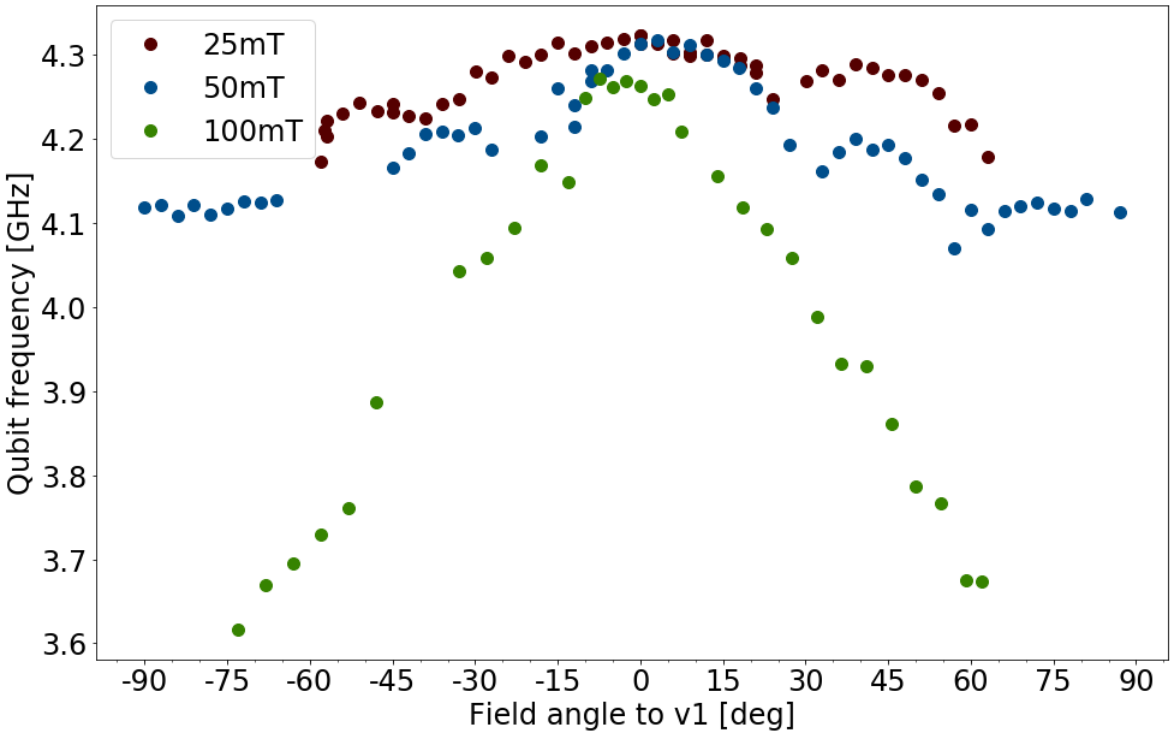

Figure 2.10: Results for the measured qubit f_{01} frequency as a function of the angle to $V1$. The qubit physically lies almost parallel to $V1$, as indicated by the maximum in f_{01}. At 25 mT, for angles $< 59^\circ$ and $> 60^\circ$, no qubit could be found. At the apparent dips (2 visible for 25 mT and 4 visible for 50 mT), the qubit frequency peak broadens until its SNR ratio is too low to measure. At 100 mT the qubit frequency goes too low for the chosen measurement range.

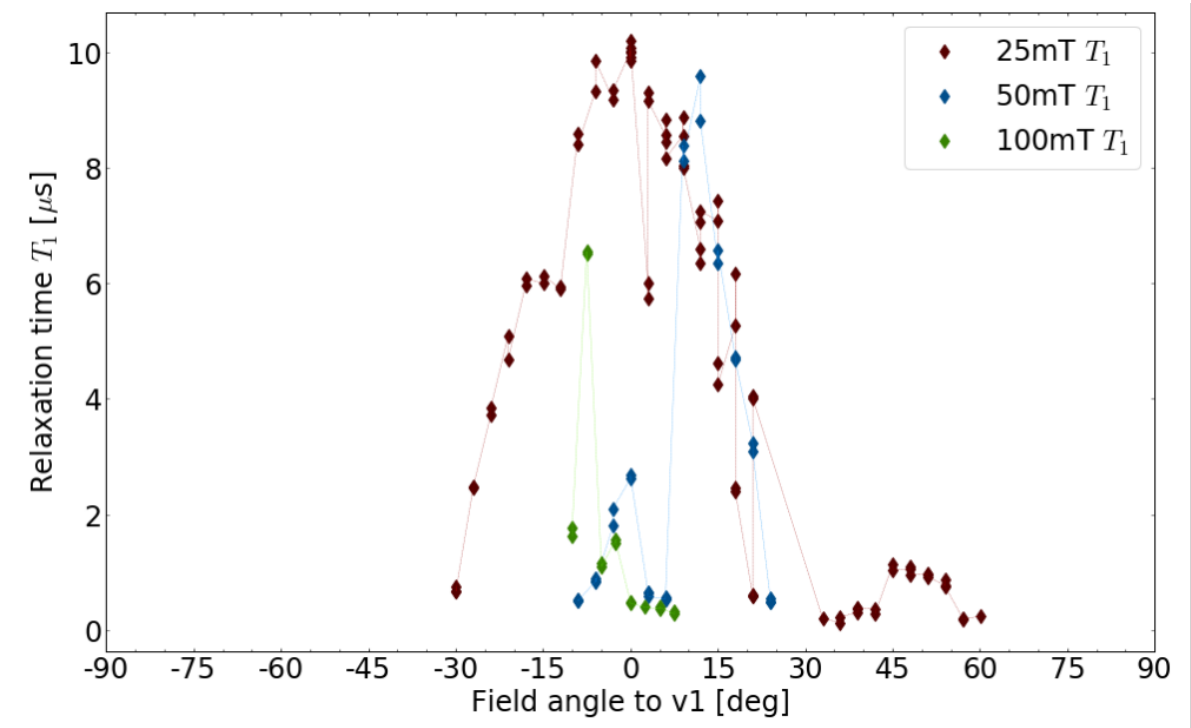

Figure 2.11: Results for the measured qubit relaxation time T_1 frequency as a function of the angle to $V1$. The relaxation time is strongly dependent on the angle and the disappearance coincides with the first peak broadening in the qubit frequency.

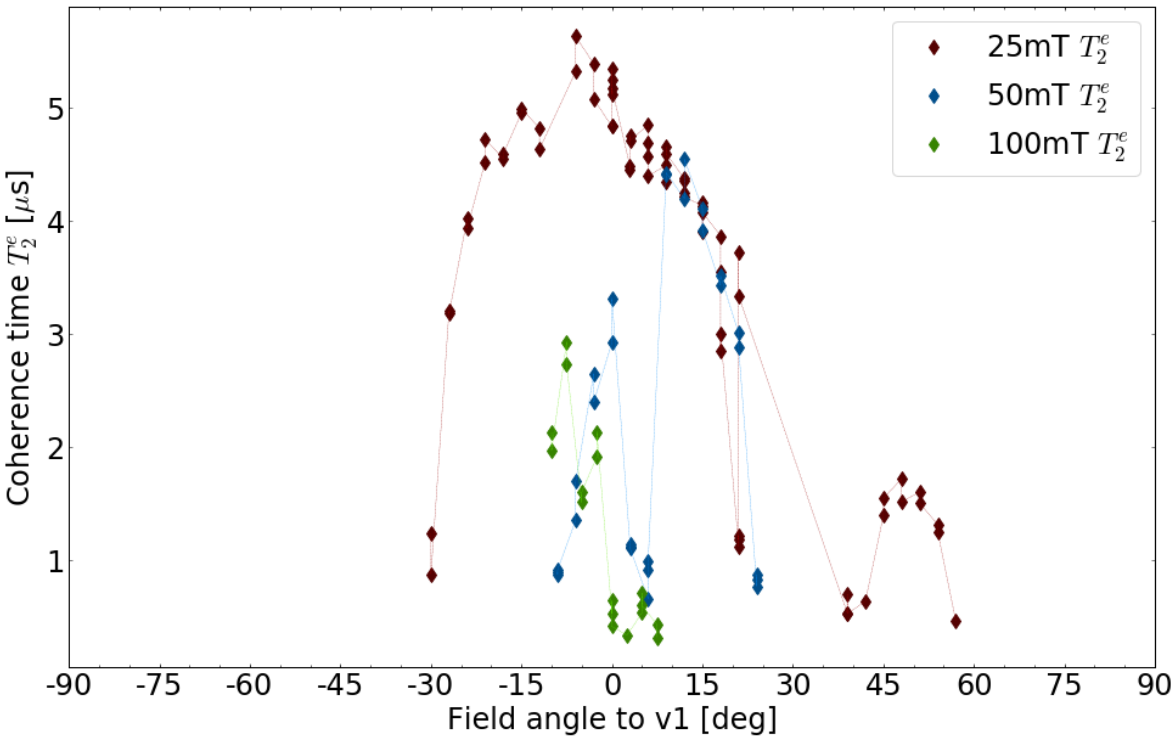

Figure 2.12: Results for the measured qubit coherence time T_2^e frequency as a function of the angle to $V1$ for different in-plane magnetic fields. The results again show a clear optimal angle, which coincides with T_1 measurements.

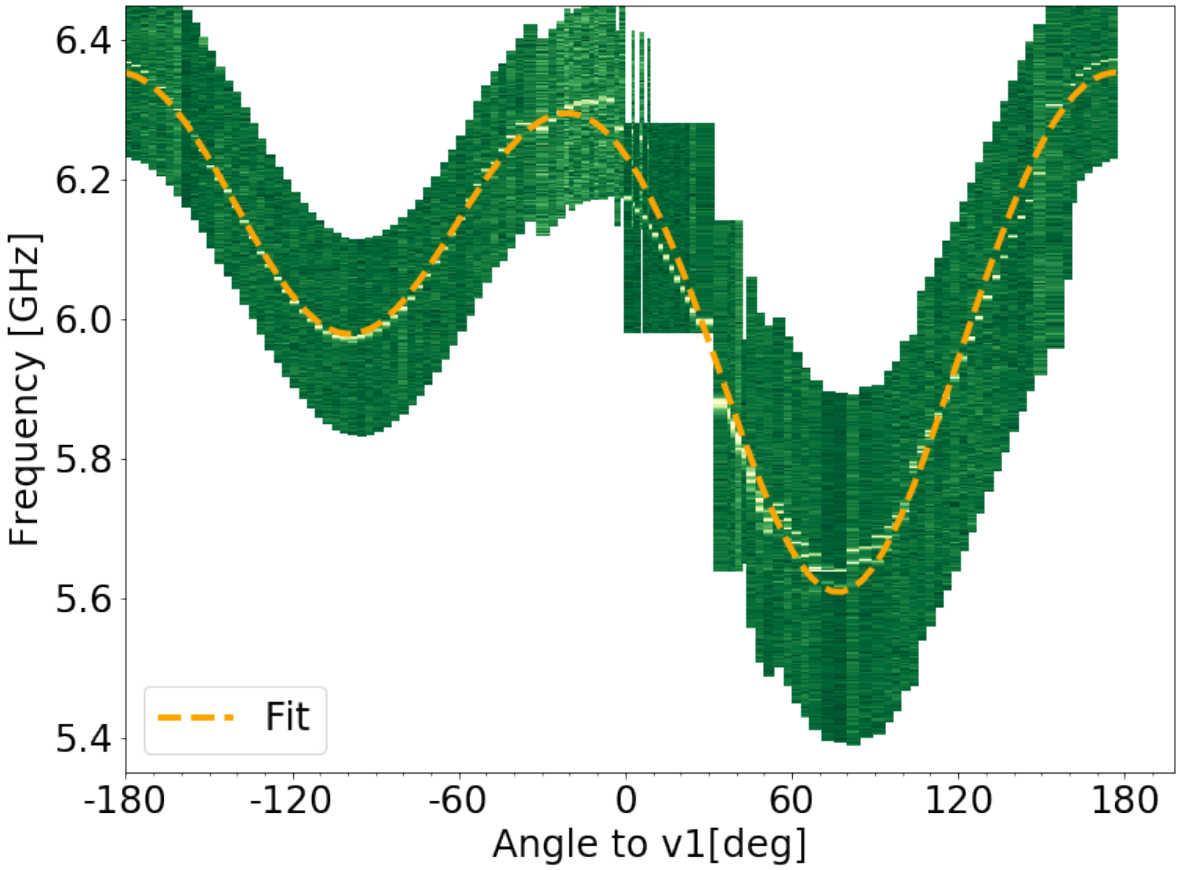

Figure 2.13: Results for the measured qubit frequency vs. the full 360° angle scan. The fit used is

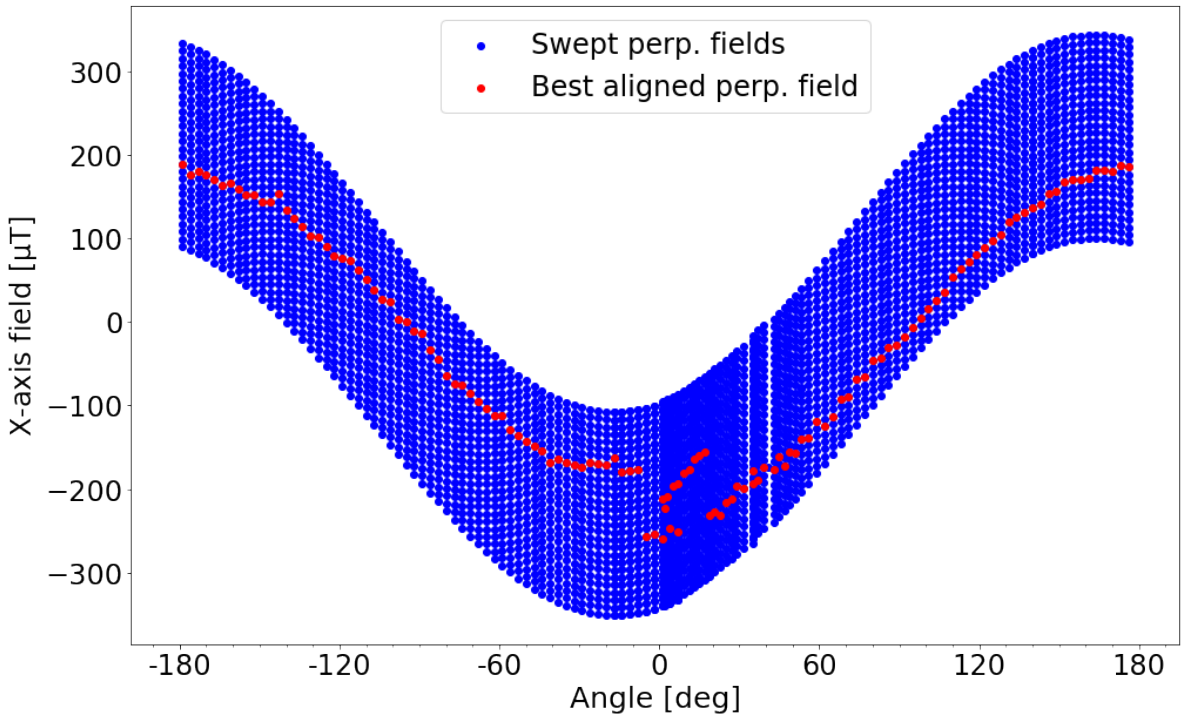

Figure 2.14: The result for the angle scan. The blue values are the values swept against. These values were determined by the $V1$ and $V2$ values found in earlier alignments. The red dots show the perpendicular X-field for which the angle was aligned. The angle scan was made at a constant field magnitude $|B| = 25\,\mathrm{mT}$. It swept up from angle $\theta = 0$ to a value of $\theta = 369° = 9°$.

3

Flux noise and its microscopic origin

3.1. Introduction

Flux tunable transmons and flux qubits are currently being limited by flux noise. Qubit control can still be improved by having more accurafte and faster hardware, but there are limitations inherent to the fabrication of the qubit itself. The effects can often be measured by the T_1 and T_2 times of the qubit, called the relaxation and decoherence time respectively. Relaxation is caused by loss of the excited state of the qubit due to loss channels. Energy can be exchanged with these channels at the qubit frequency. The decoherence time can be split into two contributions[38, 48]:

$$T_2^{-1} = T_\phi^{-1} + (2T_1)^{-1} \tag{3.1}$$

where T_ϕ is the dephasing time. So not only is the coherence time dependent on the relaxation, the qubit is also affected due to the phase changing undesirably. The phase evolution is dependent on the qubit frequency. Thus dephasing is an effect of the qubit frequency fluctuating [34]. In a flux tunable transmon, there are be several ways that this could happen. The main effect investigated is the flux noise, due to fluctuations in the magnetic field as sensed by the SQUID. Other effects would be photon number fluctuations in the resonator or the critical current noise of the Josephon junction. This SQUID is used by the qubit as a knob to tune the qubit frequency, so any noise in the sensed magnetic field creates noise in the flux measured by the SQUID and thus creates fluctuations in the qubit frequency. Ideally these noise sources do not increase the dephasing such that $T_\phi \ll 2T_1$, making the T_2 be $2T_1$-limited. Qubits are preferentially used at the sweetspot: the flux bias where the qubit frequency is first-order insensitive to the flux. During two-qubit gates, flux pulses are used to tune the qubits frequencies off-sweetspot and the qubit coherence times will decrease to flux noise. This can limit the 2-qubit-gate fidelity [8]. Our nanowire transmons have the possibility of being voltage tunable using a voltage bias gate, or being flux tunable by embedding the wire in a SQUID. Of these two, only the flux tunable transmon is sensitive to flux noise.[33].

3.2. History of flux noise

In 1987, Wellstood et al. [50] found the noise in SQUID devices of different sizes and materials below 500 mK to be

$$\sim 7\,\mu\Phi_0 \mathrm{Hz}^{-1/2} \text{ at } 1\,\mathrm{Hz}$$

with an $1/f^\alpha$-type noise and $0.58 < \alpha < 0.65$. This was measured by extracting the SQUID current as a result of the changing flux. The measured frequency ranges of the power spectral density went from 0.1 Hz to 10 kHz. After more than a decade, superconducting qubits were researched. Decoherence proved a difficult problem to solve, so methods involving control sequences were investigated to quantify the noise sources, such as critical current, charge or flux noise [34][18]. Among the first measurements of the flux noise in qubits were Yoshihara [54] fitting $\frac{A}{f}$ using $\sqrt{A} = 1-2\,\mu\Phi_0\mathrm{Hz}^{-1/2}$ for frequencies to which the Echo filter is sensitive, similar to Wellstood. Kakuyanagi [23] found a similar result and Bialczak [6] fit $\frac{A}{f^\alpha}$ using $\sqrt{A} = 4\mu\Phi_0/\sqrt{\mathrm{Hz}}$ and $\alpha = 0.95$ for lower frequencies. New methods have been devised to probe the higher frequency components. Nowadays, the measurements have found that the $1/f$-like signal spans over 13 order of magnitude (from 10^{-4} Hz to 10^9 Hz) with no clear indication of lower or upper cut-off frequencies[6][37].

3.3. Measurements of flux noise

Different protocols have been devised to characterize the flux noise power spectral densities at different frequency ranges. First off, the investigation began at lower frequencies. However, since no cut-off frequencies have been found yet, methods to probe even GHz levels of noise have been developed. The measurement methods used to date are:

1. By measurement of the SQUID flux using a second flux-locked SQUID and measuring its current or voltage and sweeping the bias current of the first SQUID, which is useful for low frequency noise measurements from 0.1 Hz to 10 kHz. [50][49][27].

2. By measuring the sensitivity of a qubit's frequency vs. the change in flux, and calculating its dephasing time using the Echo or Ramsey sequences, which are sensitive up to frequencies corresponding to $\frac{1}{t_{meas}}$, where t_{meas} is the measurement time. [54][23][33]

3. By measuring the correlations in the Echo times with two coupled qubits , being sensitive to all noise under ~ 1 MHz[55].

4. Fast repetitions of a single shot readout after a Ramsey experiment, with a fixed free induction time and detuning frequency, using Bernoulli statistics to deduce $S(f)$ for frequencies 10 Hz to the single shot repetition rate $\frac{1}{t_{rep}}$, which can go up to kHz ranges. [52]

5. Measurement of the proportion of clockwise vs. counterclockwise currents in a flux qubit. Should be 1 at exactly zero flux bias. This can be used to probe the low frequency noise [29][30][37].

6. Measurement of the anti-correlation of positively biased and negatively biased qubit frequency deviations. This measurement has been done to frequencies as low as 10^{-5} Hz[6].

7. By extracting, next to the sensitivites, the exact noise amplitude at a certain frequency independent of the form of the spectrum, usable for Ramsey, Echo and CPMG sequences. This is useful for frequencies 1 to 10 MHz[10].

8. Measurement of the relaxation time during driven evolution of qubit. This can probe the noise up to 200 MHz[53].

9. Measurement of decay of Rabi oscillations at a strong driving field so that a certain Rabi oscillation frequency (and noise frequency) is probed. Frequencies up to 1.4 GHz are able to be probed using this [56].

10. Measurement of the T_1 and residual excitation population of a flux tunable flux qubit, tuned to a certain frequency, and the ratio excitation and relaxation to discern classical and quantum noise. This probes $1-10$ GHz[37].

11. Measurement of the spurious excited state population of the qubit by showing excitation due to dephasing noise at a frequency equal to the detuning of the qubit-resonator. This probes GHz frequencies [41].

These methods can be combined to give a complete view of the noise characteristics across the entire frequency span. It has been shown that the methods give consistent results. Methods that could be used for our transmon qubits include methods 2,4,7,8,9 and when modified 10.

3.4. Possible microscopic origins of the flux noise

In the process of improving the SQUID white temperature noise of the form $\epsilon/1\,\text{Hz} \approx 16 k_B T\sqrt{LC}$ by lowering the temperature, it was found that a residual $1/f$-noise was present at even the theoretical lowest noise floors [45]. This has been investigated to not be fully explained by critical current fluctuations [25]. Even at mK temperatures, it has been shown that the fluctuations were only weakly dependent on geometries. It was proposed that the fluctuations could be caused by local magnetic moments [50]. It was also shown that vortex motion by having a non-zero cooling magnetic field, could not explain the flux noise present at low-T_c SQUIDs [26]. For (large) magnetic moments (far) outside the superconductor, the flux noise of magnetic moments would scale linearly with the dimension. We do not observe this. It is also shown that nuclear spins

can not sufficiently influence the flux by themselves [26]. It was subsequently shown that surface paramagnetic magnetic moments exist. If it were electron spins, the density of spins would equal $\sigma_s = 5 \cdot 10^{-17}\,\mathrm{m}^{-2}$ [39]. Over the years, several spin species have been proposed. This must have a defect site on which they can bind. In amorphous SiO2 substrates, the E' center, nonbridging oxygen hole center, superoxide radical [26] or P_b center [13] could form a defect site. While in superconductors, OH defect sites could form, or other yet unknown defects. [26] The candidates for the paramagnetic spin species are:

1. Physisorbed hydrogen [47]
2. Gap state created by oxygen electron deficiencies on neighboring O 2p orbitals [31]
3. Metal Induced Gap States [11]
4. Oxygen doublets (on Lewis base sites of sapphire [12])
5. Oxygen triplets [27][46]

There have been multiple hints of a large density of hydrogen on the surface [12][37]. Oxygen [27] has also been seen as a source of flux noise. These spins also need an interaction with their environment to fluctuate. This could be due to interaction with the environment, or others spins. The following processes have been proposed:

1. Unpaired electrons that hop on and off defect sites through thermal activation. The spin does not change at one defect site. [26]. However, there are only a few thermal TLSs at mK temperatures[17].
2. Dangling bond electrons (at substrate-oxide interfaces) flip their spin by spin-orbit interaction with TLSs where TLSs tunnel by a phonon-induced transition [13]. Also, not sufficient TLSs are available to use this as the main interaction.
3. The interaction between electron spins due to intermediate interaction with a conduction electron, called the RKKY interaction. This causes spin diffusion.[17] However, it has been shown that magnetization is not conserved, while the RKKY interaction is magnetization conserving.[7].
4. Dipole-dipole interaction, but the typical interaction noise is too small to explain the flux noise [17].
5. Spin-orbit interaction, but flux noise is still seen when orbital angular momenta of the atoms are zero [51], also the resulting noise would be too small to explain the flux noise [17]
6. Interaction due to hyperfine splitting with nuclei [51]

None of these models have been conclusive. However, there has been evidence of spin diffusion at low frequencies, due to spin-spin interaction on SQUIDs. The characteristic crossover frequency would be dependent of $f_c \propto \frac{1}{W^2}$. For $W = 1\,\mu\mathrm{m}$ it was found $f_c \approx 0.1 - 1\,\mathrm{Hz}$[30], however no signal was found in [49].

4

Spin fluctuator noise in a magnetic field

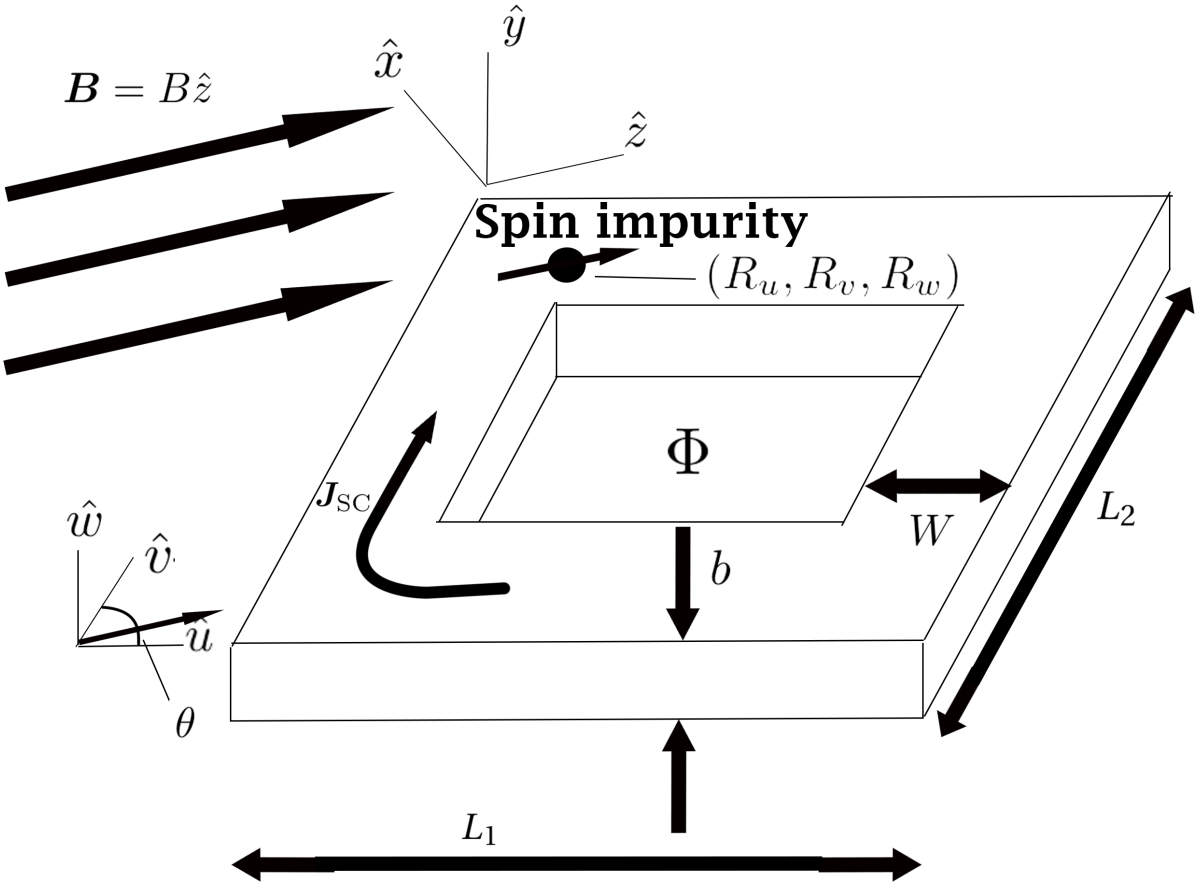

Figure 4.1: A superconducting loop showing the coordinate systems used in this chapter. The spin lives at location (R_u, R_v, R_w) and is pointing in the $\hat{z}$-direction. The $\hat{y}$-axis is perpendicular to SQUID loop $\hat{u}\hat{v}$-plane. The $\hat{u}$-axis is radially inwards and the $\hat{v}$-axis signifies the direction in which the current J_{SC} flows (or comes from, for negative currents). Through the loop area, a magnetic flux Φ can form, depending on the applied magnetic fields. The superconducting loop has ring width W and film thickness b.

Since the qubits we are looking at are compatible with in-plane magnetic fields above 10 mT, we would like to know what the effect of the magnetic field is on the flux noise amplitude. The consensus is that the noise is caused by local magnetic moments, thus we want to find out the coupling of spins near the SQUID to the flux and to couple the spin fluctuations to the flux fluctuations. Furthermore, we assume there are many such fluctuators present in the SQUID region, with different rates of flipping. These all couple to the SQUID with their spin-flipping, which makes the measured flux through the SQUID fluctuate a tiny, but noticeable

amount. Since we are dealing with three different coordinate systems: the magnet direction with the corresponding spin basis coordinate system, the SQUID geometry coordinate system and the spin position coordinates. We have depicted them all in Figure 4.1. In this chapter, we will discuss the relation of spin correlations to flux fluctuations in Section 4.1, find the spin fluctuator power spectral densities in Section 4.2, find the exact coupling constants in Section 4.4 and work out an example for surface electron spins on our SQUIDs in Section 4.6.

4.1. Coupling of the spin fluctuations to the SQUID flux

In these subsections, we follow the outline of LaForest and De Sousa [28] to arrive at the coupling between the total flux created by spins on, in or near the superconducting film, and the spin state. We can find the flux fluctuations as a function of spin-fluctuations, assuming some constraints on the spin interactions.
The analysis is based on the fact that each spin can be linearly coupled to the flux through

$$\Phi_s(t) = -\sum_n \mathbf{F}(\mathbf{R}_n) \cdot \mathbf{s}_n(t) \tag{4.1}$$

where Φ_s is the flux added by the collection of spins near the SQUID, $\mathbf{F}(\mathbf{R}_n)$ is a vector in $\mathbb{R}^3$ that describes the u, v or w contribution of the n'th spin at location $\mathbf{R}_n$. The unit of $\mathbf{F}$ is [Wb]. $\mathbf{s}_n$ is a vector in $\mathbb{R}^3$ giving the direction of the i'th spin. $\mathbf{s}_n$ is dimensionless and for $S = 1/2$-particles (such as electrons), we find $|\mathbf{s}_n| = \frac{1}{2}$. In [28] and Appendix H it has been shown that Φ_s is indeed linear in $\mathbf{s}$.
Using the Wiener-Khinchin theorem, we find that

$$S_\Phi(f) = \int df e^{2\pi i f t} \langle \Phi(t)\Phi(0) \rangle \tag{4.2}$$

where $S_\Phi(f)$ is the power spectral density of the flux through spin fluctuations. f is the frequency in Hz. $\langle \ldots \rangle$ is the thermal equilibrium expectation value, given quantum mechanically through $\langle \hat{A} \rangle = \mathrm{Tr}\big(\rho_{Th} A\big)$ where $\rho_{Th} = \frac{\exp(-\mathscr{H}/k_B T)}{\mathscr{Z}}$, where $\mathscr{H}$ is a Hamiltonian of the spin dynamics and $\mathscr{Z} = \mathrm{Tr}\big(\exp(-\mathscr{H}/k_B T)\big)$. We will show that the flux power spectral density is linearly related to the spin component (cross) power spectral densities. A full derivation can be found in Appendix G, we will give the outline here.
We assume the interaction between spins to be zero, and that the individual spins are independent and identically distributed. However, the processes of interaction given in Section 3.4 actually use spin-spin interactions to fluctuate. So this model only works if the Zeeman splitting is the dominant energy scale. We decompose the spin correlation to their components in the $\hat{x}, \hat{y}, \hat{z}$-directions as in Figure 4.1. In a later section the magnetic field direction will be chosen to be $\hat{z}$. We suppose a continuum of spins in space with a density of spins $\sigma(\mathbf{R})$. We finally suppose all spin components have their proper (cross) power spectral density $S_{\alpha\beta}(f) = \int df e^{2\pi i f t} \langle s_\alpha(t) s_\beta(0) \rangle$. We can define the total direct spin-to-SQUID coupling using

$$C_{\alpha\beta} := \int d^3R \sigma(R) F_\alpha(\mathbf{R}) F_\beta(\mathbf{R}) \tag{4.3}$$

and we can find, all written out:

$$\begin{aligned} S_\Phi(f) &= \sum_{\alpha,\beta=i,j,k} C_{\alpha\beta} S_{\alpha\beta}(f) \\ &= C_{xx}S_{xx}(f) + C_{yy}S_{yy}(f) + C_{zz}S_{zz}(f) + C_{xy}(S_{xy}(f) + S_{yx}(f)) \\ &\quad + C_{xz}(S_{xz}(f) + S_{zx}(f)) + C_{yz}(S_{yz}(f) + S_{zy}(f)) \end{aligned} \tag{4.4}$$

We will find expressions for $S_{\alpha\beta}(f)$ in Section 4.2 and values for $C_{\alpha\beta}$ in Section 4.4.

4.2. Spin fluctuator model

We start by looking at a spin-1/2 particle that has a certain incoherent flipping rate Γ. We would like to find the dependence of the magnetic field on the spin. Thus we assume the dominant Hamiltonian influencing the spin is due to the Zeeman effect

$$\mathscr{H}_Z = -\boldsymbol{\mu} \cdot \mathbf{B}. \tag{4.5}$$

Here $\boldsymbol{\mu}$ is the magnetic moment of the spin and $\mathbf{B}$ is the (externally) applied field on the magnetic moment. This means the energy difference of the spin-1/2 particle is dictated by the magnetic field. To clarify, the

magnetic moment of a spin-1/2 can be described by:

$$\boldsymbol{\mu} = \frac{g_s q}{2m}\hbar \boldsymbol{s} = g\mu_s \boldsymbol{s} \tag{4.6a}$$

$$\boldsymbol{s} = \frac{1}{2}\boldsymbol{\sigma} \tag{4.6b}$$

where g_s is the g-factor, q the charge of the particle, m the mass of the particle and $\boldsymbol{s}$ the spin operator acting on the spin states. $\boldsymbol{\sigma}$ is the vector of Pauli matrices, each matrix having eigenvalues of ± 1.
Typical values for an electron are $g \approx -2$ and $\mu_B = |\frac{e\hbar}{2m_e}|$ so that this can be written as $\mathscr{H}_Z \approx \mu_B \boldsymbol{\sigma}\cdot\boldsymbol{B}$ We assume without loss of generality that the magnetic field is in the $+\hat{z}$ direction, as shown in Figure 4.1, $\boldsymbol{B} = B\hat{z}$. The spin axis of quantization is chosen along $\boldsymbol{B}$. The resulting energy levels for a spin-1/2 system are:

$$E_{\pm} = \pm\frac{g_s\mu_s}{2}B \tag{4.7}$$

where the positive energy is where $\boldsymbol{\mu}$ is anti-parallel to $\boldsymbol{B}$ and the negative lower energy is where $\boldsymbol{\mu}$ is parallel to $\boldsymbol{B}$. We also assume the system is in thermal equilibrium, and through the Boltzmann equation, we find

$$P(\psi = \psi_+) = \frac{e^{-\tilde{B}}}{e^{+\tilde{B}} + e^{-\tilde{B}}} \tag{4.8a}$$

$$P(\psi = \psi_-) = \frac{e^{+\tilde{B}}}{e^{+\tilde{B}} + e^{-\tilde{B}}} \tag{4.8b}$$

where $\tilde{B} = \frac{g_s\mu_s B}{2k_B T}$. We can use this to determine the relaxation and excitation rates:

$$\Gamma_\uparrow := \Gamma_{-\to+} = \Gamma\frac{P(\psi_+)}{P(\psi_-) + P(\psi_+)} \tag{4.9a}$$

$$\Gamma_\downarrow := \Gamma_{+\to-} = \Gamma\frac{P(\psi_-)}{P(\psi_-) + P(\psi_+)} \tag{4.9b}$$

where $\Gamma = \Gamma_\uparrow + \Gamma_\downarrow$. This means that for a general spin fluctuator under Zeeman interaction, we will find $\Gamma_\uparrow = \exp(-2\tilde{B})\Gamma_\downarrow$. Since we can assume either $\Gamma_\uparrow, \Gamma_\downarrow$ or Γ to be fixed while sweeping the field, we need to choose one. In this chapter $\Gamma_\downarrow$ is kept fixed. Reasoning and more explanation for this choice will be given in Section 4.5.

4.2.1. Power spectral density of $S_{zz}(f, B)$

Using the model defined above, we use QuTiP [21] [22] to simulate a fluctuating spin using a fixed $\Gamma_\downarrow$ and different fields. We can also derive an analytical solution for the power spectral density, as found in Appendix F. The solution is a Lorentzian and follows the relation:

$$S_{zz}(f) = \frac{1}{\cosh(\tilde{B})}\frac{\exp(-\tilde{B})\Gamma_\downarrow}{(2\exp(-\tilde{B})\cosh(\tilde{B})\Gamma_\downarrow)^2 + (2\pi f)^2} + \frac{1}{4}\tanh^2(\tilde{B})\delta(f) \tag{4.10}$$

The results for several fields B and rates $\Gamma_\downarrow$ are visible in Figure 4.2. Simulations for negative frequencies have also been done in QuTiP. They show that $S_{zz}(f) = S_{zz}(-f)$, as expected, since this noise can be described classically.
We can distinguish two regions of the Lorentzian. One where $f \ll \Gamma_\downarrow$, and one where $f \gg \Gamma_\downarrow$. These features can be described as

$$S_{zz}(f \ll \Gamma) = \frac{\exp(+\tilde{B})}{4\cosh^3(\tilde{B})\Gamma_\downarrow} \tag{4.11a}$$

$$S_{zz}(f \gg \Gamma) = \frac{\exp(-\tilde{B})}{\cosh(\tilde{B})}\frac{\Gamma_\downarrow}{(2\pi f)^2}. \tag{4.11b}$$

We see that the low frequency components of a fluctuator do not change at lower frequencies; it is peaked. However, the high frequency components go down as $\sim f^{-2}$. We can also look at what the influence of the field is at low fields ($\tilde{B} \to 0$) and high fields ($\tilde{B} \to \infty$):

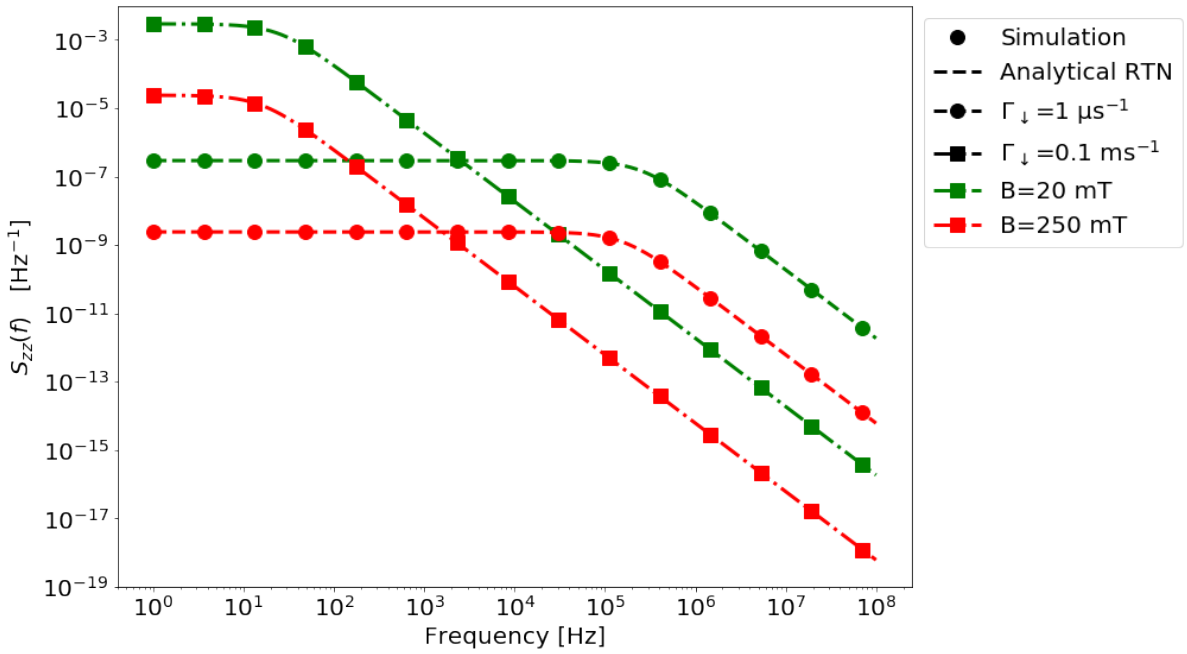

Figure 4.2: The values of a single spin fluctuator. The dots and squares are simulation results, while the lines are Equation (4.10). The green lines are taken at $B = 20\,\mathrm{mT}$, the red at $B = 250\,\mathrm{mT}$. The squares use a rate $\Gamma_\downarrow$ of $10\,\mu\mathrm{s}^{-1}$, while the diamonds use a rate of $0.1\,\mathrm{ms}^{-1}$. The temperature used in the simulation is 50 mK.

$$\lim_{B\to 0} S_{zz}(f) = \frac{\Gamma_\downarrow}{\Gamma_\downarrow^2 + (2\pi f)^2}$$

and

$$\lim_{B\to\infty} S_{zz}(f) \approx \lim_{B\to\infty} \frac{\exp(-2\tilde{B})\Gamma_\downarrow}{\Gamma_\downarrow^2 + (2\pi f)^2} \to 0$$

We find that at zero field there exist only fluctuations by some other mechanism. At high fields, the Zeeman effect dominates these other interactions and polarizes the spins. As such, the total fluctuations tend to 0.
As a consistency check, we integrate over all frequencies $\int df S_{zz}(f)$ to check the total noise power. We find using $\int dx \frac{a}{a^2+(2\pi x)^2} = \frac{\arctan(2\pi x/a)}{2\pi}$ and Equation (4.10)

$$\langle s_z^2 \rangle = \int_{-\infty}^{\infty} df S_{zz}(f) = \frac{1}{2\cosh^2(\tilde{B})} \left[\frac{1}{2\pi} \arctan\left(\frac{2\pi f}{2\exp(-\tilde{B})\cosh(\tilde{B})\Gamma_\downarrow} \right) \right]_{-\infty}^{\infty} + \frac{1}{4}\tanh^2(\tilde{B}) = \frac{1}{4}\frac{1+\sinh^2(\tilde{B})}{\cosh^2(\tilde{B})} = \frac{1}{4} \tag{4.12}$$

This is also what you would expect statistically from $\langle s_z^2 \rangle = \left(+\frac{1}{2}\right)^2 P(\psi_+) + \left(-\frac{1}{2}\right)^2 P(\psi_-) = \frac{1}{4}(P(\psi_+) + (1 - P(\psi_+)) = \frac{1}{4}$.

4.2.2. Power spectral density of $S_{xx}(f)$

However, a spin is not only a classical two level system, it also precesses due to the time evolution imposed by the Hamiltonian:

$$U(t,0) = \exp\left(-\frac{i}{\hbar} H_Z t\right) = \exp\left(\frac{i}{\hbar}\left[\frac{g\mu_s B}{2}\right]\hat{\sigma}_z t\right) \tag{4.13}$$

We can now define the precession frequency $f_Z := \frac{g\mu_s B}{4\pi\hbar}$ so that $U(t,0) = e^{2\pi i f_Z \hat{\sigma}_z t}$, which is called the Larmor precession. We determine the autocorrelation function, in the case there are no flips $\Gamma = 0$.

$$\langle \sigma_x(t)\sigma_x(0)\rangle = \left\langle U^\dagger(t,0)\sigma_x U(t,0)\sigma_x \right\rangle = \left\langle \exp(-2\cdot 2\pi i f_Z \sigma_z t)\right\rangle = \frac{e^{-\tilde{B}}e^{-4\pi i f_Z t} + e^{+\tilde{B}}e^{+4\pi i f_Z t}}{2\cosh(\tilde{B})} \tag{4.14}$$

We find similarly that $\langle\sigma_x(0)\sigma_x(t)\rangle = \langle\exp(2\cdot 2\pi i f_Z \sigma_z t)\rangle$. Both results are consistent and give the following result for positive and negative f at $\Gamma = 0$:

$$S_{xx}(f) = \frac{e^{\tilde{B}}\delta(f+2f_Z) + e^{-\tilde{B}}\delta(f-2f_Z)}{2\cosh(\tilde{B})}. \tag{4.15}$$

We note that the relation

$$S_{xx}(-f) = S_{xx}(f) + \int_{-\infty}^{\infty} dt e^{2\pi i f t}\langle[\sigma_x(0),\sigma_x(t)]\rangle \tag{4.16}$$

holds. Equation (4.15) implies that $\frac{S_{xx}(2f_Z)}{S_{xx}(-2f_Z)} = e^{-2\tilde{B}}$, which we verify in simulations. Now we turn on the incoherent flipping. Again, we fix $\Gamma_\downarrow$ and can sweep the magnetic field. We simulate again and plot the results for several fields in Figure 4.3. We have found an equation that fits almost everywhere, except near the peaks:

$$\hat{S}_{xx}(f) = \frac{1}{4}\frac{2\Gamma_{avg}}{(\Gamma_{avg})^2 + (2\pi f - 2f_Z)^2} \tag{4.17}$$

where $\Gamma_{avg} = \frac{\Gamma_\downarrow+\Gamma_\uparrow}{2}$. Note the term $(2\pi f - 2f_Z)$, where we subtract a normal frequency from an angular frequency. I do not know the origin, but since the simulated $S_{zz}(f)$ follows the exact analytical derivation, we assume that in the simulation a factor 2π is missing. We can also calculate $S_{xx}(-f)$ for negative frequencies. We can see an inequality around $2f_Z$. This can be seen more clearly in Figure 4.4. We see three effects as $\tilde{B}$

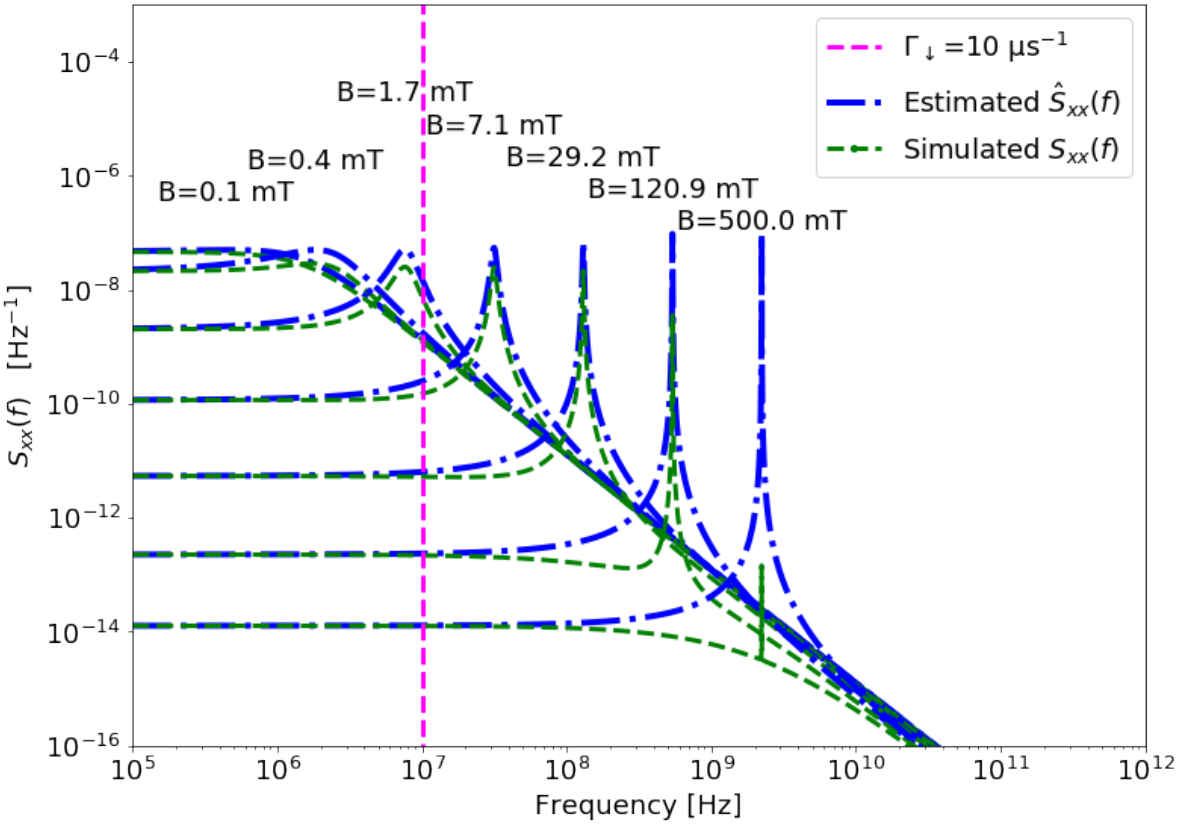

Figure 4.3: The power spectral density in the XX-direction of a single spin fluctuator using a low flipping rate ($\Gamma \lessapprox 2f_Z$). The temperature used in the simulation is 50 mK.

grows higher. The peak at $f = 2f_Z$ shrinks, until it disappears. The peak at $-f = 2f_Z$ almost stays unchanged. However, it changes to match Equation (4.17) perfectly. To investigate the effect of the field on the frequency peak, we look at $\frac{S_{xx}(\pm f)}{\hat{S}_{xx}(f)}$ for low flipping rates Γ. A peak appears centered around $2\pi f = 2f_Z$. The peak value

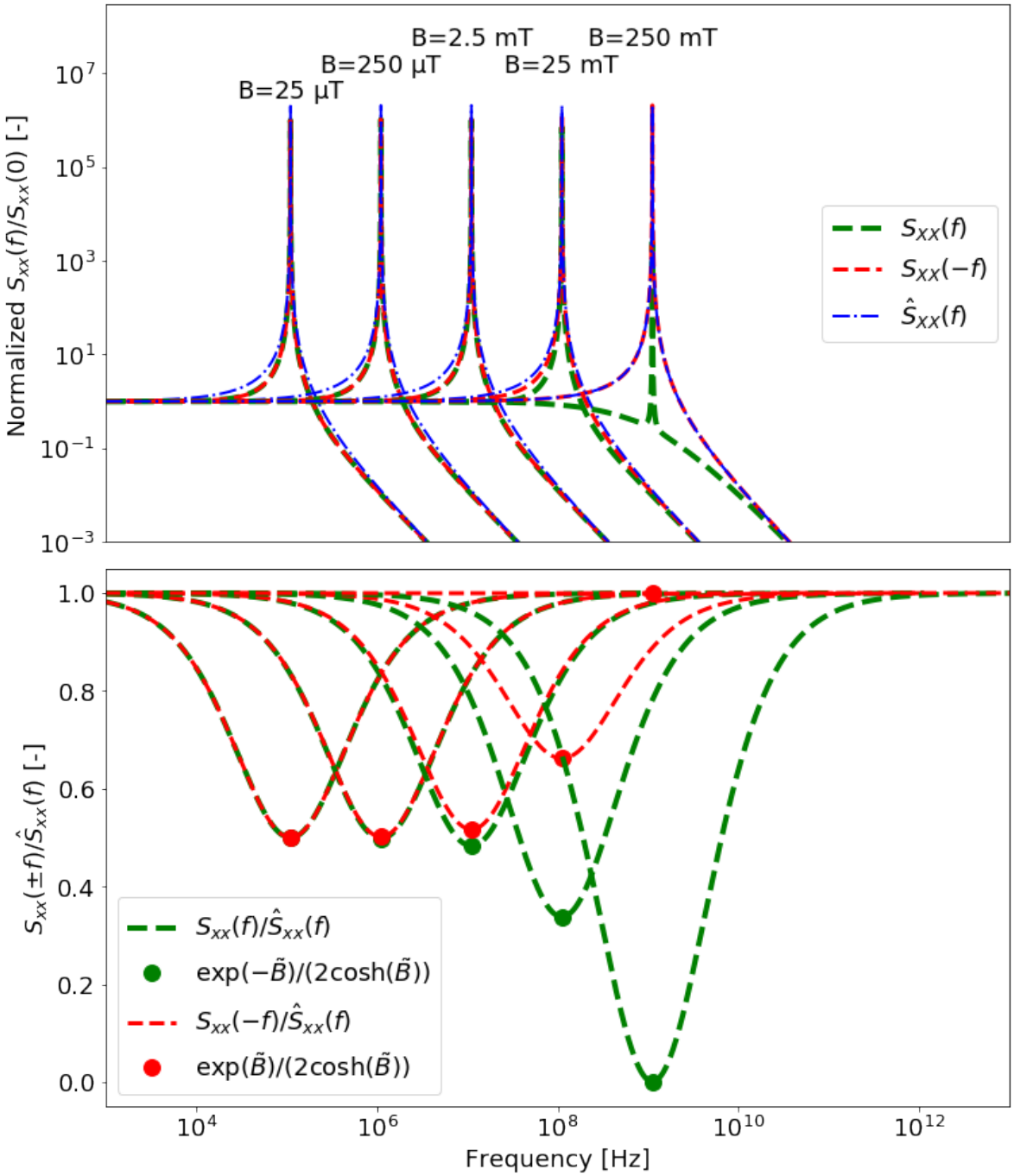

Figure 4.4: The power spectral density in the XX-direction of a single spin fluctuator using a low flipping rate ($\Gamma \ll 2f_Z$). (Top) The shifteng and widening/disappearance of the Larmor precession peaks. The values are normalized to emphasize the peak behavior. (Bottom) The (multiplicative) error from the approximation $\hat{S}_{xx}(f)$ from Equation (4.17). The dots are equation (4.15). The temperature used in the simulation is 50 mK.

is consistent with the magnitude from Equation (4.15):

$$S_{xx}\left(f = \frac{2f_Z}{2\pi}\right) = \frac{\exp(-\tilde{B})}{\cosh(\tilde{B})}\hat{S}_{xx}(f) \tag{4.18}$$

$$S_{xx}\left(f = -\frac{2f_Z}{2\pi}\right) = \frac{\exp(\tilde{B})}{\cosh(\tilde{B})}\hat{S}_{xx}(f) \tag{4.19}$$

The limits $f \ll 2f_Z$, $f \gg 2f_Z$ can be described by:

$$\frac{S_{xx}(\pm(f))}{\hat{S}_{xx}(f)} = 2f_Z \cdot \frac{\exp(\mp\tilde{B})}{2\cosh(\tilde{B})}(2\pi f) \text{ when } f \ll 2f_Z \tag{4.20}$$

$$\frac{S_{xx}(\pm(f))}{\hat{S}_{xx}(f)} = 2f_Z \cdot \frac{\exp(\mp\tilde{B})}{2\cosh(\tilde{B})}\frac{1}{2\pi f} \text{ when } f \gg 2f_Z \tag{4.21}$$

with tails of $\sim f$ at low frequencies and $\sim \frac{1}{f}$ over high frequencies. The curve does not match a Gaussian or Lorentzian.

4.2.3. Other (cross-)spectra

Through reasoning, we would expect that $S_{xx}(f) = S_{yy}(f)$, since the Hamiltonian does not change its form if we rotate the system around the Z-axis. We also expect to have $S_{xz} = S_{zx} = S_{yz} = S_{zy} = 0$, for all positive and negative frequencies, all fields and all switching rates. The explanation lies in the fact that $\langle s_z s_x \rangle = \langle s_z \rangle \langle s_x \rangle$ is independent and that $\langle s_x \rangle$ is zero. All important relations between spectral densities are shown in Table 4.1.
However, we do see some small activity of $S_{xy}(f), S_{yx}(f)$ at positive and negative frequencies. However, simulations show they are related by $S_{xy}(f) = -S_{yx}(f)$. This and all other information is summarized in Table 4.1.

Table 4.1: Relation of the different spectral densities $S_{\alpha\beta}$ to each other. A "0" means that the PSD is zero at all frequencies.

$S_{\alpha\beta}(f)$	x	y	z
x	$S_{xx}(f) = S_{yy}(f)$	$S_{yx}(f) = -S_{xy}(f)$	0
y	$S_{yx}(f) = -S_{xy}(f)$	$S_{xx}(f) = S_{yy}(f)$	0
z	0	0	$S_{zz}(f)$

The fact that $S_{xx} = S_{yy}$ and $S_{xy} = -S_{yx}$ implies that Equation (4.4) can be simplified to

$$S_\Phi(f) = (C_{xx} + C_{yy})S_{xx}(f) + C_{zz}S_{zz}(f) \tag{4.22}$$

Since $S_{xy}(f)$ and $S_{yx}(f)$ cancel in this equation, we do not follow up on its exact formulaic nature.

4.3. Ensemble of fluctuators

To get to the ubiquitous $1/f$-noise signal, it is customary (see e.g. [40]) to assume a distribution of relaxation rates $\Gamma_\downarrow = \frac{1}{T_1}$ that is distributed as $P(\Gamma_\downarrow) = \frac{1}{\Gamma_\downarrow}$ (or equivalently $P(T_1) = \frac{1}{T_1}$) with some maximum and minimum $\Gamma_{\downarrow,max}, \Gamma_{\downarrow,min}$.
We can now solve for the $S_{zz}(f)$ spectrum for an ensemble of fluctuators. A more complete derivation can be found in Appendix I. We find for $\Gamma_{min} < f < \Gamma_{max}$

$$S_{zz,ens}(f) = \frac{\pi}{2\ln(\Gamma_{max}/\Gamma_{min})}\frac{1}{2\cosh^2(\tilde{B})(2\pi f)} \tag{4.23}$$

We can see this ensemble plotted in Figure 4.5.
We can derive the same for $\hat{S}_{xx}$, the estimate of the S_{xx}. Due to the singularity at $2\pi f = 2f_Z$, we need the full analytical solution and which is

$$\hat{S}_{xx,ens}(f) = \frac{1}{16}\frac{1}{\ln(\Gamma_{max}/\Gamma_{min})}\frac{2}{(2\pi f - 2f_Z)}\left[\arctan\left(\frac{\frac{1+\exp(-2\tilde{B})}{2}\Gamma_{max}}{2\pi f - 2f_Z}\right) - \arctan\left(\frac{\frac{1+\exp(-2\tilde{B})}{2}\Gamma_{min}}{2\pi f - 2f_Z}\right)\right] \tag{4.24}$$

Note that $\hat{S}_{xx,ens}$ is nearly independent of magnetic field. However, $f_Z \propto B$, so the peak shifts. Also, since $\hat{S}_{xx}$ did not describe the peak at $2f_Z$ well, the real spectrum might be inconsistent with this formula. In Section 4.6, that the inconsistency is only important near the Larmor precession peak.

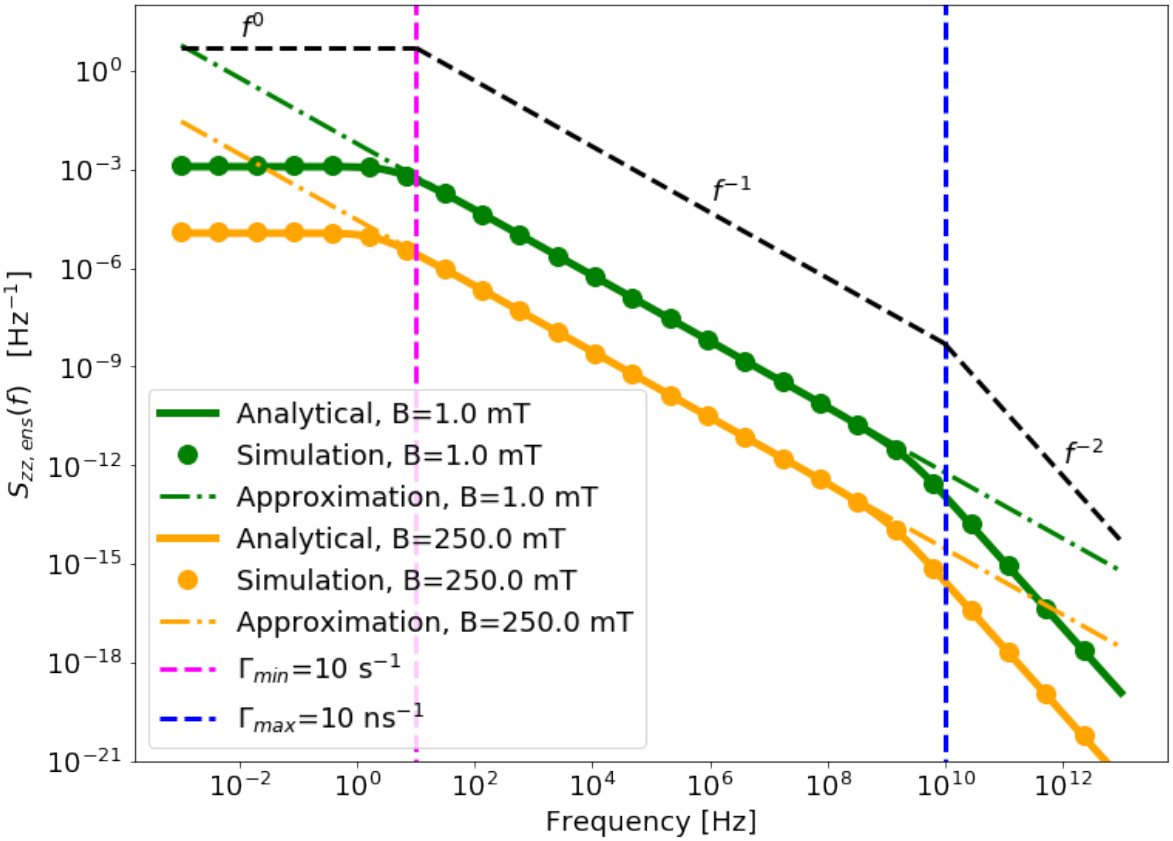

Figure 4.5: The average ensemble power spectral density of the Z-component of the spin fluctuator. It uses a temperature of $T = 50\,\text{mK}$. The black dashed lines are a guide to the eye. The dash-dotted lines are Equation (4.23), while the green and orange dashed lines are (I.4). The dots represent the simulation results.

4.4. The flux vector F

In Section 4.2, we found that the flux noise PSD is a linear combination of the spin PSD, in the constants $C_{\alpha\beta}$. To find a value for these constants, we can follow the model of LaForest and De Sousa to model the SQUID we are using. We can find equations for **F** relating the spin to the flux inside of the loop. The derivation can be found in Appendix H. The derivation assumes a thin film, where the (bulk) magnetic penetration depth λ is smaller than the width W, and on the same order (or smaller) than the thickness b. It also assumes all current flows in the direction of the wire ($\hat{v}$). The formulae for **F** inside, outside and on the superconductor surface can be found. For clarity, we define the SQUID film to be residing at $-W/2 < R_u < W/2$ and $-b < R_w < 0$. We find

$$F_u(R_u, R_w) = -\frac{g\mu_s\mu_0}{4\pi}\int_{-1}^{1} dx \left\{ \frac{J_{\text{SC}}\left(\frac{2x}{W}\right)}{I_{\text{SC}}} \ln\left[\frac{(x-R_u)^2 + R_w^2}{(x-R_u)^2 + (R_w+b)^2}\right]\right\} \tag{4.25a}$$

$$F_v(R_u, R_w) = 0 \tag{4.25b}$$

$$F_w(R_u, R_w) = \frac{g\mu_s\mu_0}{2\pi}\int_{-1}^{1} dx \left\{ \frac{J_{\text{SC}}\left(\frac{2x}{W}\right)}{I_{\text{SC}}} \left[\arctan\left(\frac{R_w+b}{x-R_u}\right) - \arctan\left(\frac{R_w}{x-R_u}\right)\right]\right\}. \tag{4.25c}$$

Here g, μ_s are the g-factor and the magnetic moments of the spin-particle respectively, μ_0 the vacuum permeability, W and b are the width and the thickness of the thin-film superconductor strip creating the SQUID. $\boldsymbol{J}_{SC}$ is the current density at a certain point along the width. The expression for the current density can be found in Appendix H.
We can visualize the results for **F** for our SQUID in Figure 4.6.
Immediately, important symmetries are visible (also present in Equations 4.25).

1. $F_v = 0$ everywhere.

Table 4.2: Dimensions of our SQUID and SQUID materials. The effective $\lambda_{eff} = \frac{\lambda}{\tanh(b/\lambda)}$ [20] using the λ found in [43].

SQUID property	Value
Material	NbTiN
Dimensions $L_1 \times L_2$	$2 \times 3\,\mu$m
Width W	$1.5\,\mu$m
Thickness b	100 nm
Magnetic penetration depth λ	246 nm
Effective magnetic penetration depth λ_{eff}	640 nm
Coherence length ξ_0	$1-10$ nm

2. $F_u(R_u, R_w) = F_u(-R_u, R_w)$, so symmetric in the width (around $R_u = 0$).

3. $F_u(R_u, -b/2 + R_w) = -F_u(R_u, -b/2 - R_w)$, so antisymmetric in the thickness (around $R_w = -b/2$). So $F_u = 0$ when $R_w = -b/2$.

4. $F_w(R_u, R_w) = -F_w(-R_u, R_w)$, so antisymmetric in the width (around $R_u = 0$). So $F_w = 0$ when $R_u = 0$.

5. $F_w(R_u, -b/2 + R_w) = F_w(R_u, -b/2 - R_w)$, so symmetric in the thickness (around $R_w = -b/2$)

6. As a result $|F|$ is symmetric in the width and thickness ($R_u = 0$ and $R_w = -b/2$) with $|F| = 0$ when exactly in the middle of the wire ($R_u = 0, R_w = -b/2$).

We find that the high values of **F** are concentrated around the surface, as expected. This can be explained by the current density being highest at the two sides at $R_u = \pm W/2$.

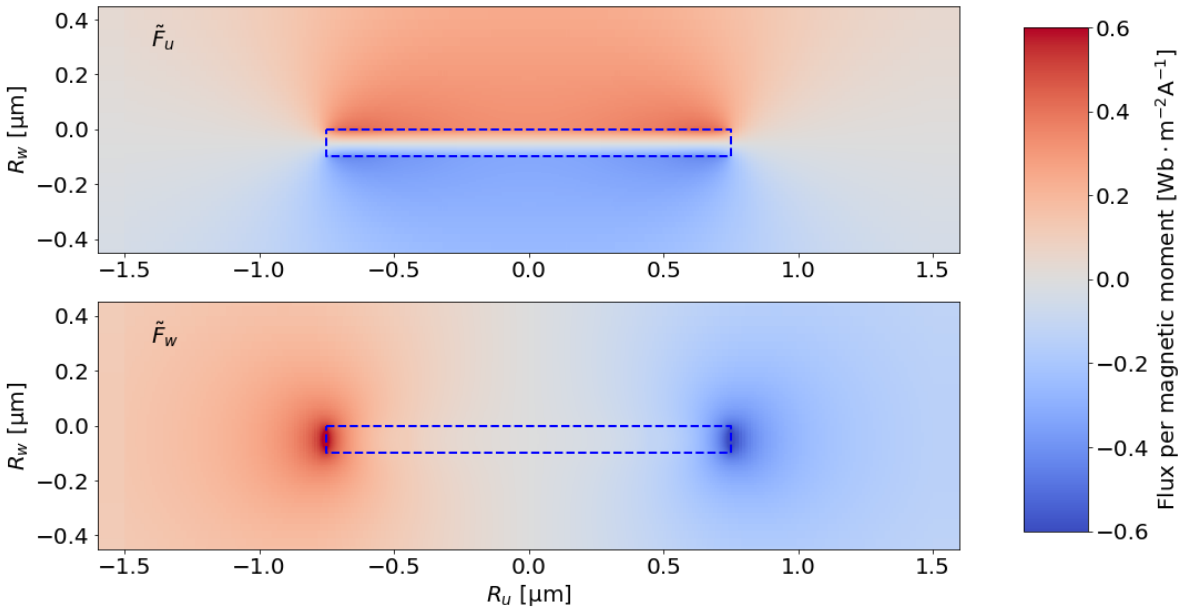

Figure 4.6: The value of $\tilde{F}_u = \frac{F_u}{g\mu_s}$ (top) and $\tilde{F}_w = \frac{F_w}{g\mu_s}$ (bottom) at or around the wire. A positive value implies that a spin located at that point adds a positive flux to the total flux. The blue dashed line outlines the superconducting film used for our SQUID. Its top is at $R_w = 0$ and its bottom surface at $R_w = -b$. $\tilde{F}_v = 0$ everywhere and not shown.

We notice in Equation (4.22) that we only invoke products of $F_\alpha F_\beta$. The magnetic field will only lie in the $\hat{u}, \hat{v}$-plane of the film (and the $\hat{z}$-direction of the spin). We find, with the help of Figure 4.1 that $F_y = F_w$. We now define an angle θ that corresponds to the angle between the u-axis radially inwards of the SQUID and the angle of the magnetic field. We define $\theta = 90°$ as the angle that the B-field aligns with the v-axis. We apply a basis transformation on **F** from the SQUID coordinate system $(\hat{u}, \hat{v}, \hat{w})$ to the spin-fluctuator coordinate system $(\hat{x}, \hat{y}, \hat{z})$. So $F_x = \cos(\theta)F_u - \sin(\theta)F_v$ and $F_z = \sin(\theta)F_u + \cos(\theta)F_v$. The terms F_v are zero.

We find $C_{xx} = \int d^3R\sigma(\mathbf{R})\cos^2(\theta)F_u^2(\mathbf{R})$ and $C_{yy} = \int d^3R\sigma(\mathbf{R})F_w^2(\mathbf{R})$ and $C_{zz} = \int d^3R\sigma(\mathbf{R})\sin^2(\theta)F_u^2(\mathbf{R})$ to extend Equation (4.22) to

$$S_\Phi(f) = S_{xx}(f)[\cos^2(\theta)C_{uu} + C_{ww}] + S_{zz}(f)\sin^2(\theta)C_{uu} \tag{4.26}$$

Since we have found the F_u, F_v, F_w to be dependent on $g\mu_s$, which is particle species-dependent we can separate the spin species and geometry through defining a new constant $\tilde{C}_{\alpha\beta}$ for every non-curved SQUID segment of length L:

$$C_{\alpha\beta,s,g} = \sigma_{d,s,g}(g_s\mu_s)^2 \cdot \tilde{C}_{\alpha\beta,g}L \tag{4.27}$$

where the index s defines a spin species, such as nuclear spins or electron spins, and the index g defines a geometry for the spins, such as the interior spins, superconductor-vacuum interface spins, superconductor-substrate interface spins or substrate spins. σ_d is the areal density (for interface geometries) or volume density. (for volume geometries) and L the length of this segment of the thin-film (for square SQUID washers of outer dimensions $L_1 \times L_2$, the length of a segment would either $L_1 - W$ or $L_2 - W$). We can see that $\tilde{C}_{\alpha\beta}$ is solely dependent on the dimensions of the cross-section of the superconducting thin film. Its unit is $[\left(\mathrm{Wb}\cdot\mathrm{m}^{-2}\mathrm{A}^{-1}\right)^2\mathrm{m}^{-1}\mathrm{m}^{-\mathrm{d}}]$ where $d = 2$ for area geometries and $d = 3$ for volume geometries.
We could now calculate the flux noise for a straight SQUID segment of length L using the sum of of the contributions of spins from different geometries and species:

$$S_\Phi(f) = \sum_{s\in S, g\in G}(\mu_s g_s)^2 L\sigma_{d,s,g}\left[S_{xx,s}(f)[\cos^2(\theta)\tilde{C}_{uu,s,g} + \tilde{C}_{ww,g}] + S_{zz,s}(f)\sin^2(\theta)\tilde{C}_{uu,g}\right]. \tag{4.28}$$

A worked out example of this will be shown in Section 4.6.

4.5. The nature of flipping rates

We have three natural choices of fixing the flipping rates in this simulation model in comparison to the magnetic field. We have $\Gamma_\downarrow$, which is the rate at which the spin relaxes to the lowest energy state. This is the natural choice to fix when the system is in equilibrium and can only dissipate energy to its environment. In e.g. Bloch-Redfield theory, the $T_1 = \frac{1}{\Gamma_\downarrow}$ is used to describe the spin dynamics. Another choice is the $\Gamma_\uparrow$, which is the excitation due to the environment. A last rate to consider is the $\Gamma_{tot} = \Gamma_\downarrow + \Gamma_\uparrow$. This is the rate of going to a thermal equilibrium, when brought out of equilibrium. This can be clearly seen in Equations (F.6). As such, it is entirely dependent on the Hamiltonian of the system and its environment.
In Appendix I, we found that for a Lorentzian, the chosen flipping rate does not influence the final $1/f$-rate, except for a change in amplitude depending on differences in $\frac{1}{\ln(\Gamma_{i,max}/\Gamma_{i,min})}$ and behaviour for $f > \Gamma_{max}$ or $f < \Gamma_{min}$. This means the results given in this chapter still holds (up to a factor unity) for any choice of Γ_i.

4.6. Tying everything together: a $S = 1/2$-electron example

For our SQUID, the dimensions are given in Table 4.2. Following the strategy of Section 4.4, we can find the values of all components of $\frac{\mathbf{F}(\mathbf{R})}{g\mu_s}$ for all desired spin positions $\mathbf{R}$ using Equations (4.25). We can now calculate the constant $\tilde{C}_{\alpha\beta,g}$ for a geometry g. The geometry that will be used in this example is the vacuum-superconductor interface. This interface is described by the top surface of the film, $-W/2 < R_u < W/2$ at $R_w = 0$, and the sides of the film, $-b < R_z < 0$ at $R_w = W/2$ and $R_w = -W/2$. Using Equations (4.3) and (4.27), we find $\tilde{C}_{uu,top} = 2.0\cdot10^{-7}$, $\tilde{C}_{ww,top} = 0.47\cdot10^{-7}$ for the top surface of the SQUID. For one side, we find: $\tilde{C}_{uu,side} = 0.02\cdot10^{-7}$ and $\tilde{C}_{ww,side} = 0.38\cdot10^{-7}$. The total, one top surface and two sides, amounts to $\tilde{C}_{uu} = 2.0\cdot10^{-7}\,(\mathrm{Wb}\cdot\mathrm{m}^{-2}\mathrm{A}^{-1})^2\mathrm{m}^{-3}$ and $\tilde{C}_{ww} = 1.25\cdot10^{-7}\,(\mathrm{Wb}\cdot\mathrm{m}^{-2}\mathrm{A}^{-1})^2\mathrm{m}^{-3}$

We will assume only one spin specie to be participating, and electronic in nature. This means $g \approx -2$ and $\mu_s = \mu_B$. We assume the surface spin density to be $\sigma_d = 5\cdot10^{17}\,\mathrm{m}^{-2}$ [39].
We can now use Equation (4.28) to find a relation of a straight segment of length L

$$S_\Phi(f) = (-2\mu_B)^2\sigma_d L\left[(\tilde{C}_{uu}\cos^2(\theta) + \tilde{C}_{ww})S_{xx}(f) + \tilde{C}_{uu}\sin^2(\theta)S_{zz}(f)\right] \tag{4.29}$$

We can now assume a range of rates $\Gamma_\downarrow$, such that we find the values of $S_{xx}(f)$ and $S_{zz}(f)$ for an ensemble of spins. We use Section 4.2 to give an approximation of the resulting spectra. We assume $\Gamma_{max} = 10^{12}$ and $\Gamma_{min} = 10^{-5}$.

$$S_\Phi(f) \approx \frac{\pi(-2\mu_B)^2\sigma_d}{2\ln(\Gamma_{max}/\Gamma_{min})}\left[\frac{\tilde{C}_{uu}\cos^2(\theta) + \tilde{C}_{ww}}{16(2\pi f - 2f_Z)} + \frac{\tilde{C}_{uu}\sin^2(\theta)}{2\cosh^2(\tilde{B})(2\pi f)}\right]$$

We then take a square washer SQUID of dimensions $L_1 \times L_2$ (with inner loop dimensions $L_1 - 2W \times L_2 - 2W$) and integrate over the length in the four different directions (so we integrate each part with $\theta_i = \theta_{i-1} + \frac{\pi}{2}$). This can be described as:

$$S_\Phi(f) \approx \frac{\pi(-2\mu_B)^2\sigma_d}{2\ln(\Gamma_{max}/\Gamma_{min})} \times \left((2L_1 \left[\frac{\tilde{C}_{uu}\cos^2(\theta) + \tilde{C}_{ww}}{16(2\pi f - 2f_Z)} + \frac{\tilde{C}_{uu}\sin^2(\theta)}{2\cosh^2(\tilde{B})(2\pi f)} \right] + 2L_2 \left[\frac{\tilde{C}_{uu}\sin^2(\theta) + \tilde{C}_{ww}}{16(2\pi f - 2f_Z)} + \frac{\tilde{C}_{uu}\cos^2(\theta)}{2\cosh^2(\tilde{B})(2\pi f)} \right]) \right) \tag{4.30}$$

in reality, we use Equations (4.23) and (4.24) for $S_{xx,ens}$ and $S_{zz,ens}$ to find a better approximation for the flux noise power spectral density. We can now find the dependency of the flux noise as a function of the frequency, the field magnitude and field angle. Since we do not know the full formula for $S_{xx}(f)$, we again use simulations to create Figures 4.7 and 4.8.
Some important features are:

1. At very high fields (see 1 T in Figure 4.7), the only spin component that contributes to the flux noise is the $S_{yy}(f)$-spectrum.
2. If $L_1 \neq L_2$, there is a dependence of the flux noise to the angle of the magnetic field with the SQUID as visible in Figure 4.8. The dependence is proportional to $(|L_1/L_2| - 1)\cos^2(\theta)$. This dependence shifts $\pi/2$ when measuring $f > 2f_Z$.
3. Using this angle dependence, we can deduce the separate contributions of $S_{xx}(f)$ and $S_{zz}(f)$.
4. The $S_{xx}(f)$ spectrum is the dominant contribution to the measured spectrum at and above $f \geq 2f_Z$.
5. Above $f > 2f_Z$, we see the sensitivity of the flux noise to the magnetic field dropping.

4.7. Further research and outlook

This model is only a prototype of more extensive models. The obvious extension would be adding examples or equations for $S > \frac{1}{2}$, which could be used for coupled spin systems in certain defect sites (e.g. the oxygen triplet state). Hyperfine splitting with the hydrogen atom is also a strong contender for simulation.
A good exercise would be to find the dynamic susceptibility of a boson bath or spin bath and find the relation to the relaxation rates (or excitation rates) of the spin system.
We could also try to include secondary interactions next to the Zeeman effect, to the model, introducing spin-spin correlations. A good first step would be to explore nearest-neighbour interaction. We could also skip using simulation by using the spin diffusion model. This is an alternative to taking a distribution of flipping rates $P(\Gamma) \propto \frac{1}{\Gamma}$ to find an $1/f$ noise spectrum. We might use that to model the spin dynamics instead.
We could also investigate different geometries, aka triangle shaped washers or pentagon-shaped washers. These should give a different effect on the flux noise as the angle of the magnetic field is changed. See Section 4.6 for an example of a square washer SQUID.
Another avenue to investigate might be to look at specific molecules and the effect of spin-orbit coupling on the flux.

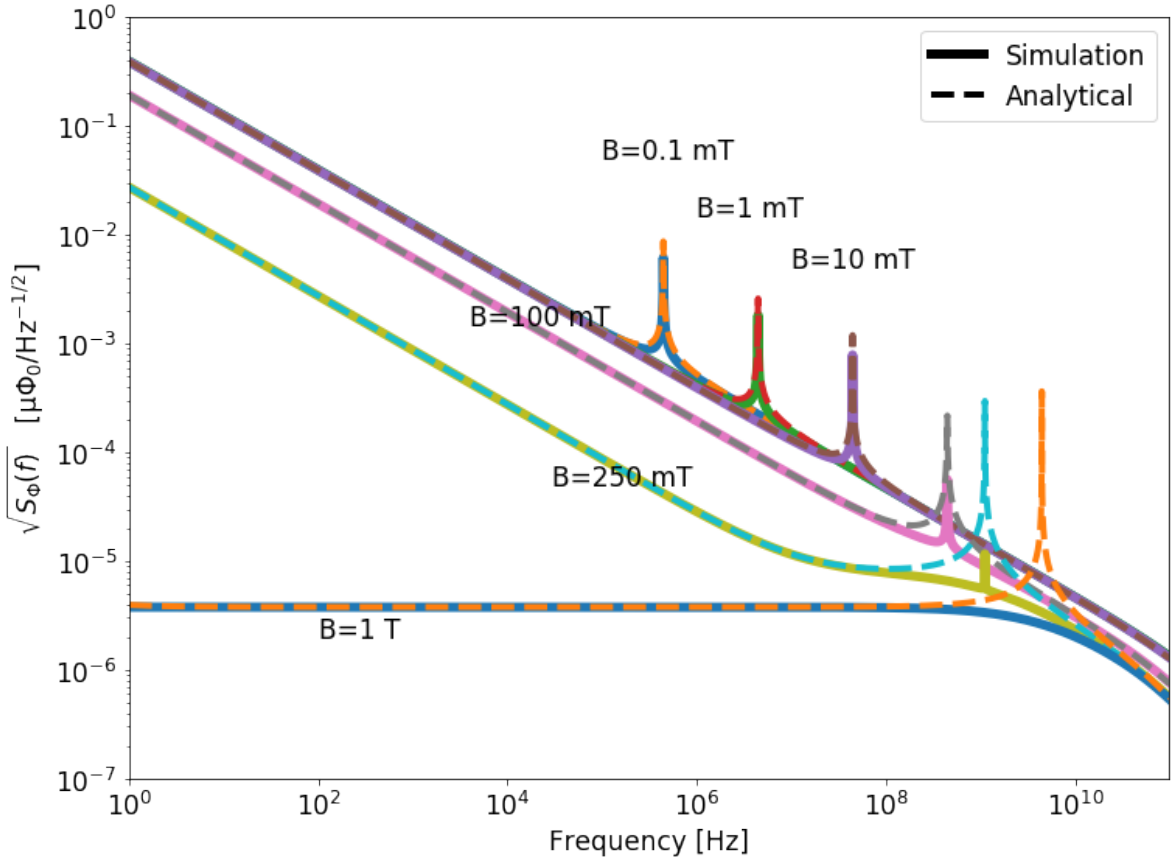

Figure 4.7: The result of a complete flux noise calculation given in this chapter for different magnetic fields at $T = 50\,\text{mK}$. The dashed lines are the analytical equations described in Equation (4.30); the solid lines describe the simulation results.

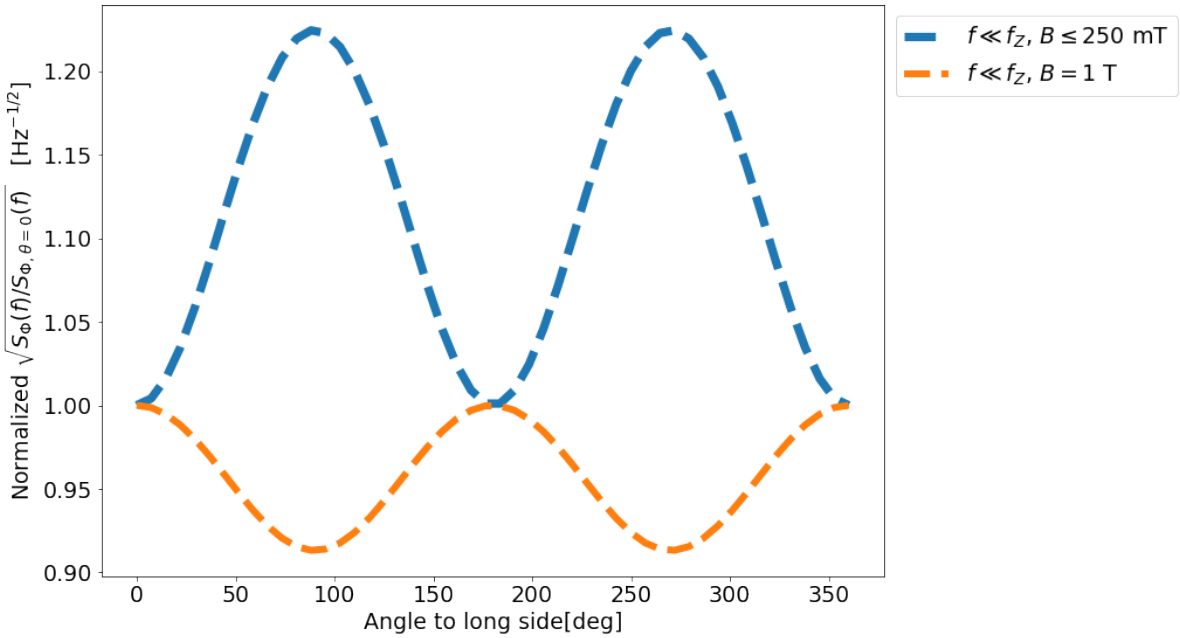

Figure 4.8: The change in the $S_\Phi(f)$ at a certain frequency as a function of the angle θ that the magnetic field makes with the SQUID loop. This is done for $f \ll f_Z$ and low and high fields.

5

Flux tunable nanowire transmon in a magnetic field

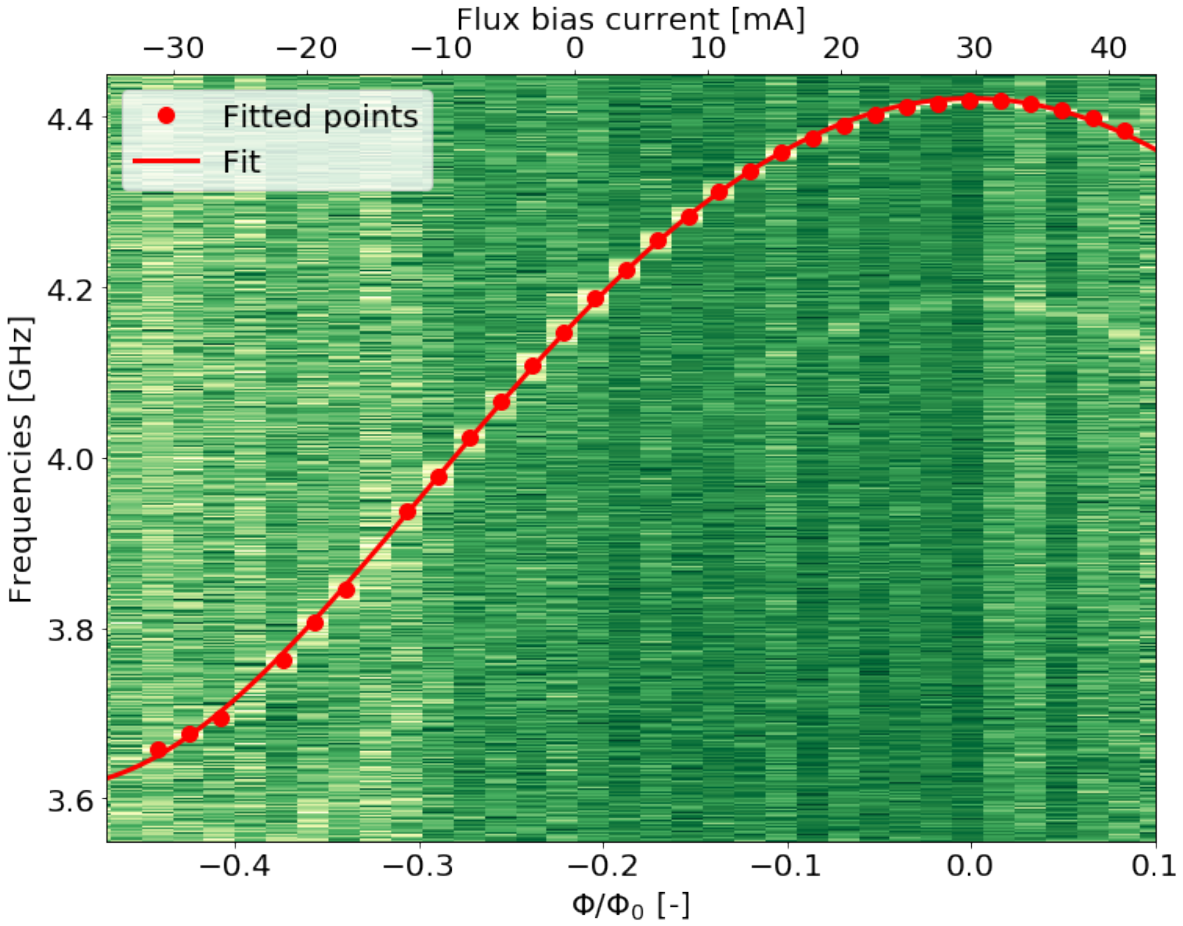

Figure 5.1: A flux arc of a flux tunable qubit. We have made a frequency sweep for different flux bias line currents. The red dots constitute the qubit peaks that have been correctly determined. The red line is a fit to these points using Equation (5.1). We have found an asymmetry of $d = 0.67$, which is large compared to the expected value of 1. and found that the conversion of one flux quantum vs. the flux bias current is 118 mA/Φ_0. The offset is 26 mA.

In this section we will discuss a flux tunable nanowire transmon, a Dmon, in an in-plane magnetic field. This is on a chip without airbridges and with on-chip wirebonds where a flux tunable qubit with a qubit frequency

in the desired range of 4 – 6 GHz was available.
We will discuss the difficulties encountered in characterizing this qubit and results found during this exploration.
The main path towards measuring flux noise has the four following requirements:

1. A qubit with measurable T_2^e Echo times > 5 µs
2. A flux tunable qubit
3. Measurement of a continuous qubit frequency arc for at least a flux sweep of $\sim \frac{\Phi_0}{2}$
4. A stable in-plane magnetic field
5. A qubit that has measurable T_2^e up to at least 250 mT.

We have met all these requirements in isolation, but as of yet, every qubit had at least one of the requirements not met.

5.1. Flux tunability

We have designed our flux tunable qubits so that they are tunable using the perpendicular coil and - if available - a dedicated flux bias line. An example of a flux tunable qubit is shown in Figure 5.1. This is a qubit with a dedicated feed bias line. We vary the feed bias line and see that the two sweetspots (where the maximum and minimum frequencies are) are only a few GHz apart, indicating a very large asymmetry in the Josephson junction.
The asymmetry in the nanowires qubits can be approximated by using Equations (1.2) and (1.6) in tandem, when we are in the transmon regime $E_J \gg E_C$:

$$f_{01}(\Phi) \approx f_{01,max}\left((1-d^2)\cos^2(\frac{\pi\Phi}{\Phi_0}) + d^2\right)^{1/4} \tag{5.1}$$

where $f_{01,max} \approx \sqrt{8E_cE_{j,tot}}$. The minimum frequency can also be found to be $f_{01,min} = \sqrt{d}f_{01,max}$. Fitting this with the data shown in Figure 5.1, we see $d = 0.67$ and we get the flux bias current corresponding to one flux quantum Φ_0. The flux bias offset in comparison to the flux bias current zero-point is due to a shift in the magnetic field due to the perpendicular coil shifting the field. An additional correction term is provided by the asymmetry. With a flux tunable qubit come a few problems. In the following sections, we will try to answer some.

5.1.1. Method for determining a quickly changing qubit frequency

On the flux tunable Dmon on this chip, there are many difficulties finding the qubit at any field, even zero field. First of all, as is discussed in Section 6, we find that it is hard to predict whether the qubit is at all visible in the spectroscopy before cooling down, let alone knowing its target frequency beforehand. Finding it the first time takes quite some effort and examples of how to find the qubit can be found in e.g. [16].
After being found, traditionally we could make a map from the qubit frequency f_q to the coupled resonator frequency f_{reso}. We use, as given in Section 1.3, the fact that the resonator shifts $\chi \sim \frac{g^2}{\Delta}$ when the qubit is in the ground or excited state, compared to an uncoupled resonator. As such, measuring only the resonator, we could also predict the qubit frequency. This is shown in Figure 5.2 for a large collection of datapoints measured at 25 mT at different angles. We see that the fit is good at high frequency, but worsens as the frequency lowers.

This mapping will only be correct when none of the following happen:

1. Using the perpendicular coil to change the flux, also affects the bare, unloaded resonator frequency, such that this mapping is only valid for a small excursion in the flux supplied by the perpendicular coil.
2. Ramping the in-plane magnet also decreases the bare frequency, rendering the mapping invalid.

There are other problems to take in consideration:

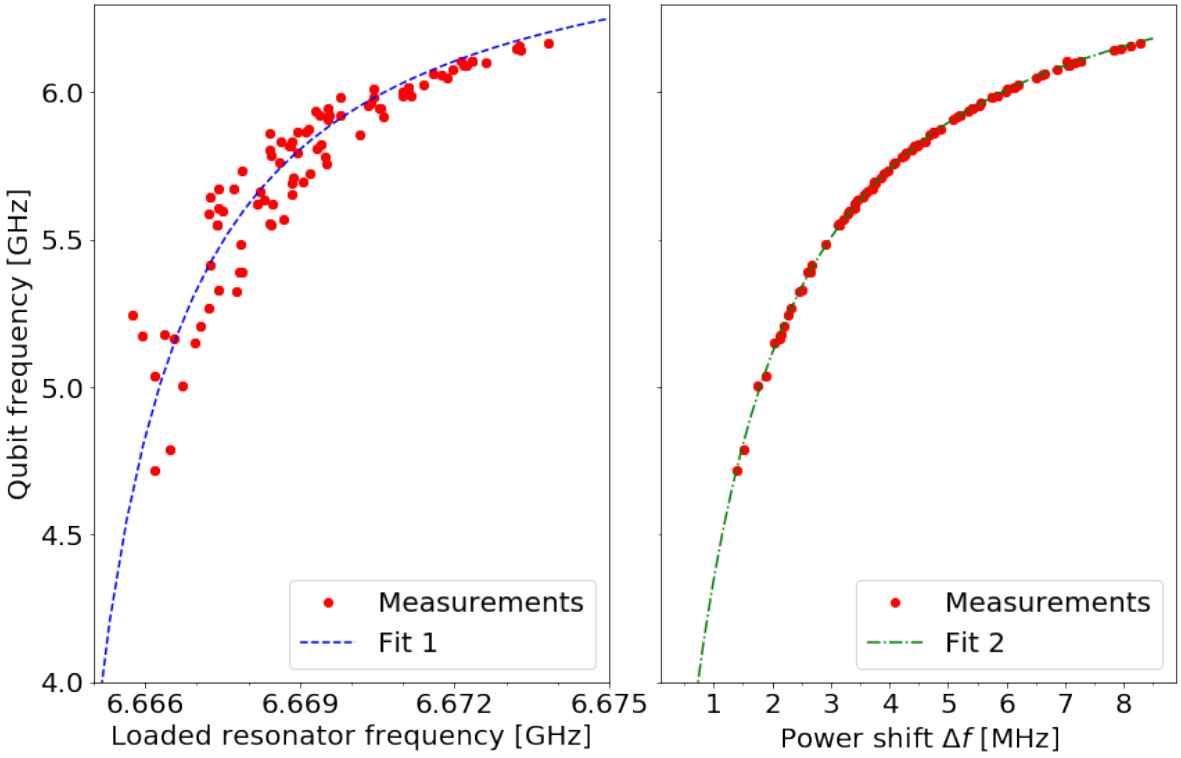

Figure 5.2: All data points were made at different in-plane angles at a fixed in-plane magnetic field of 25 mT. (Left) A fit made using the measured loaded resonator frequencies compared to the separately measured qubit frequencies. The fit uses the dispersive shift and assumes a constant f_{bare}. (Right) A fit made using the measured power shift and the measured qubit frequencies. The fit was made assuming the dispersive shift, without assuming a constant f_{bare} and introducing a correction to the frequency shift. The largest errors to the measured values are < 40 MHz.

1. While consistently aligning the in-plane magnetic field to be as parallel as possible, a flux tunable qubit is extremely sensitive to a misaligned field, and as such, the qubit frequency changes as the magnetic field changes.

2. The qubit frequency itself also reduces due to the closing of the superconducting gap at an unknown field, rendering a fixed frequency span unwieldy.

Taking all of these in consideration, we might correct for problems by measuring the bare and shifted resonator frequency and using $\Delta f = g^2/\Delta$. However, since our qubits do not guarantee that they will not be at a low frequency, the rotating wave approximation (RWA) which uses $\Delta \ll f_q + f_r$, might not hold. As such, we have tried the approach given in [58]: $\Delta f = g^2\left(\frac{1}{\Delta} + \frac{1}{2f_q - \Delta}\right)$. Even this does not satisfactorily predict the exact qubit frequency using the shifted resonator frequency as a function of power, the power shift. A better, phenomenological fit is

$$\Delta f + f_{off} = g^2\left(\frac{1}{\Delta} + \frac{1}{2f_q - \Delta}\right) \tag{5.2}$$

where Δf is the measured power shift, g the coupling between the resonator and the qubit and f_{off} is some phenomenological offset to fit the qubit frequency. The fit is shown in Figure 5.2 with a fit of $f_r \approx 6.666$ GHz, $g = 67.44$ MHz and $f_{off} = 0.55$ MHz, where f_r is the bare resonator frequency and does not need to be known precisely for the fitting procedure. This method works extremely well, even for low qubit frequencies, only having an error in prediction of 20 – 30 MHz.

5.1.2. Flux tunability at field

To measure flux noise at a higher field, we also want to have a flux tunable qubit at high fields. Using the power shift method described in Section 5.1.1. We have found that even at 245 mT in-plane field, we can tune the qubit. However, due to difficulty in finding the qubit frequency, we could not aqcuire any time domain data. We did get a clear signal of the flux tunability in the power shift as seen in Figure 5.3.

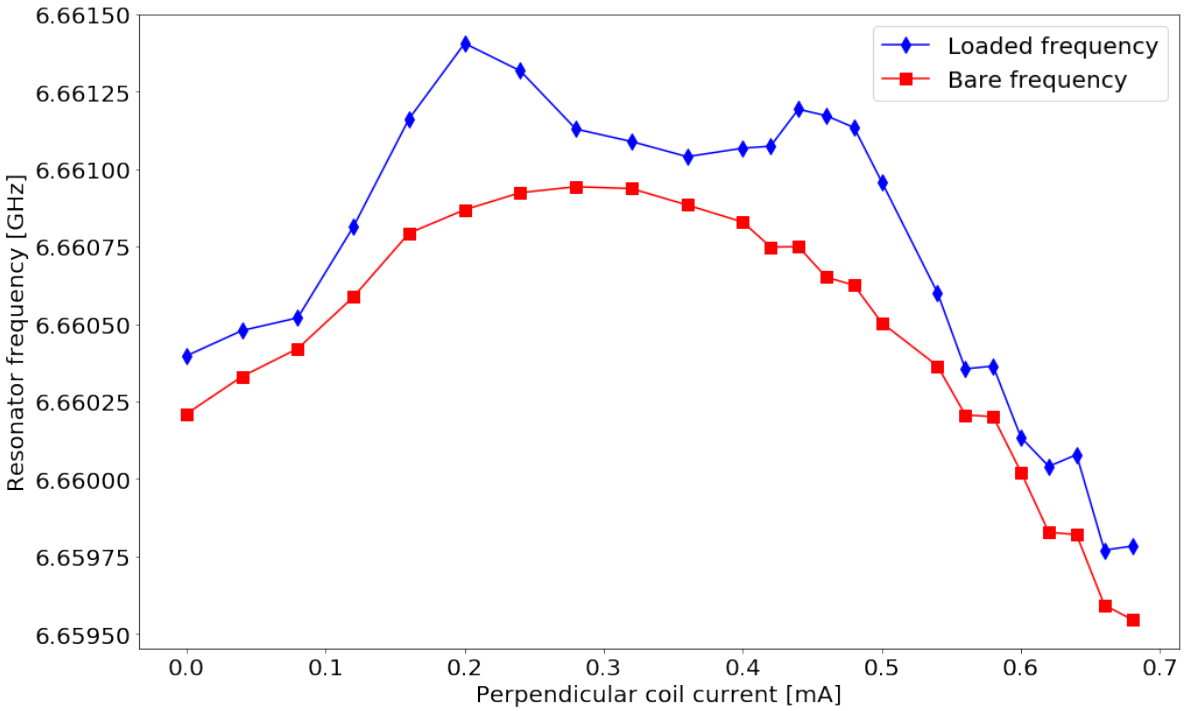

Figure 5.3: The resonator frequencies measured during a small excursion in the perpendicular field at high and low power. At low power, the resonator is shifted due to the qubit coupling. The shift is increased as the qubit comes closer. The bare frequency changes as an effect of the perpendicular field of the perpendicular coil lowering the bare resonator frequency.

5.2. Stable magnetic fields: magnet current source noise

The current source of the magnet is also a source of noise. By sampling the current in the magnet current source as measured by the magnet current source programmer, we can reconstruct the noise in the field and as a result, we can determine if this noise would influence our Echo and Ramsey measurements.
From the measured magnet source current, we can create a power spectral density (PSD), $S_{I_S}(f)$, as can be seen in Figure 5.4. Now, we will try to estimate the noise present in the in-plane field. To do this, we suppose the magnet is connected to the current source in an RL-circuit.
The R will be the equivalent resistance including the source (contact leads) resistance and the resistance of the persistent switch being normalconducting. We take a conservative estimate of $R = 0.1\,\Omega$
The inductance in the Y-axis magnet coil is 1.8 H and in the Z-axis magnet coil 0.7 H.
The RL-circuit equations would read:

$$-L\frac{dI_{mag}}{dt} = R(I_{mag} - I_S)$$

In frequency space, we can find the transfer function $I_{mag}(\omega) = H(\omega)I_S(\omega)$ with

$$H(\omega) = \frac{R}{i\omega L + R}.$$

We can now estimate the noise in the magnet current through PSD transformation law:

$$S_{I_{mag}}(f) = |H(\omega)|^2 S_{I_s}(f)$$

Following this, we can find the field in the coil by $B = C_{coil} I_{mag}$, where C_{coil} is the coil constant of the magnet, which is $49.6\,\mathrm{mT}\cdot\mathrm{A}^{-1}$ for the Z-axis and $13.2\,\mathrm{mT}\cdot\mathrm{A}^{-1}$ for the Y-axis.
We can find the field PSD by $S_B(f) = C_{coil}^2 S_{I_{mag}}(f)$. The sensitivity of the qubit frequency to the in-plane magnet field can be approximated by the equation:

$$f_{01}(B) = f_{01}(0)\left(1 - \left[\frac{B}{B_c}\right]^2\right)^{1/4} \tag{5.3}$$

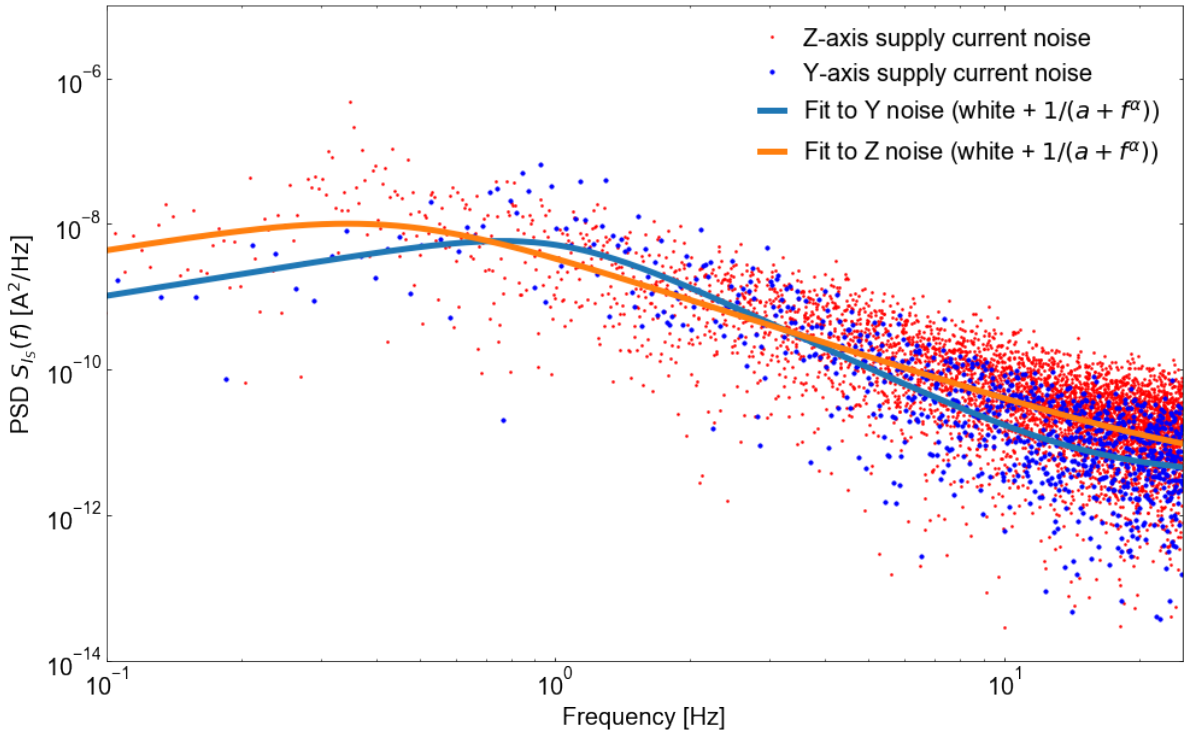

Figure 5.4: Noise measured for the Y-axis magnet current supply, and for the Z-axis magnet current supply. Fits are made using a white noise floor A_w and the function $A\frac{f}{B+f^\alpha}$, where A_w, A, B and α were free parameters. For the Y-axis and Z-axis, these values were $(A_w, A, B, \alpha) = (3.6\cdot10^{-12}, 1.0\cdot10^{-8}, 1.0, 3.87)$ and $(A_w, A, B, \alpha) = (3.7\cdot10^{-12}, 0.36\cdot10^{-8}, 0.08, 3.73)$ respectively.

and its first-order sensitivity given by

$$\frac{\partial f_{01}}{\partial B}(B) = -\frac{f_{01}(0)}{2B_C^2}\left[1-\left(\frac{B}{B_C}\right)^2\right]^{-3/4} B. \tag{5.4}$$

The dephasing of the qubit is given by (see e.g. [10])

$$\langle\Phi^2\rangle = \left(\frac{\partial f_{01}}{\partial B}\right)^2 \int df S_B(f) W(f,t) \tag{5.5}$$

where $W(f,t)$ is the filter of the measurement (e.g. a Ramsey or Spin Echo measurement) as a function of the frequency and time.
The Echo filter function is given by [34]

$$W_E(f,t) = \tan^2(\pi f t/2)\frac{\sin(\pi f t)^2}{(\pi f)^2} \tag{5.6}$$

So compiling all the equations into one, we get the resulting noise for a magnet in persistent mode at an in-plane magnetic field

$$\langle\Phi^2\rangle = \frac{f_{01}(0)^2}{4B_C^4}B^2\left[1-\left(\frac{B}{B_C}\right)^2\right]^{-3/2}\int_0^{f_q}\left[\tan^2(\pi f t/2)\frac{\sin(\pi f t)^2}{(\pi f)^2}C_{coil}^2\frac{R^2}{(2\pi f)^2L^2+R^2}S_{I_S}(f)\right]df \tag{5.7}$$

Plotting this, using $P_1 = \exp(-\langle\Phi^2\rangle/2)$ in Figure 5.5, gives an estimate of the total dephasing caused by the in-plane Y and Z magnets.
What's even more: we know that the qubit plane might be slightly misaligned compared to the magnets. This means for a flux tunable qubit that any change in the magnetic field could also cause a change in the perpendicular magnetic field penetrating the SQUID loop. This is through $\Phi = B_\perp A_{eff} = \sin(\alpha)B_\parallel A_{eff}$, where $B_\perp$ is the perpendicular component of the aligned in-plane field, A_{eff} the effective area of the SQUID loop and α

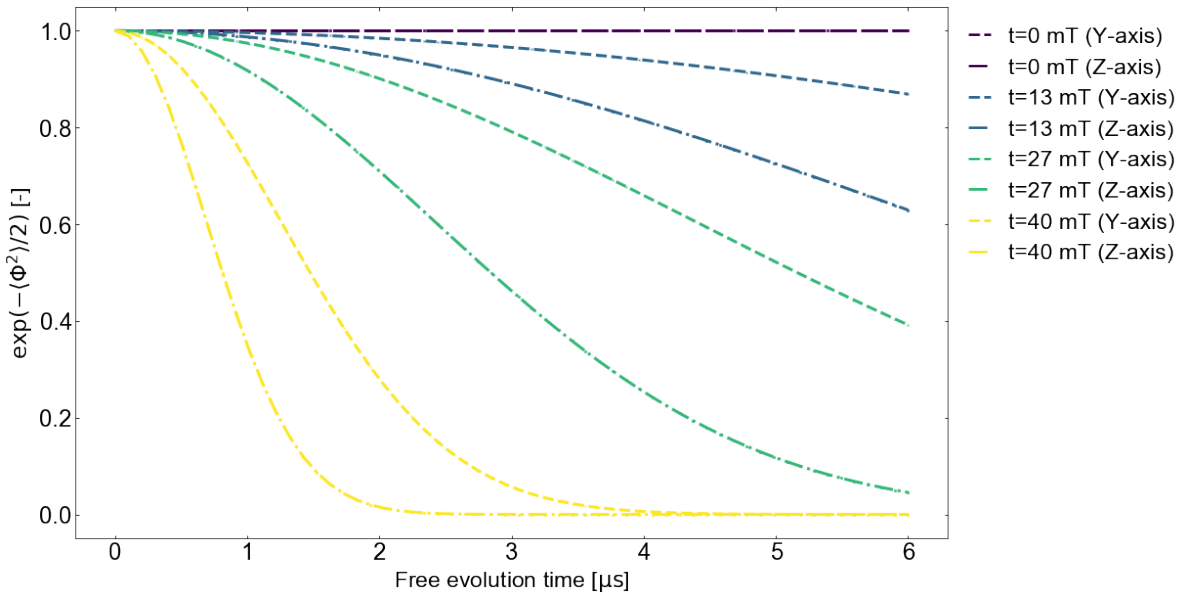

Figure 5.5: Result on the Ramsey if no other effect was present except for dephasing due to the noise in the magnetic field. Assumed was $B_c = 45\,\mathrm{mT}$ as was measured in one of the qubits.

the misalignment in angle. $\alpha = 0$ means perfectly aligned. Through misalignment of the chip in the sample holder, we can cause in-plane field noise to propagate to the perpendicular field as

$$S_{B_\perp}(f) = \sin^2(\alpha) S_{B_\parallel}(f) \tag{5.8}$$

We can now repeat the analysis, using the first-order sensitivity of the qubit to the SQUID flux changing using Equation (1.6)

$$\frac{\partial f_{01}}{\partial \Phi} = -f_{max}\frac{\pi}{2\Phi_0}\frac{(1-d^2)\cos(\pi\Phi/\Phi_0)\sin(\pi\Phi/\Phi_0)}{\left((1-d^2)\cos^2(\frac{\pi\Phi}{\Phi_0})+d^2\right)^{3/4}} \tag{5.9}$$

This means the SQUID is sensitive to changes in the perpendicular magnetic field, so Echo and Ramsey experiments are further affected negatively. We have found that at field, the Y and Z-axis magnets cause dephasing due to noise in the current source. This happens for all qubits, even gatemons and non-tunable qubits. This means that at field, Ramsey measurement T_2^* will be dominated by magnet current noise. Echo experiment T_2^e are not affected significantly. Next to that, flux-tunable qubits have the extra dephasing channel of misalignments. This affects both the Ramsey and Echo experiments significantly. The advice is: for flux-tunable qubits, the magnets should be operated in persistent current mode, where the current source is essentially disconnected from the magnet, to prevent current noise from dominating the Ramsey and Echo experiments. For non-flux tunable qubits, it might be sufficient to measure in non-persistent mode when at low fields $B \ll B_c$.

5.3. Measurement of a continuous frequency arc vs. flux

We have seen that we have a flux tunable qubit. However, there are difficulties in measuring the full flux arc. Since the Y and Z-axis magnet fields drift, the SQUID loop might feel a drift in the flux bias offset due to this. A solution had been implemented: decrease the SQUID loop size. However, now we have the problem of the SQUID loop not having sufficient sensitivity to flux to completely characterize one full flux quantum. To resolve this, we have tried to use the perpendicular X-coil as a flux bias. This has the range of several flux quanta. However, there is the problem of flux jumps, as we will discuss in Section 5.3.1. This happens when using the perpendicular coil. To get a full flux quantum of continuous qubit measurement, we need to use the perpendicular coil and the flux bias line in tandem.

5.3.1. Flux jumps

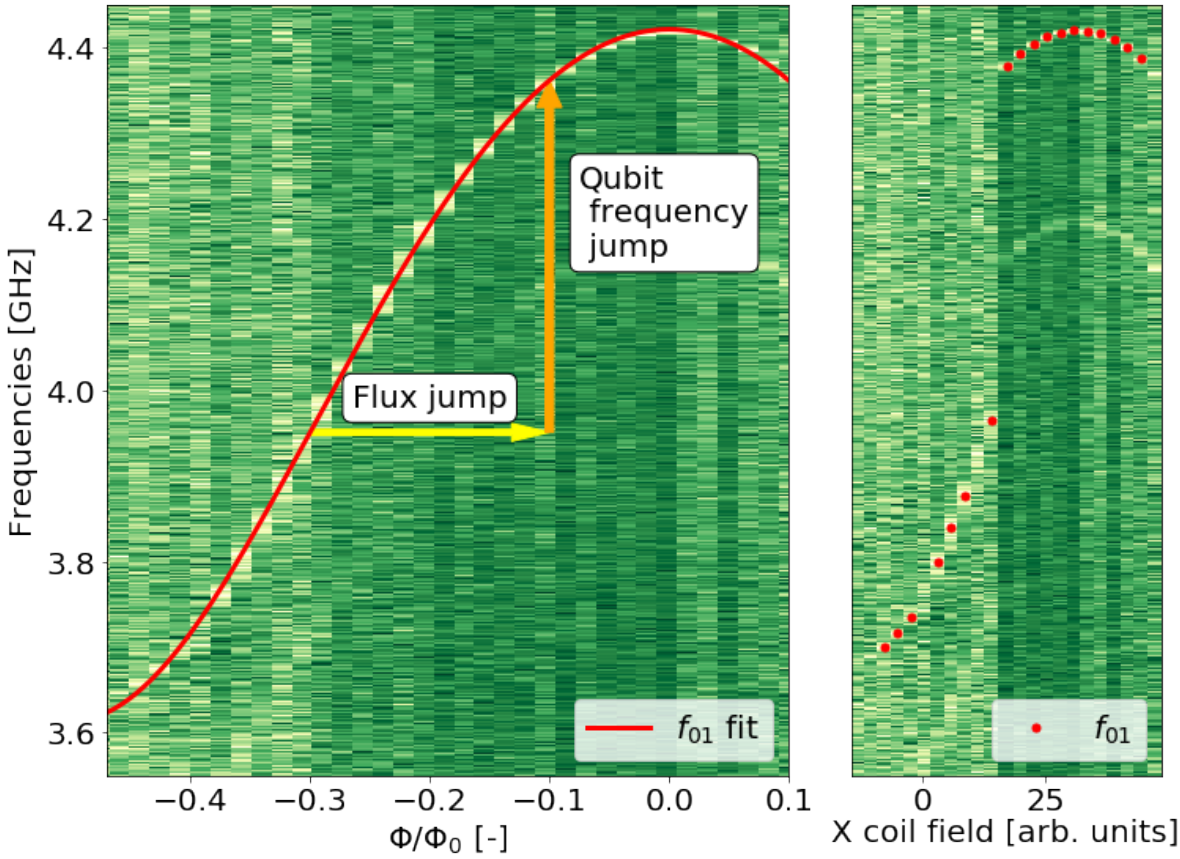

Figure 5.6: A (mock) example of a flux jump. (Left) A typical flux arc without flux jumps. (Right) A situation where the flux bias using the perpendicular coil is swept up and a flux jump occurs.

What are flux jumps? There are qubit frequency jumps in the spectrum of the qubit while sweeping the field perpendicular to the plane. This can be explained by flux jumps, which are depicted in Figure 5.6. Since the qubit is sensitive to the magnetic field applied to its SQUID loop, the qubit frequency changes as the flux changes. If the flux jumps discontinuously, the qubit frequency jumps discontinuously as well. This limits the possibility of measuring the flux noise, since the way to measure flux noise, is to use the fluctuating qubit frequency as detector for the flux noise. Two main hypotheses are given for the discontinuous flux jumps:

1. The presence of a superconducting loop around the SQUID, in which the magnetic field tries to penetrate the outer superconducting loop. The outer loop responds by coursing a current to resist creating a flux. This continues until the total flux Φ inside of the outer loop exceeds $+\Phi_0$ or $-\Phi_0$, after which the superconducting ring imposes the flux quantization constraint $\Phi = n\Phi_0$ where $n \in \mathbb{Z}$. The total flux then jumps to a multiple of Φ_0 and a small part of the magnetic field will thread the loop. As a result, the smaller SQUID loop also gets affected by the different magnetic field, and a flux jump is visible.

2. The trapping of flux in vortices of the superconductors near the SQUID loop, since one vortex changes the total field going through the SQUID itself. This would also be visible in the resonator frequency by changing its kinetic inductance.

5.3.2. Flux jumps due to a superconducting loop in the system

One example of flux jumps happening on the qubit can be seen in Figure 5.7(Top). The qubit frequency does not change as the perpendicular field to the SQUID is changed. The jumps happen at intervals (which happen to be the same during each sweep) and have an hysteresis effect which is observed when the sweeping direction changes. A further investigation using the same data can be found in Figure 5.7(Bottom). We can

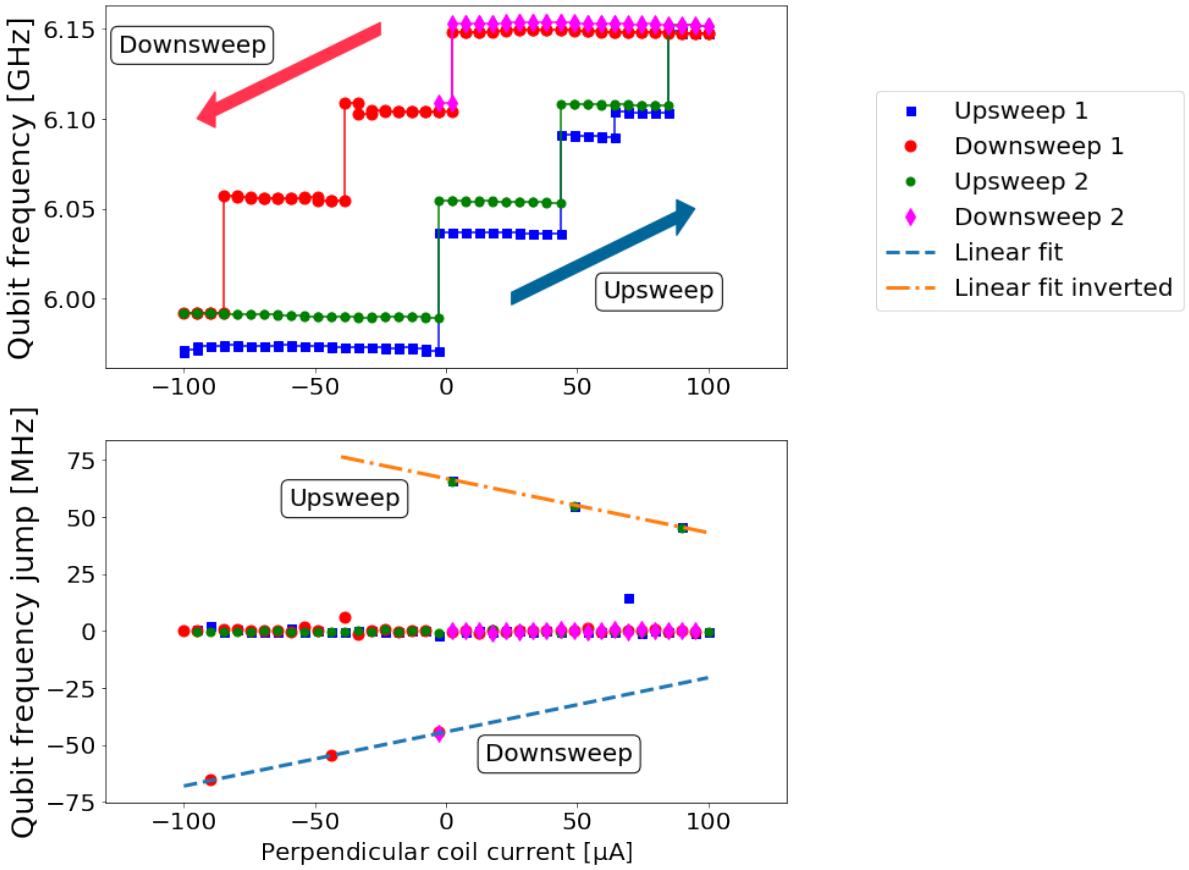

Figure 5.7: The perpendicular coil current, providing a flux bias to the SQUID of the qubit, was swept up and down. Starting from −0.1 mA, keeps sweeping between −0.1 mA and 0.1 mA. (Top) The qubit frequency as measured during the sweeps. The red and magenta colours indicate downwards sweeps and the blue and green colours indicate upwards sweeps. (Bottom) The qubit frequency change in during an up or down sweep between two consecutive (in time) measurements. A linear fit $f_q = 0.2375 \cdot I_{coil} - 44.3$ was made to the jumps present, where I_{coil} in μA and f_q in MHz to reveal a linear dependence. A second fit was made with the exact same function inverted and shifted by 95 μA so that $f_{q,fit}(I_{coil}) \rightarrow -f_{q,fit}(I_{coil} - 95\,\text{mA})$. All areas where no jumps happened stay close to zero change, as expected.

see that the qubit frequency difference that happens when the flux jumps, follow a linear relationship with the perpendicular coil current. This means the flux jumps are evenly spaced and small compared to the flux arc of the qubit. The flux threading the SQUID loop is on the slope of a flux arc which can often be well approximated by a parabola, explaining the linearity of the differences. Since in the up sweeps, the qubit frequency increases again, the qubit frequency difference follows exactly the same fit. We assume this hysteresis effect to be due to the outer loop being able to create a counter-current to form $\Phi = -\Phi_0$ to $\Phi = +\Phi_0$. This would imply that the hysteretic shift is exactly $2\Phi_0$ of the outer loop, which gives the precise current at which one jump happens: $I_o = 42.5\,\mu\text{A}$.
To give an indication of the area that this loop should have, we examine the constraint for a flux jump: $\Phi_0 = A_{eff} \cdot B_{app}$, where A_{eff} is the effective area of the loop and B_{app} the applied field. Due to the magnetic field not being able to penetrate a superconductor, the magnetic field lines might bend through the loop hole, increasing the flux more than only the hole area A_{hole} would predict. This is called flux focusing. As such, we include a factor f_{focus} to account for this. This factor can have a value ranging from 2/3 to 20 − 30 depending on the material and geometry of the SQUID. We can also determine the applied field from the coil current by imposing that the applied field is linear in current: $B_{app} = C_{coil} I_{coil}$.
Doing this for both the outer loop and the SQUID loop, we find the relation:

$$\Phi_0 = f_S I_S C A_S = f_o I_o C A_o \tag{5.10}$$

Where the subscript $\square_S$ denotes the SQUID loop and $\square_o$ the outer loop. f is the flux focusing factor, I the coil current necessary to give one flux quantum and A the area of either loop. We find I_S through guessing one

period of the qubit arc vs flux. We find I_o by analyzing the interval between jumps.
Using the SQUID loop hole dimension $6\,\mu m^2$ and assume a strong flux focusing factor of $\frac{f_S}{f_o} = 20$, and eye-balling one flux period of the SQUID being $I_S = 300\,\mu A$, and using $I_o = 42.5\,\mu A$, we find the outer loop area to be $A_o = 850\,\mu m^2$.
However, in photo's of the qubit junction structure, no small loop as such can be found.

5.3.3. Flux jumps due to a vortex in the superconductor

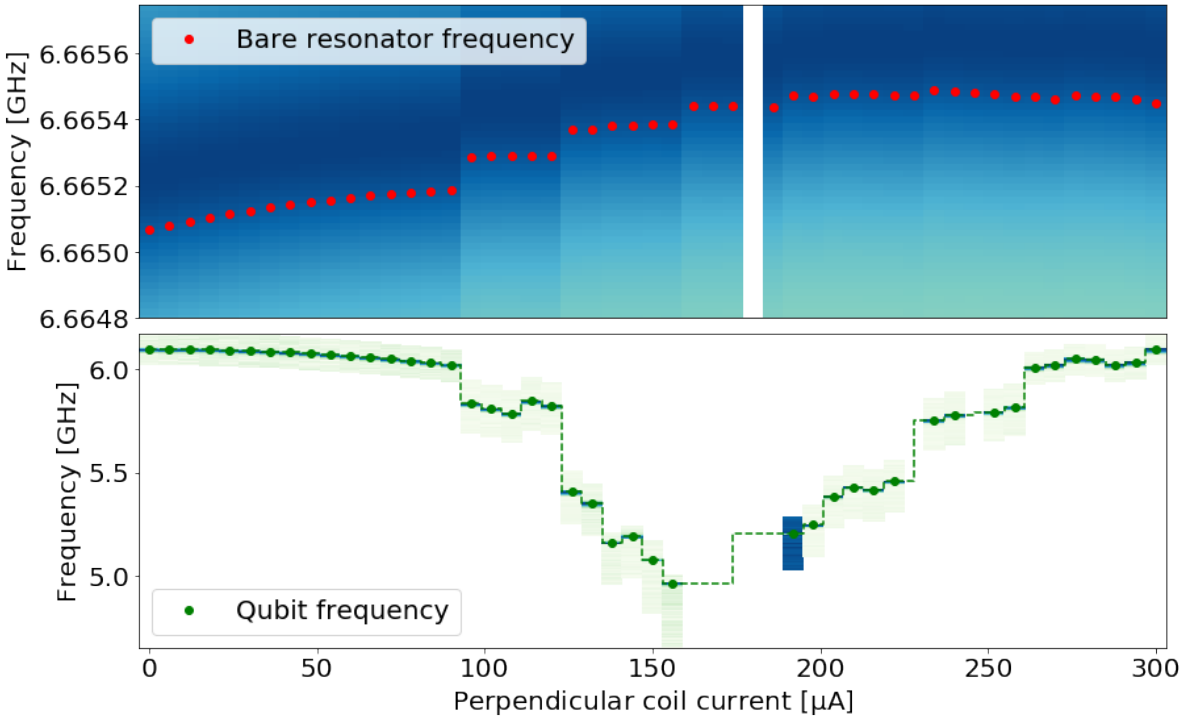

Figure 5.8: The result of sweeping the perpendicular coil current, used as flux bias, upwards from 0 to 300 μm. (top) A measurement of the transmission $|S_{21}|$ for every perpendicular coil current measurement. Only a part of the bare resonator frequency measurement is shown to increase the resolution. We can some polynomial tendency in the bare resonator, in addition to discontinuous jumps. The green dots indicate the fits to the resonator frequency dip. (bottom) The found qubit frequency for every perperdicular coil current. The green dots are the fits to the qubit frequency, and the green dashed line is a guide to the eye for discontinuous jumps.

The other explanation would be the creation of vortices in the superconducting film near the SQUID loop. We can see in Figure 5.8 that the jumps in the qubit frequency correspond to the jumps in the bare resonator frequency. This is what we would expect to see when vortices would be created. As reasoning, we can see that the qubit frequency is uncorrelated with the bare resonator frequency, which leads us to believe that the qubit does not have an effect on the resonator (like the dispersive shift on the loaded resonator frequency as in Equation (1.4)). Moreover, the jump heights of the bare resonator frequency do not correspond to the magnitude of the jumps of the qubit frequency. We therefore believe that the jumps are due to a third factor: the creation of a vortex near the SQUID.

5.4. Flux noise measurements

We have measured flux noise in a chip (see Figure 5.9). The characterization of the flux noise at field is still in progress. To measure the flux noise, we have done a flux sweep and measured the corresponding T_1s and T_2^es. We have fit the measured flux by using the flux arc and the frequency. We have then changed the sensitivity of the frequency by taking the derivative $\frac{df}{d\Phi}$, as done in Section 5.2. We have calculated the T_ϕ as defined in Equation (3.1). After fitting the dephasing rate vs. the flux sensitivity of the qubit at different fluxes, we can extract the flux noise amplitude. We have assumed $S_\Phi(f) = \frac{A}{f} + \sigma$ where σ is white noise and have found $\sqrt{A} \sim 1000\,\mu\Phi_0$, higher than expected.

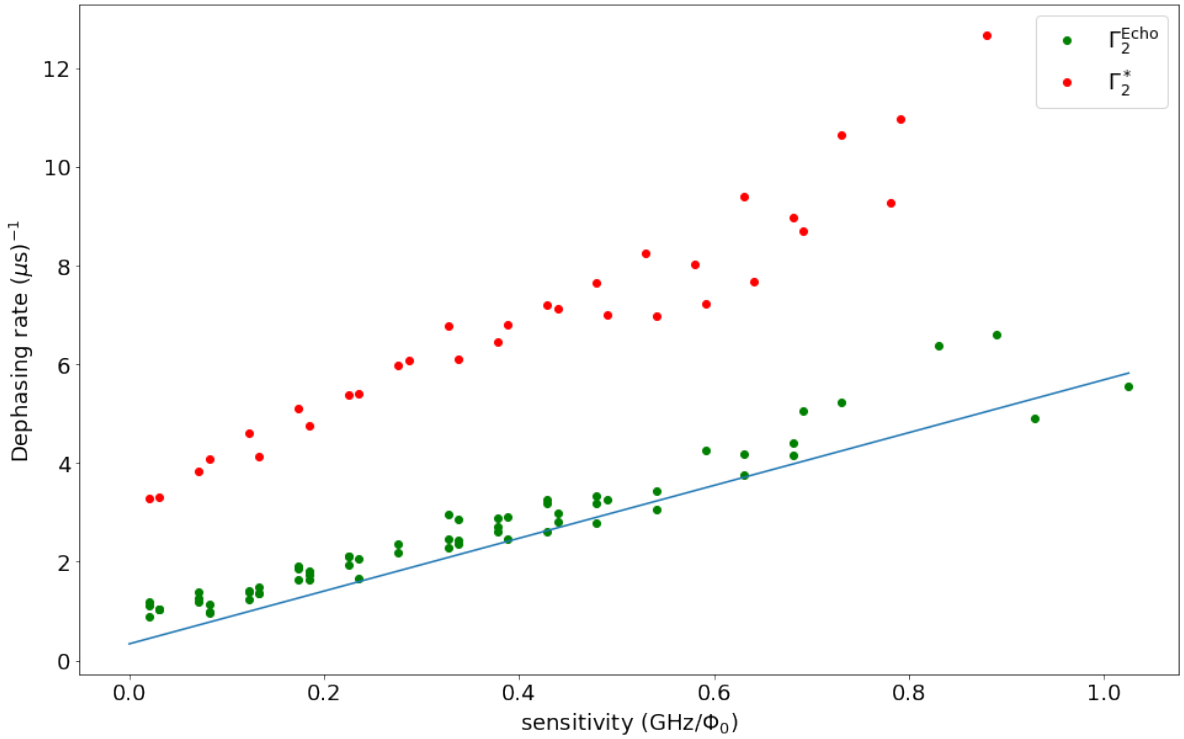

Figure 5.9: The dephasing rate, calculated using the Echo times (green) and the Ramsey times (red). The Echo times have been fit to find the flux noise amplitude at 1 Hz

6

Statistical analysis of nanowire junction room temperature resistances

A quantitative measurements of the nanowire we can do before cooling down the chip, is to measure the room temperature resistance. For SIS Josephson junctions, we can predict the qubit frequency of a transmon by measuring the room temperature resistances of the two contact pads besides the junction. This is due to the Ambegaokar-Baratoff relation, linking the measured normal resistance and the Josephson junction critical current together [1]. We would like to investigate if the room temperature resistance for nanowire junctions also can tell us something about the qubit properties. It turns out that we cannot yet predict qubit performance through this proxy measurement, but there definitely is a correlation in the chance of a qubit being measurable and the measured resistance at room temperature. In the following sections, we will explain our data analysis method and probable causes of low performance chips.

6.1. Data analysis

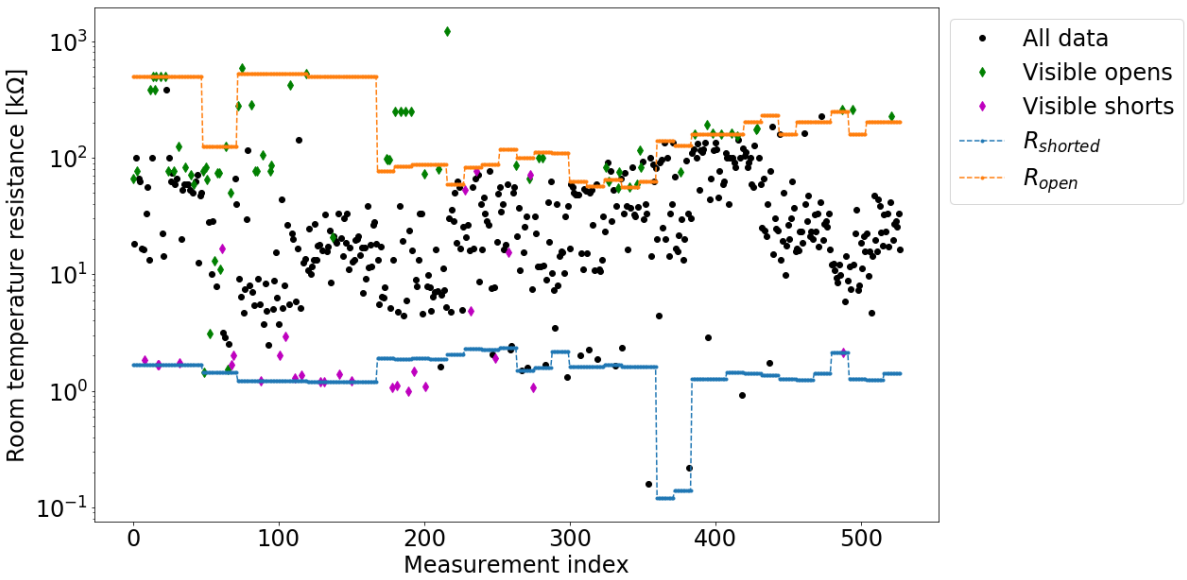

Figure 6.1: All data since January 2018 collected on room temperature resistances of nanowire transmon junctions. All shorted and open junctions were only determined using microscopy images. Fabrication was done in batches of 4 chips yielding 48 measurements (or less in case of failure) per batch. The measurements presented here are in chronological order.

Due to well-documented fabrication details, we could collect data on the nanowire junctions used since January 2018. To fabricate nanowire transmons, nanowires are placed in the junction area, dark field microscopy images are taken to determine the exact location of the nanowires. Then the image recognition software [42]

creates contacts to connect the nanowire to the transmon. The contacts may form different structures forming different types of tunability. Creating a voltage bias side gate ~ 200 nm next the nanowire creates a Gatemon. Forming a SQUID loop, containing two Josephson junctions using the single placed nanowire creates a Dmon. Just connecting the two ends of the nanowire to the contacts creates an untunable transmon. Several problems may arise in this process:

1. The nanowire is not placed correctly or is washed away, before liftoff, creating an open or shorted junction.

2. The image recognition software did not recognize the nanowire in the junction area, creating an open or shorted junction.

3. The image recognition software accidentally overlapped the two superconducting contacts, creating a short.

4. The position calibration of the contacts fabrication drifted, so that the etched contacts do not overlap the nanowire, creating an open junction.

5. The nanowire, after etching the contacts, was washed away, creating an open junction.

All the subsequent data collected includes: designed type of qubit, presence of airbridges on chip, maximum power shift measured, maximum qubit frequency measured, the g-coupling between resonator and qubit, maximum T_1, T_2^e and T_2^* measured, measured tunability of qubit, voltage threshold before power shift presence and maximum predicted field compatibility.
To give an indication of the resistances due to other effects while probing the nanowire resistance, two transmons without nanowires are on the chip. One is shorted with a strip of NbTiN and the other does not have a contact at all, mimicking an open. As such, we can measure two more values for every chip: shorted resistance R_s and open resistance R_o. With these, we can retrieve a better estimate of R_{NW} through the simple equivalent R calculation:

$$R_{NW} = \frac{R_m R_o}{R_o - R_m} - R_s \tag{6.1}$$

where R_{NW}, R_m, R_o, R_s are the nanowire resistance, the measured resistance, the open resistance and the shorted resistance respectively. The measured room temperature resistances are shown in Figure 6.1. We can see a clear band of measurements present in the data. The junctions that were visibly shorted or open seem to create their own bands at low resistances and high resistances respectively. At measurement index 217, the image recognition software improved, improving the yield.
Only a fraction of these chips went into the refrigerator and were cooled down. For these junctions, we have data about the presence of a power shift, indicating a measurable qubit. This is shown in Figure 6.2. It seems that low resistances lead to measurable qubits. We like to investigate quantitatively what we can say about this.

6.2. Probability distribution of resistances

Since we have around 500 data points of junction resistances, we can apply a statistical treatment to the data to find a distribution. We use a empirical cumulative distribution function (ECDF) to see if there is a distribution that describes the collection of resistances well.
We fit the resistances to the ECDF using the method described in [5], using Fourier expansion and a two-sided Kolmogorov test to find a smooth probability density function that is statistically indistinguishable from the data as shown. The results are shown in Figure 6.3.
Fitting this to all available data, we find the sum of two log-normal distributions where $\log_{10}(R_{NW}) \sim \mathcal{N}(\mu_1, \sigma_1) + \mathcal{N}_2(\mu_2, \sigma_2)$. The second peak centered at 280 kΩ is most likely an indicator that the junction has an undetected open. The first peak then is the distribution of working nanowire junction resistances. The resistancs are centered around 20 kΩ, indicating a mean resistance higher than optimal, as we will see in Section 6.3.
Since a log-normal distribution normally appears when there is a multiplicative process going on, such as percentage growth, this might give insight into why the nanowires have this distribution.

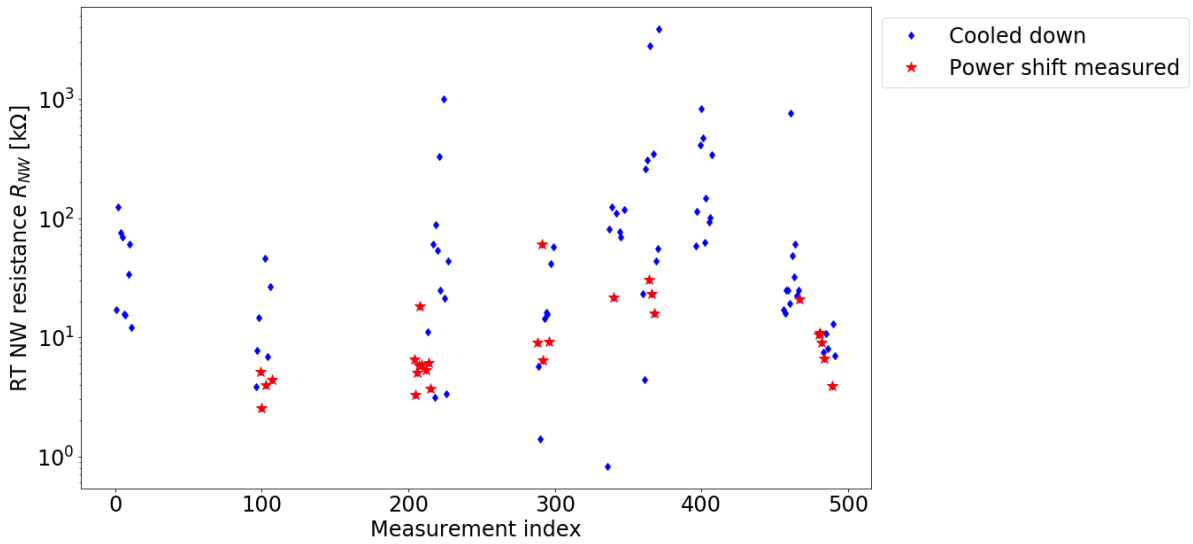

Figure 6.2: All data since January 2018 collected on room temperature resistances of nanowire transmon junctions cooled down. Only junctions are graphed in case no visible short or open was detected. The measurements index is the same as Figure 6.1.

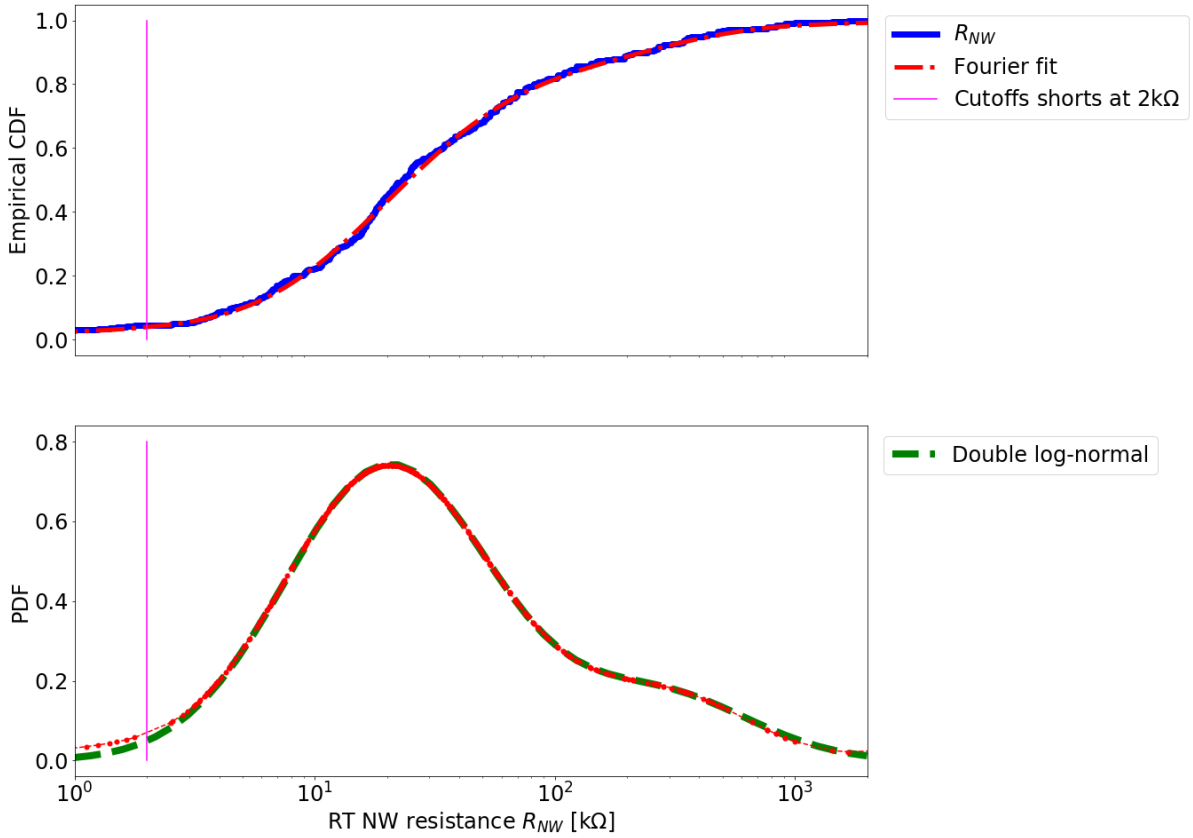

Figure 6.3: Empirical CDF data of junction data. (Top) The empirical distribution with a fit using the method described in [5]. (Bottom) The corresponding PDF that fits the CDF. Each dot represents one measurement. The log-normal distribution uses parameters amplitude $A = 0.80$, mean $\mu = \log_{10}(20.5\,\text{k}\Omega)$, variance $\sigma = 0.43$ for the high peak and $A = 0.15$, $\mu = \log_{10}(280\,\text{k}\Omega)$ and $\sigma = 0.37$.

6.3. Prediction of qubit measurability

We have also measured 26 power shifts throughout the year, of which 22 were a qubit with measurable properties, such as the qubit frequency. The room temperature resistance of the nanowires does not seem to correlate with the maximum measured power shift. It is therefore hard to determine a link between the qubit

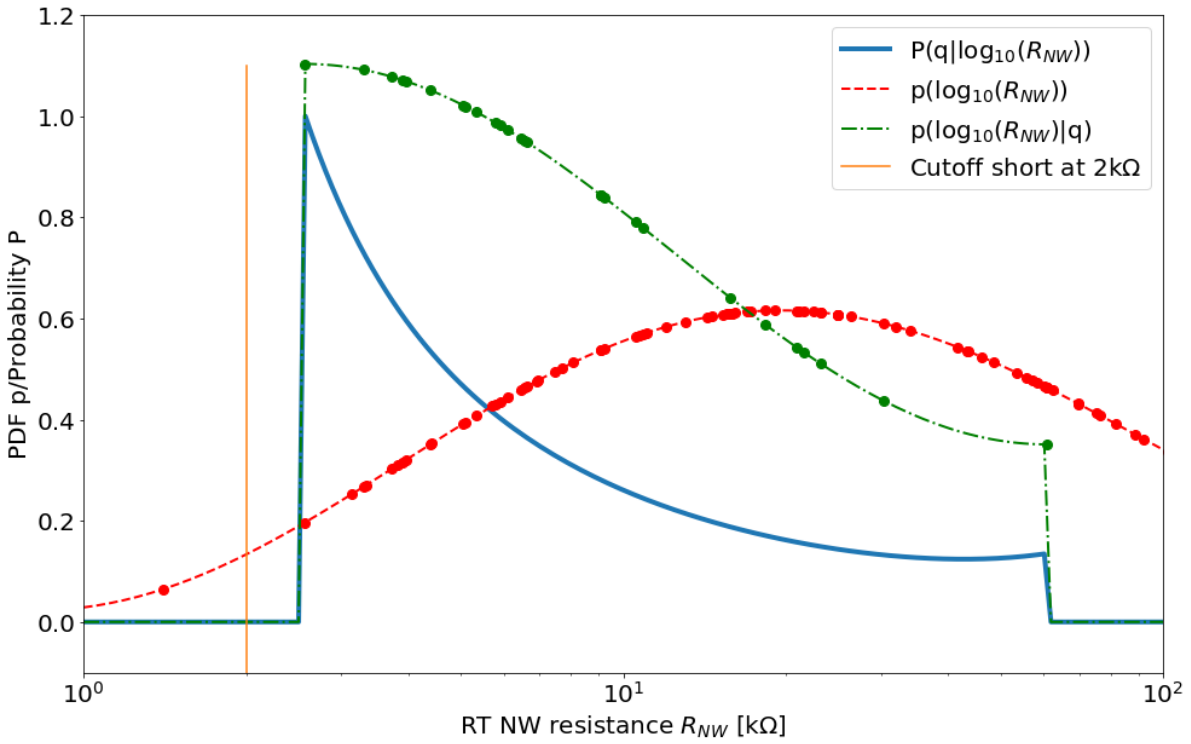

Figure 6.4: The probability of any qubit working found using Equation (6.2). Also shows are the fitted pdfs for the nanowire resistance R_{NW} calculated by Equation (6.1). The dashed lines are constituents of the Bayes theorem to find the desired fit. All measurements are shown as dots on the dashed lines.

frequency and the junction resistance. What we can do, is find the probability that a qubit can be found given a certain resistance.
This can be done using Bayes' theorem:

$$P(q|\log_{10}(R_{NW})) = \frac{p(\log_{10}(R_{NW})|q)P(q)}{p(\log_{10}(R_{NW}))} \tag{6.2}$$

where $P(q|\log_{10}(R_{NW}))$ is the probability that we can measure a qubit given a certain calculated R_{NW}, $p(\log_{10}(R_{NW})|q)$ the Probability Distribution Function (PDF) of the R_{NW} given that we have measured a qubit, $P(q) = \frac{\#\text{ of qubits}}{\#\text{ of cooled junction}}$ the probability of a qubit working in general, and $p(\log_{10}(R_{NW}))$ the PDF of the R_{NW}. We use the R_{NW} in log-space for ease of use. We can see the result in Figure 6.4. A clear dependence on the room temperature nanowire resistance is visible. We see that the one measurement at 2.5 kΩ is the lowest measurement which corresponds to a qubit. Between 2.5 and 5 kΩ, the chance of having a measurable power shift is > 50%. However, the success rate drops significantly as the resistance goes higher. Junction resistances higher than 80 kΩ have not yet provided a measurable qubit. We can approximate the given curve by

$$P(q, R_{NW}) \approx \begin{cases} 0 & \text{when } R_{NW} < 2\,\text{k}\Omega \text{ or } R_{NW} > 80\,\text{k}\Omega \\ \frac{0.27}{\log_{10}(R_{NW})^{1.4}} & \text{when } 2 < R_{NW} < 80\,\text{k}\Omega \end{cases}. \tag{6.3}$$

We will assume that this probability is independent of factors such as: aging, fabrication differences or NbTiN wafer differences and differences between nanowire batches. This due to having insufficient data points for each of the separate categories.

6.4. Batch differences

It can be seen that in one single batch of chips, made with the same fabrication process simultaneously, that the separate chips generally follow the same distribution. However, between batches from different fabrication cycles, the resistances differ substantially. This can be seen in Figure 6.5. This implies that the quality of the nanowire resistances, in which lower is better, is only dependent on the differences between batches. We

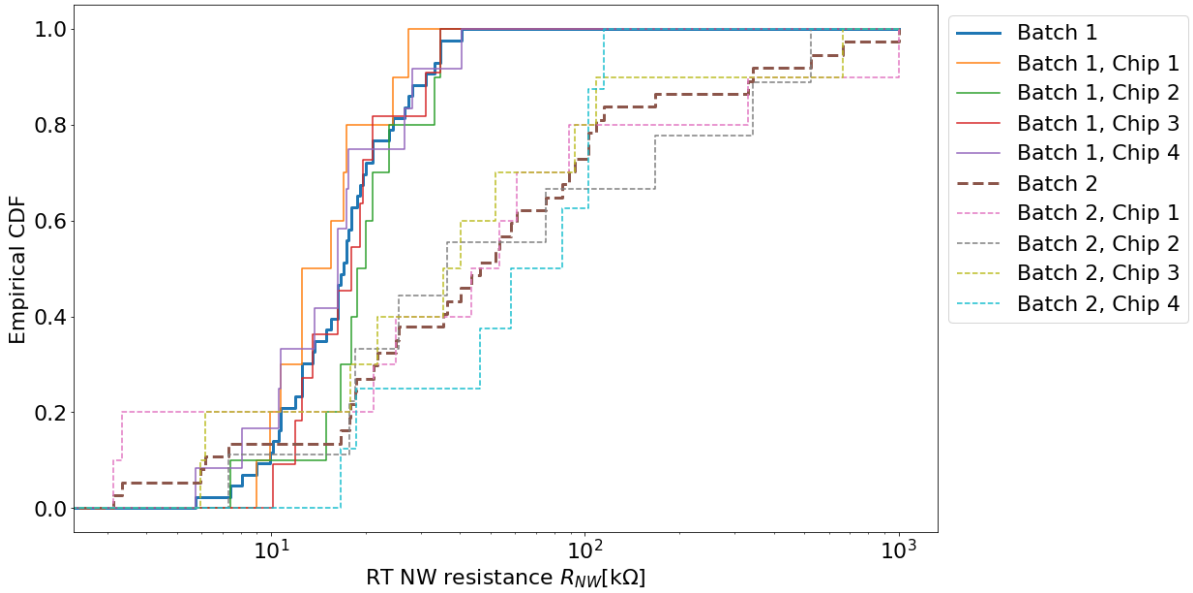

Figure 6.5: The empirical CDF functions for two different batches. The thick lines represent all data from one batch. The thinner lines are separate chips from that batch. The solid lines and dashed lines represent two different batches.

try to explain these differences in the following sections using the presence of airbridges and due to nanowire aging.

6.5. Effect of airbridge fabrication

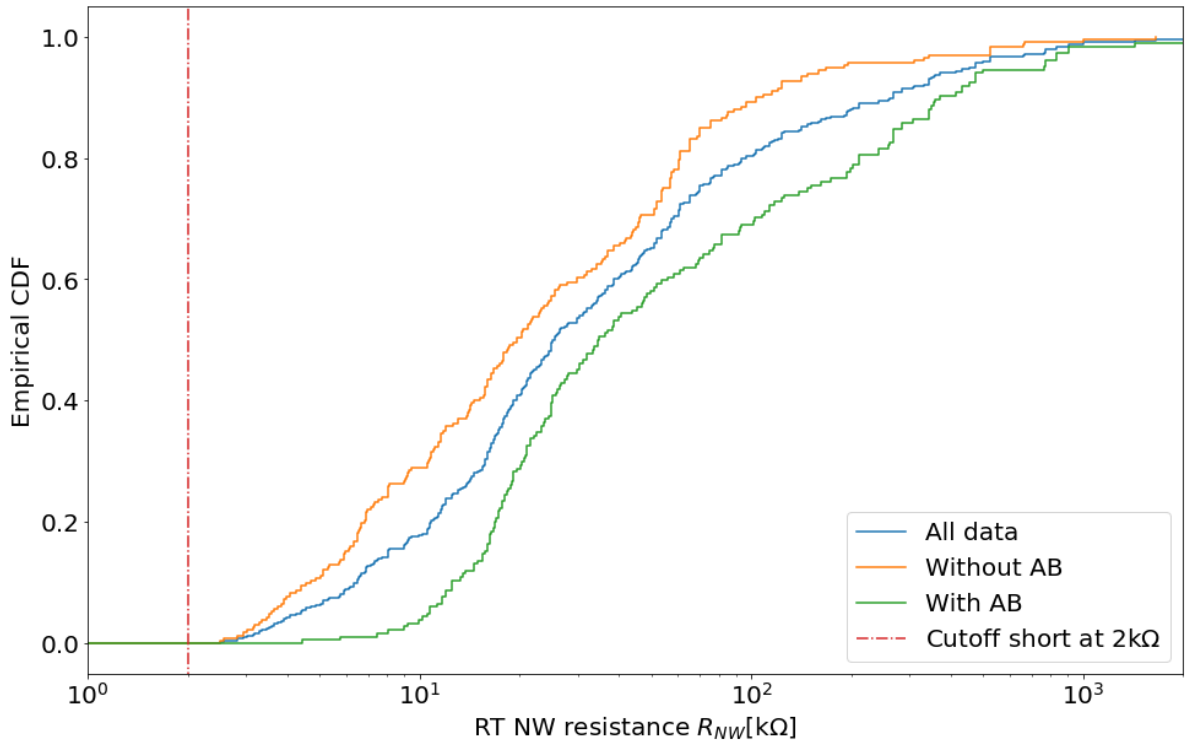

Figure 6.6: The empirical CDF functions comparing chips with airbridges or with on-chip wirebonds. The blue line depicts all data available in the dataset, the orange line all junctions on chips where airbridges (AB) were fabricated. The green line depicts all junctions where no ABs were present.

For this, we use the complete dataset, excluding the obvious visible defects such as opens and shorts, and using the R_{NW} as a method of determining the effect of e.g. fabricating airbridges. We have compared datapoints for junctions where airbridges were fabricated to junctions where on-chip wirebonds were used. Airbridges have as a function to ground the on-chip plane next to the various resonators, to suppress odd modes. We show the differences in the junctions on chips with airbridges and no airbridges in Figure 6.6. We see that the fabrication of the airbridges has a clear effect on the distribution of resistances. At least a factor 2 or 3 increase can be seen in the measured resistances. From Figure 6.2 we can read that this factor of 2 or 3 decreases the probability of finding a measurable qubit by about 70%.

6.6. Effect of aging

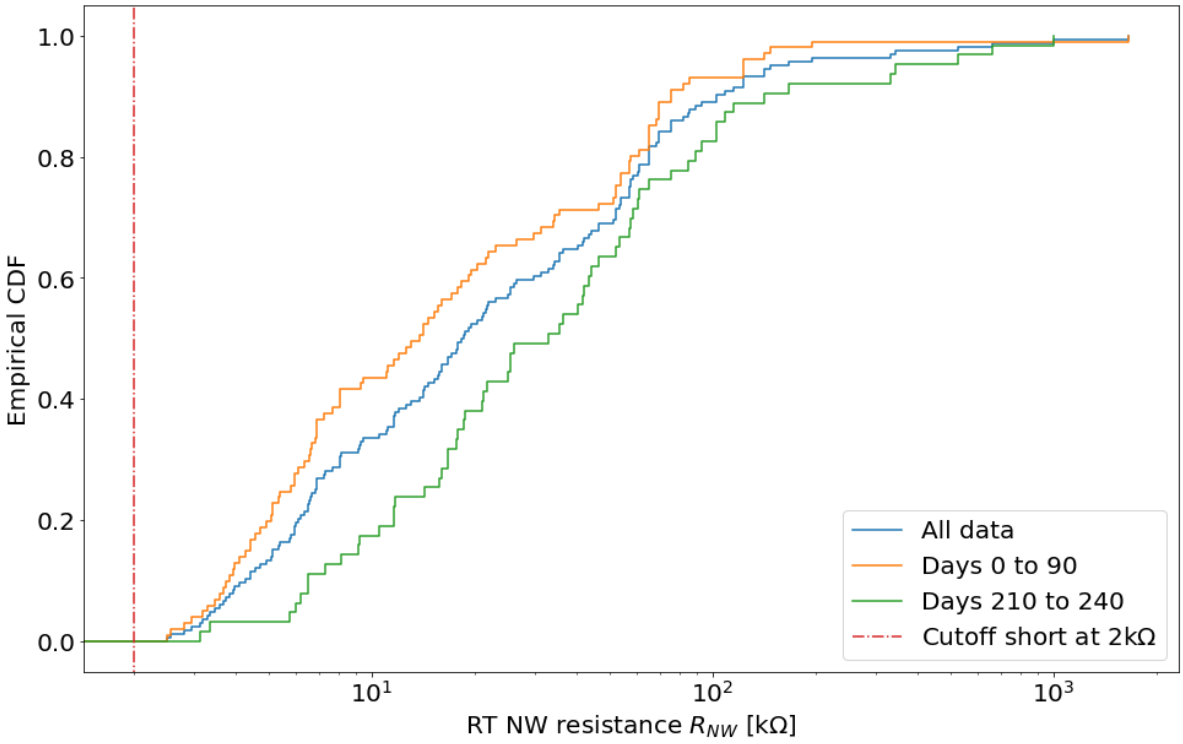

Figure 6.7: All data from chips produced around the start of 2018. These are junction measurements on chips without airbridges and from the same nanowire batch.

To investigate the effect of aging on the nanowires, we select all junctions from the dataset without airbridges (which have been shown above to have a big effect on the resistances) and the same nanowire batch. To see a difference between batches, we look at junction resistances during two separate periods and see if there is a significant difference. This is shown in Figure 6.7.
We see a significant difference, even though no airbridges were involved. As such, we must conclude that the aging of the nanowires will influence the qubit quality as well. The quality of the vacuum in which the nanowires are stored may be an important factor.

6.7. Other effects

There is no discernible effect of the qubit position on the resistances or the amount of shorts (not shown). There is no discernible effect between the different types of qubits (Gatemons or Dmons) (not shown). There might be an effect due to different types of nanowires, but we cannot control it for the airbridges and the aging variables. Since from all qubits, the T_1 and T_2^e were also measured, we have found that these correlate and that the maximum measured $T_2^e \approx T_1$. We also find that the tunability of the Gatemons are quite consistent when measurable, while the tunability of Dmons has only a 50% success rate when measured.

6.8. Further research

We still do not know the physical significance of the nanowire resistance at room temperature and its relation to its superconducting properties. Also, the reason for having a log-normal distribution is not immediately obvious.

A dataset is kept in .csv -format for future research, and hopefully, more data will be added in the future to extend these investigations.

We have not yet tried to fit the effects of aging and airbridge fabrication simultaneously, which might give reveal a better explanation for the shift in nanowire resistances. Another way to gain more information, is to fit every batch with a log-normal distribution, and see if a pattern emerges from the resulting log-mean and log-variance.

The data supports revising and improving the image recognition software for a higher yield, and investigating different processes in the fabrication process. A rise in resistances after executing a process might give insight into the nanowire failure modes.

7

Conclusions and prospects

The flux tunable nanowire transmon is a suitable qubit to use as a sensitive quantum sensor for measuring flux noise in a magnetic field.
The room temperature resistances of the nanowires in the transmon junctions have been collected and show that the resistances in general follow a log-uniform distribution. There are big differences in the mean and spread of this distribution between each fabrication cycle consisting of 48 nanowire junctions. Different chips from the same cycle show similar distributions.
The resistances of the nanowire junction are a good proxy to knowing whether the nanowire transmon will be measurable or not. A room temperature resistances of $2-3\,\mathrm{k}\Omega$ predicts that the transmon is almost gauranteed to be measurable. The chance of success halves every $2-3\,\mathrm{k}\Omega$ increase. The shift of the mean of the distribution is correlated strongly with the fabrication of airbridges and with the aging of the nanowire. No discernible correlation of the nanowire resistances were found with the positions of the qubit on the chip, the qubit type (gatemon or Dmon) or nanowire batch. There might be no correlation with qubit frequency or success of tunability, but we need more data points from measurable qubits to support this.
The chip design code has been ported to PyQip3, to speed up design iteration. A relation between the elbow coupler length and the coupling quality was found for this chip design. To improve readout, the coupling quality factor was increased, sharpening the peaks of the resonators. This worked as expected. The resonator targeting shows a deviation from the targeted frequency. This deviation depends on the qubit being on one or the other side of the feedline.
The behavior of a nanowire transmon qubit in a magnetic field was investigated. An alignemnt procedure for aligning the magnetic field on the qubit plane has been tested. This procedure ensures that the perpendicular field is zero and the field is entirely in the transmon plane. The alignment is performed on a nearby resonator and it is found that maximizing the resonator frequency of a resonator nearby the qubit is a valid way to align on the qubit. The internal quality factor Q_i of the aligned resonator returns to its zero field value after ramping up and down the field, indicating that almost no magnetic flux vortices were formed. Also, the alignment is dependent on the position of the resonator on the chip. This is due to inhomogeneity of the perpendicular magnetic field. A solution is to use a bigger perpendicular coil diameter. The alignment shows hysteresis while ramping the field. This means that we can not assume a perfect relation $B_{x,align} \propto B_{\parallel}$ for aligning and need to align during and after ramping.
One of the measured qubits has a $T_2^e \sim 0.5\,\mu\mathrm{s}$ at 250 mT. The coherence times T_1, T_2^2 and T_2^s are influenced heavily by the magnetic field, with an interesting pattern of increases and decreases in these times at 50 and 100 mT and a peak at 200 mT. The rampdown has a very different relation, losing coherence as the field ramps down to zero field.
Next to ramping the magnetic field magnitude at a constant angle in-plane, the nanowire transmon has been investigated at a fixed magnetic field magnitude, but at a changing in-plane angle of the magnetic field. Knowing the virtual in-plane vectors $V1$ and $V2$, the alignment procedure produces the best aligning perpendicular field correctly for the whole angle sweep. The in-plane angle between the nanowire and the in-plane magnetic field is crucial to measurements, since the qubit frequency is maximum when the nanowire is parallel to the applied in-plane magnetic field and minimal when perpendicular. This can be explained by the proximitized nanowire superconducting gap that has a higher critical magnetic field parallel to the magnetic field. The qubit frequency also shows an asymmetry between θ and $\theta+\pi$. This might be due to an asymmetry

between the two perpendicular sides of the nanowire, such as the 2-facet shell facing only one side, while the other side is bare InAs nanowire.
The origin of $1/f$-flux noise is investigated and several important characteristics of its origin have been discussed. Consensus is that the flux noise originates from local spin fluctuators near or on the SQUID loop. Promising candidate spins include hydrogen and oxygen, and proposed spin fluctuation processes include the RKKY-interaction and hyperfine splitting. Several methods are given that would apply for a transmon qubit to the characterize flux noise at several frequency ranges.
Spatially uncorrelated spin fluctuators in a magnetic field has and their coupling to the flux noise have been investigated and simulated. The power spectral density (PSD) of the flux mirrors the PSD components of the spin fluctuator. This means that not only the component parallel to the field is important, but also the components perpendicular. An analytical equation for the PSD of the spin fluctuator parallel to the magnetic field (zz-component) was derived. Simulations have verified this equation. An approximate equation for the PSD of the spin fluctuator perpendicular to the magnetic field (xx-component) has been found. This component exhibits different effects at positive and negative frequencies of the PSD, corresponding to quantum noise due to Larmor precession. Other cross-spectral densities are deemed to be unimportant to the problem due to symmetries or its negligible values.
An ensemble of fluctuators has been investigated. This ensemble gives us the $1/f$-noise as expected. Using approximations, the coupling of the spins to our SQUID have been found and captured in geometry and spin species independent constants. An example of a spin-1/2 particle using our SQUID dimensions and literature values has been worked out and the flux noise PSD has been simulated and approximated. It shows that the magnetic field suppresses the zz-contribution of the spin PSD by $\sim \cosh^{-2}(\mu_B B/k_B T)$. The field also changes the Larmor precession frequency $f_Z \sim B$, determining the frequency at which the peak in the xx-contribution appears. Next to that, the xx-contribution is insensitive at frequencies higher than $2f_Z$. At frequencies higher than $2f_Z$, the xx-contribution is the dominant factor. The simulations also show that the angle the magnetic field makes with the SQUID influences the flux noise amplitude by a factor of about 1.5. This can be increased by increasing the rotational asymmetry of the SQUID loop.
A flux tunable nanowire transmon was investigated in a magnetic field. It has proved difficult to find the qubit frequency, since the resonator frequency does not correspond perfectly to the qubit frequency. This is due to the bare resonator frequency shifting. A solution is to use the power shift to determine the qubit frequency through a modified dispersive shift relation. The magnet introduces significant noise in Ramsey experiments for all qubits at field, and for flux tunable qubits there is an additional noise component quadratically proportional to the misalignment angle. We have found that a qubit can be flux tunable at 245 mT.
Flux sweeps were made using the perpendicular coil as flux bias at several fields and angles. It has been found that we could not calibrate the flux bias to multiples of Φ_0. This is due to vortex forming near the SQUID loop. Therefore, the sensitivity necessary for the measurement of flux noise cannot be extracted. Dedicated flux bias lines have been (re)introduced and these do not introduce flux jumps. A flux noise amplitude of $\sqrt{A} \sim 1000\,\mu\Phi_0$ was measured.
Finally, a new magnet current source system has been installed and troubleshot. This system can rotate a full 360° and can go to 500 mT, the maximum field the system can provide. This system had several unexpected issues, which were diagnosed, solved and documented. The used design parameters of the chip were documented and an improved method to fit the double beating patterns in the Double Ramsey experiments was implemented.

7.1. Future research

The first step would be to increase the yield of flux tunable qubits. The statistical analysis of the nanowire resistances can be used as a room temperature measure of the yield. Since we have found the fabrication cycle to impact the resistance, changing fabrication parameters and seeings its effect on the nanowire resistances might give a way to increase the yield. An explanation also needs to be found to explain the log-uniform distribution of the nanowire resistances. Another way to increase the yield, is to change the bias line setup to include six flux bias lines, since qubits without them will not be usable for measuring the flux noise.
Another change to the chip design, would be to extend the resonator holes to the very edge of the coplanar wave guides, since the current density of thin-film superconductors is highest at the edges. A vortex on the edge will create the dominant loss channel for the resonator.
With more usable qubits, improving the collective alignment is the next issue. A good way to go forwards is to increase the coil diameter of the perpendicular field coil to remove inhomogeneities and to automate the

field alignment procedures, so that we are not time-limited by human efforts and errors.
Areas to investigate for (non-flux tunable) qubits are the coherence for fields up to 0.5 mT and its relation to angles for the full 360° in-plane field. These will give more insight in potential undesirable nanowire effects on the qubit frequency and the application of the BCS gap critical magnetic field approximation at high fields.
Now turning to the flux noise measurements in a magnetic field, our simulations can be extended to include models using $S \neq 1/2$ or the hyperfine splitting with the hydrogen atom. Another avenue is the full simulation of spin coupled to a spin bath, retrieving the relaxation rates or excitation rates of the spin-spin interaction system in question (for which contenders are RKKY-interaction or hyperfine splitting interaction). In the simulation, it would be good to also include other non-rotationally symmetric SQUID washers, such as triangle washers or rectangular washers. These are shown to create a difference between the flux noise amplitudes as a function of the angle of the magnetic field. This can be used to separate the contribution of the perpendicular spin fluctuation component and the parallel spin fluctuation component.
For the flux tunable nanowire transmon, the qubit frequency can be found more easily by making a power shift map to the qubit frequency, and automating this process. This will prevent losing the qubit frequency and might be used as a robust backup routine if the main strategy of finding the qubit fails. A next improvement would be to implement a system where a full flux quantum flux sweep can be performed automatically, with the perpendicular coil and dedicated flux bias line working in tandem.
After these things have been completed, the qubit echo times vs. flux at different fields, different field angles and fridge temperatures need to be mesaured to extract the flux noise amplitude. Moreover, techniques to extract GHz-noise levels should be implemented to investigate the noise at the frequencies on and around the potential peaks of the hydrogen hyperfine splitting peak or any electron spin Larmor precession peak.

Acknowledgements

First off, I would like to thank Leo DiCarlo for giving me the opportunity to conclude my student life at one of the coolest projects I have worked on to date. There is so much cool stuff happening in this lab simultaneously, every week had something to show for. I could definitely watch a live stream of it.
Speaking of the lab, I would like to thank every one of you for being open to answer any question I had. I have been lucky to be surrounded by all these clever people and I definitely learned a lot of good practices in research right here, during data meetings or journal clubs. I enjoyed the evening discussions where Ramiro Sagastizabal shared his current project with me thorougly and without prompt. I'd like to thank Niels Bultink for helping me out when I had a problem with measuring and his occasional spot-on pun. I'd like to thank Adriaan Rol for having some good philosophical questions (and by definition of philosophy, answering it with more questions). It made the not-knowing of the answers in the research a lot more enjoyable. You also made me realize some important distinctions in the presentation of data and taught me the general gist of good gitting. I'd like to thank Luc Janssen and Timo van Abswoude for being other students to whom I could vent my amateur measuring misadventures with. I would like to thank Matt Sarsby for sharing fun fridge anecdotes to boot and sharing his enthusiasm about the fridges in general. I would like to thank Gerco Versloot for always having a good joke at hand and Jacob de Sterke for making more of those jokes. I'd like to thank Nandini Muthusubramanian for sharing her design for PyQip3 and Marc Beekman for helping me through understanding PyQip3.
I'd like to thank Slava Dobrovitski, Anton Akhmerov and Akira Endo for accepting the invitation to join my assessment committee. I hope you will enjoy this decision as well.
I'd like to thank Bas Dorsman for the necessary coffee breaks and his enthusiastically listening to my stories about fridges and qubits and Rebecca Gharibaan to acknowledge the lack of mathematical rigor in physics at moments I needed it most.
I'd like to thank Florian Lüthi, for being really welcoming into the nanowire transmon group and for sharing his years of experience. Thank you for enduring the indefinite amount of silly questions I kept asking about the nanowires, disentangling all the intertwined concepts. Your thesis also proved very resourceful, which definitely got answers to questions I did not yet know.
And last, but definitely not least, I'd like to thank Thijs Stavenga for enduring my endless barrage of topics of utmost non-importance. Thank you for taking the time to teach me the concepts of measuring, opening and closing the fridge, the concepts of fabrication. And thanks for keeping on making chips for me to measure, it always was a time of excitement during the first week of measuring. You have been a great motivator to just do it, instead of correcting for every failure case.

In the end, one major wisdom that I will take with me for the rest of my career will be: "What would Leo say?", which can often steer you in the right direction.

Bibliography

[1] Vinay Ambegaokar and Alexis Baratoff. Tunneling between superconductors. *Phys. Rev. Lett.*, 10: 486–489, Jun 1963. doi: 10.1103/PhysRevLett.10.486. URL https://link.aps.org/doi/10.1103/PhysRevLett.10.486.

[2] Joep Assendelft. Increasing the magnetic field compatibility and field stability of nanowire transmons. Master's thesis, Delft University of Technology, 2018.

[3] Rami Barends. *Photon-detecting superconducting resonators.* PhD thesis, Delft University of Technology, 2009.

[4] Marc Beekman. Superconducting transmon qubit chip design and characterization through electromagnetic analysis. Master's thesis, Delft University of Technology, 2018.

[5] Bernd A. Berg and Robert C. Harris. From data to probability densities without histograms. *Computer Physics Communications*, 179(6):443 – 448, 2008. ISSN 0010-4655. doi: https://doi.org/10.1016/j.cpc.2008.03.010. URL http://www.sciencedirect.com/science/article/pii/S0010465508001458.

[6] Radoslaw C Bialczak, R McDermott, M Ansmann, M Hofheinz, N Katz, Erik Lucero, Matthew Neeley, AD O'Connell, H Wang, AN Cleland, et al. 1/f flux noise in josephson phase qubits. *Physical review letters*, 99(18):187006, 2007.

[7] Hendrik Bluhm, Julie A. Bert, Nicholas C. Koshnick, Martin E. Huber, and Kathryn A. Moler. Spinlike susceptibility of metallic and insulating thin films at low temperature. *Phys. Rev. Lett.*, 103:026805, Jul 2009. doi: 10.1103/PhysRevLett.103.026805. URL https://link.aps.org/doi/10.1103/PhysRevLett.103.026805.

[8] X. Bonet-Monroig, R. Sagastizabal, M. Singh, and T. E. O'Brien. Low-cost error mitigation by symmetry verification. *Phys. Rev. A*, 98:062339, Dec 2018. doi: 10.1103/PhysRevA.98.062339. URL https://link.aps.org/doi/10.1103/PhysRevA.98.062339.

[9] Daniel Bothner, Tobias Gaber, Matthias Kemmler, Dieter Koelle, Reinhold Kleiner, Stefan Wünsch, and Michael Siegel. Magnetic hysteresis effects in superconducting coplanar microwave resonators. *Physical Review B*, 86(1):014517, 2012.

[10] Jonas Bylander, Simon Gustavsson, Fei Yan, Fumiki Yoshihara, Khalil Harrabi, George Fitch, David G Cory, Yasunobu Nakamura, Jaw-Shen Tsai, and William D Oliver. Noise spectroscopy through dynamical decoupling with a superconducting flux qubit. *Nature Physics*, 7(7):565, 2011.

[11] SangKook Choi, Dung-Hai Lee, Steven G. Louie, and John Clarke. Localization of metal-induced gap states at the metal-insulator interface: Origin of flux noise in squids and superconducting qubits. *Phys. Rev. Lett.*, 103:197001, Nov 2009. doi: 10.1103/PhysRevLett.103.197001. URL https://link.aps.org/doi/10.1103/PhysRevLett.103.197001.

[12] S. E. de Graaf, A. A. Adamyan, T. Lindström, D. Erts, S. E. Kubatkin, A. Ya. Tzalenchuk, and A. V. Danilov. Direct identification of dilute surface spins on al_2o_3: Origin of flux noise in quantum circuits. *Phys. Rev. Lett.*, 118:057703, Jan 2017. doi: 10.1103/PhysRevLett.118.057703. URL https://link.aps.org/doi/10.1103/PhysRevLett.118.057703.

[13] Rogerio de Sousa. Dangling-bond spin relaxation and magnetic $1/f$ noise from the amorphous-semiconductor/oxide interface: Theory. *Phys. Rev. B*, 76:245306, Dec 2007. doi: 10.1103/PhysRevB.76.245306. URL https://link.aps.org/doi/10.1103/PhysRevB.76.245306.

[14] Chow J. M. Gambetta J. M. Bishop Lev S. Johnson B. R. Schuster D. I. Majer J. Blais A. Frunzio L. Girvin S. M. DiCarlo, L. and R. J. Schoelkopf. Demonstration of two-qubit algorithms with a superconducting quantum processor. *Nature*, 460:240 EP –, Jun 2009. URL https://doi.org/10.1038/nature08121.

[15] E.M. Wilson E.H. Rhoderick. Current distribution in thin superconducting films. *Nature*, 194(4834): 1167–1168, 1962. ISSN 1476-4687. doi: 10.1038/1941167b0. URL https://doi.org/10.1038/1941167b0.

[16] O. Enzing. Nanowire transmon characterisation and design ofa protected qubit. Master's thesis, Delft University of Technology, 2017.

[17] Lara Faoro and Lev B. Ioffe. Microscopic origin of low-frequency flux noise in josephson circuits. *Phys. Rev. Lett.*, 100:227005, Jun 2008. doi: 10.1103/PhysRevLett.100.227005. URL https://link.aps.org/doi/10.1103/PhysRevLett.100.227005.

[18] Lara Faoro and Lorenza Viola. Dynamical suppression of $1/f$ noise processes in qubit systems. *Phys. Rev. Lett.*, 92:117905, Mar 2004. doi: 10.1103/PhysRevLett.92.117905. URL https://link.aps.org/doi/10.1103/PhysRevLett.92.117905.

[19] Alexandra C Ford, S Bala Kumar, Rehan Kapadia, Jing Guo, and Ali Javey. Observation of degenerate one-dimensional sub-bands in cylindrical inas nanowires. *Nano letters*, 12(3):1340–1343, 2012.

[20] W.H. Henkels and C.J. Kircher. Penetration depth measurements on type ii superconducting films. *Magnetics, IEEE Transactions on*, 13:63 – 66, 02 1977. doi: 10.1109/TMAG.1977.1059426.

[21] J.R. Johansson, P.D. Nation, and Franco Nori. Qutip: An open-source python framework for the dynamics of open quantum systems. *Computer Physics Communications*, 183(8):1760 – 1772, 2012. ISSN 0010-4655. doi: https://doi.org/10.1016/j.cpc.2012.02.021. URL http://www.sciencedirect.com/science/article/pii/S0010465512000835.

[22] J.R. Johansson, P.D. Nation, and Franco Nori. Qutip 2: A python framework for the dynamics of open quantum systems. *Computer Physics Communications*, 184(4):1234 – 1240, 2013. ISSN 0010-4655. doi: https://doi.org/10.1016/j.cpc.2012.11.019. URL http://www.sciencedirect.com/science/article/pii/S0010465512003955.

[23] K. Kakuyanagi, T. Meno, S. Saito, H. Nakano, K. Semba, H. Takayanagi, F. Deppe, and A. Shnirman. Dephasing of a superconducting flux qubit. *Phys. Rev. Lett.*, 98:047004, Jan 2007. doi: 10.1103/PhysRevLett.98.047004. URL https://link.aps.org/doi/10.1103/PhysRevLett.98.047004.

[24] Jens Koch, M Yu Terri, Jay Gambetta, Andrew A Houck, DI Schuster, J Majer, Alexandre Blais, Michel H Devoret, Steven M Girvin, and Robert J Schoelkopf. Charge-insensitive qubit design derived from the cooper pair box. *Physical Review A*, 76(4):042319, 2007.

[25] Roger H. Koch, John Clarke, W. M. Goubau, J. M. Martinis, C. M. Pegrum, and D. J. van Harlingen. Flicker (1/f) noise in tunnel junction dc squids. *Journal of Low Temperature Physics*, 51(1):207–224, Apr 1983. ISSN 1573-7357. doi: 10.1007/BF00683423. URL https://doi.org/10.1007/BF00683423.

[26] Roger H. Koch, David P. DiVincenzo, and John Clarke. Model for $1/f$ flux noise in squids and qubits. *Phys. Rev. Lett.*, 98:267003, Jun 2007. doi: 10.1103/PhysRevLett.98.267003. URL https://link.aps.org/doi/10.1103/PhysRevLett.98.267003.

[27] P Kumar, S Sendelbach, MA Beck, JW Freeland, Zhe Wang, Hui Wang, C Yu Clare, RQ Wu, DP Pappas, and R McDermott. Origin and reduction of 1/f magnetic flux noise in superconducting devices. *Physical Review Applied*, 6(4):041001, 2016.

[28] S. LaForest and Rogério de Sousa. Flux-vector model of spin noise in superconducting circuits: Electron versus nuclear spins and role of phase transition. *Phys. Rev. B*, 92:054502, Aug 2015. doi: 10.1103/PhysRevB.92.054502. URL https://link.aps.org/doi/10.1103/PhysRevB.92.054502.

[29] T. Lanting, A. J. Berkley, B. Bumble, P. Bunyk, A. Fung, J. Johansson, A. Kaul, A. Kleinsasser, E. Ladizinsky, F. Maibaum, R. Harris, M. W. Johnson, E. Tolkacheva, and M. H. S. Amin. Geometrical dependence of the low-frequency noise in superconducting flux qubits. *Phys. Rev. B*, 79:060509, Feb 2009. doi: 10.1103/PhysRevB.79.060509. URL https://link.aps.org/doi/10.1103/PhysRevB.79.060509.

[30] T. Lanting, M. H. Amin, A. J. Berkley, C. Rich, S.-F. Chen, S. LaForest, and Rogério de Sousa. Evidence for temperature-dependent spin diffusion as a mechanism of intrinsic flux noise in squids. *Phys. Rev. B*, 89:014503, Jan 2014. doi: 10.1103/PhysRevB.89.014503. URL https://link.aps.org/doi/10.1103/PhysRevB.89.014503.

[31] Donghwa Lee, Jonathan L. DuBois, and Vincenzo Lordi. Identification of the local sources of paramagnetic noise in superconducting qubit devices fabricated on $\alpha-al_2o_3$ substrates using density-functional calculations. *Phys. Rev. Lett.*, 112:017001, Jan 2014. doi: 10.1103/PhysRevLett.112.017001. URL https://link.aps.org/doi/10.1103/PhysRevLett.112.017001.

[32] Florian Lüthi. *Circuit Quantum Electrodynamics in a Magnetic Field*. PhD thesis, Delft University of Technology, 2019.

[33] Florian Luthi, Thijs Stavenga, OW Enzing, Alessandro Bruno, Christian Dickel, NK Langford, Michiel Adriaan Rol, Thomas Sand Jespersen, Jesper Nygård, P Krogstrup, et al. Evolution of nanowire transmon qubits and their coherence in a magnetic field. *Physical review letters*, 120(10):100502, 2018.

[34] John M. Martinis, S. Nam, J. Aumentado, K. M. Lang, and C. Urbina. Decoherence of a superconducting qubit due to bias noise. *Phys. Rev. B*, 67:094510, Mar 2003. doi: 10.1103/PhysRevB.67.094510. URL https://link.aps.org/doi/10.1103/PhysRevB.67.094510.

[35] Benjamin J Mazin. *Microwave Kinetic Inductance Detectors*. PhD thesis, California Institute of Technology, 2004.

[36] M.A. Nielsen and I.L. Chuang. *Quantum Computation and Quantum Information: 10th Anniversary Edition*. Cambridge University Press, 2010. ISBN 9781139495486.

[37] C. M. Quintana and Yu et al. Chen. Observation of classical-quantum crossover of $1/f$ flux noise and its paramagnetic temperature dependence. *Phys. Rev. Lett.*, 118:057702, Jan 2017. doi: 10.1103/PhysRevLett.118.057702. URL https://link.aps.org/doi/10.1103/PhysRevLett.118.057702.

[38] A. G. Redfield. On the theory of relaxation processes. *IBM Journal of Research and Development*, 1(1): 19–31, Jan 1957. ISSN 0018-8646. doi: 10.1147/rd.11.0019.

[39] S Sendelbach, D Hover, A Kittel, M Mück, John M Martinis, and R McDermott. Magnetism in squids at millikelvin temperatures. *Physical review letters*, 100(22):227006, 2008.

[40] Alexander Shnirman, Gerd Schön, Ivar Martin, and Yuriy Makhlin. Low- and high-frequency noise from coherent two-level systems. *Phys. Rev. Lett.*, 94:127002, Apr 2005. doi: 10.1103/PhysRevLett.94.127002. URL https://link.aps.org/doi/10.1103/PhysRevLett.94.127002.

[41] D. H. Slichter, R. Vijay, S. J. Weber, S. Boutin, M. Boissonneault, J. M. Gambetta, A. Blais, and I. Siddiqi. Measurement-induced qubit state mixing in circuit qed from up-converted dephasing noise. *Phys. Rev. Lett.*, 109:153601, Oct 2012. doi: 10.1103/PhysRevLett.109.153601. URL https://link.aps.org/doi/10.1103/PhysRevLett.109.153601.

[42] Thijs Stavenga. Transmon qubits with a nanowire josephson junction. Master's thesis, Delft University of Technology, 2016.

[43] D. J. Thoen, B. G. C. Bos, E. A. F. Haalebos, T. M. Klapwijk, J. J. A. Baselmans, and A. Endo. Superconducting nbtin thin films with highly uniform properties over a ∅ 100 mm wafer. *IEEE Transactions on Applied Superconductivity*, 27(4):1–5, June 2017. ISSN 1051-8223. doi: 10.1109/TASC.2016.2631948.

[44] M. Tinkham. *Introduction to Superconductivity: Second Edition*. Dover Books on Physics. Dover Publications, 2004. ISBN 9780486435039. URL https://books.google.nl/books?id=k6AO9nRYbioC.

[45] D. J. Van Harlingen, Roger H. Koch, and John Clarke. Superconducting quantum interference device with very low magnetic flux noise energy. *Applied Physics Letters*, 41(2):197–199, 1982. doi: 10.1063/1.93460. URL https://doi.org/10.1063/1.93460.

[46] Hui Wang, Chuntai Shi, Jun Hu, Sungho Han, Clare C. Yu, and R. Q. Wu. Candidate source of flux noise in squids: Adsorbed oxygen molecules. *Phys. Rev. Lett.*, 115:077002, Aug 2015. doi: 10.1103/PhysRevLett.115.077002. URL https://link.aps.org/doi/10.1103/PhysRevLett.115.077002.

[47] Zhe Wang, Hui Wang, Clare C. Yu, and R. Q. Wu. Hydrogen as a source of flux noise in squids. *Phys. Rev. B*, 98:020403, Jul 2018. doi: 10.1103/PhysRevB.98.020403. URL https://link.aps.org/doi/10.1103/PhysRevB.98.020403.

[48] R. K. Wangsness and F. Bloch. The dynamical theory of nuclear induction. *Phys. Rev.*, 89:728–739, Feb 1953. doi: 10.1103/PhysRev.89.728. URL https://link.aps.org/doi/10.1103/PhysRev.89.728.

[49] F. C. Wellstood, C. Urbina, and J. Clarke. Role of geometry on the color of flux noise in dc squids. *IEEE Transactions on Applied Superconductivity*, 21(3):856–859, June 2011. ISSN 1051-8223. doi: 10.1109/TASC.2010.2093092.

[50] Frederick C. Wellstood, Cristian Urbina, and John Clarke. Low-frequency noise in dc superconducting quantum interference devices below 1 k. *Applied Physics Letters*, 50(12):772–774, 1987. doi: 10.1063/1.98041. URL https://doi.org/10.1063/1.98041.

[51] Jiansheng Wu and Clare C. Yu. Modeling flux noise in squids due to hyperfine interactions. *Phys. Rev. Lett.*, 108:247001, Jun 2012. doi: 10.1103/PhysRevLett.108.247001. URL https://link.aps.org/doi/10.1103/PhysRevLett.108.247001.

[52] Fei Yan, Jonas Bylander, Simon Gustavsson, Fumiki Yoshihara, Khalil Harrabi, David G. Cory, Terry P. Orlando, Yasunobu Nakamura, Jaw-Shen Tsai, and William D. Oliver. Spectroscopy of low-frequency noise and its temperature dependence in a superconducting qubit. *Phys. Rev. B*, 85:174521, May 2012. doi: 10.1103/PhysRevB.85.174521. URL https://link.aps.org/doi/10.1103/PhysRevB.85.174521.

[53] Fei Yan, Simon Gustavsson, Jonas Bylander, Xiaoyue Jin, Fumiki Yoshihara, David G Cory, Yasunobu Nakamura, Terry P Orlando, and William D Oliver. Rotating-frame relaxation as a noise spectrum analyzer of a superconducting qubit undergoing driven evolution. *Nature communications*, 4:2337, 08 2013. doi: 10.1038/ncomms3337.

[54] F. Yoshihara, K. Harrabi, A. O. Niskanen, Y. Nakamura, and J. S. Tsai. Decoherence of flux qubits due to $1/f$ flux noise. *Phys. Rev. Lett.*, 97:167001, Oct 2006. doi: 10.1103/PhysRevLett.97.167001. URL https://link.aps.org/doi/10.1103/PhysRevLett.97.167001.

[55] F. Yoshihara, Y. Nakamura, and J. S. Tsai. Correlated flux noise and decoherence in two inductively coupled flux qubits. *Phys. Rev. B*, 81:132502, Apr 2010. doi: 10.1103/PhysRevB.81.132502. URL https://link.aps.org/doi/10.1103/PhysRevB.81.132502.

[56] Fumiki Yoshihara, Yasunobu Nakamura, Fei Yan, Simon Gustavsson, Jonas Bylander, William D. Oliver, and Jaw-Shen Tsai. Flux qubit noise spectroscopy using rabi oscillations under strong driving conditions. *Phys. Rev. B*, 89:020503, Jan 2014. doi: 10.1103/PhysRevB.89.020503. URL https://link.aps.org/doi/10.1103/PhysRevB.89.020503.

[57] T. Zieliński and K. Duda. "frequency and damping estimation methods - an overview". *"Metrology and Measurement Systems"*, "18"("4"):"505 – 528", "2011". URL "https://content.sciendo.com/view/journals/mms/18/4/article-p505.xml".

[58] David Zueco, Georg M Reuther, Sigmund Kohler, and Peter Hänggi. Qubit-oscillator dynamics in the dispersive regime: Analytical theory beyond the rotating-wave approximation. *Physical Review A*, 80(3):033846, 2009.

A

Nanowire transmon physics

A.1. Nanowire subband Hamiltonian

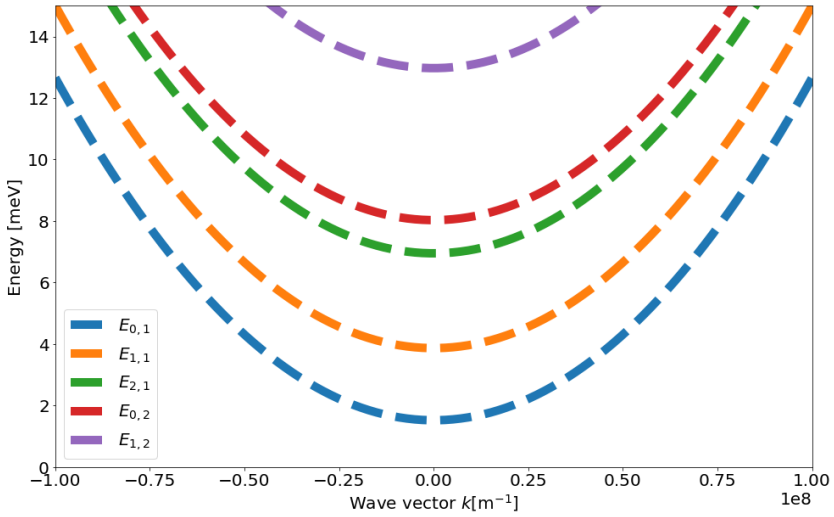

Figure A.1: The energy levels $E_{\lambda,\mu}$ in a cylindrical nanowire for different values of the wave number k. Using $m_{eff} = 0.034$ and $R = 65$ nm. We can clearly see that the gaps are of the order 5 meV.

To gain intuition in the basic 1D subband structure on which the use of nanowires is based, we will work through a simplified model.
Assuming an electron-like particle in a perfect cylindrical and infinitely long nanowire, we can model it using the Hamiltonian in cylindrical coordinates (ρ, ϕ, z) as

$$H\psi = -\frac{\hbar^2}{2m}\nabla^2\psi + V(\mathbf{x})\psi = E\psi \tag{A.1}$$

where we assume a infinite quantum well where the wavefunction is 0 on the nanowire-to-air/vacuum interface by assuming an infinite well potential

$$V(\mathbf{x}) = \begin{cases} 0 & \text{if } \rho < R \\ \infty & \text{if } \rho \geq R \end{cases}$$

here ρ is the perpendicular coordinate, R the radius of the nanowire and ϕ will be the angular coordinate of the wavefunction. Solving this system assuming a plane wave in the z-direction, we find eigenfunctions

$$\psi_{\lambda,\alpha}(\rho, t) = J_{|\lambda|}(\frac{\alpha_{\lambda,\mu}}{R}\rho)\exp\big(i\lambda\phi\big)e^{i(kz-\omega t)} \tag{A.2}$$

where $\lambda \in \mathbb{N}_{\geq 0}$ is a parameter indicating the amount of angular nodes and $\mu \in \mathbb{N}_{\geq 1}$ a parameter indicating the amount of radial nodes, $J_\nu(x)$ the Bessel function of the first kind, k the wave number and ω wave frequency of the electron-like particle. $\alpha_{\lambda,\mu}$ is the μ'th zero of the Bessel function $J_{|\lambda|}(x)$. The eigenenergies of this system can be found as

$$E = \frac{\hbar^2 k^2}{2m_{eff}} + \frac{\hbar^2}{2m_{eff}} \frac{\alpha_{\lambda,\mu}^2}{R^2} \tag{A.3}$$

where we can see that we can limit the amount of energies available by decreasing the radius R. We use experimental data found in [19] where they use an InAs nanowire of radius $R = 7.5\,\text{nm}$, to match Equation (A.3) using $m_{eff} = 0.034 m_e$. The energy levels are given in Figure A.1 are then given for a nanowire of radius 65 nm like used on our chip. This model contains some unrealistic assumptions, as the wavefunction will not be exactly zero at the nanowire-air/vacuum interface and the nanowires we use have a superconducting aluminum half-shell. Also, the nanowires used are hexagonal instead of perfectly cylindrical.

A.2. Possible measurements using a (nanowire) transmon

This gives a short summary of the relevant types of measurements in the experiment.[1]

1. Anharmonicity measurement. This can be done by probing a $f_{02}/2$ measurement.
2. Rabi experiment. Here, we measure the oscillation between the excited and ground state of the qubit by a microwave pulse as a function of the pulse shape.
3. T_1-experiment. Here, we excite a qubit, and measure the time it takes before it returns to the ground state.
4. Ramsey (T_2^*) experiment. We determine the decoherence and dephasing of the qubit along the equator of the Bloch sphere
5. Double beating Ramsey. If a double beating is present, a TLS flips the qubit frequency between two different frequencies.
6. Hahn echo experiment. We determine the decoherence and dephasing of the qubit like a Ramsey experiment, but we filter out the low noise by adding a refocusing pulse.
7. Power shift measurement, where we measure the resonator frequency at low power, so that we measure the dispersive shift, and at high power, which is the bare frequency.

[1] A more complete introduction to measurement with our setup can be found in this presentation: http://aqis-conf.org/2016/wp-content/uploads/2015/12/20160828langford_aqis_tutorial.pdf

B

Experimental setup

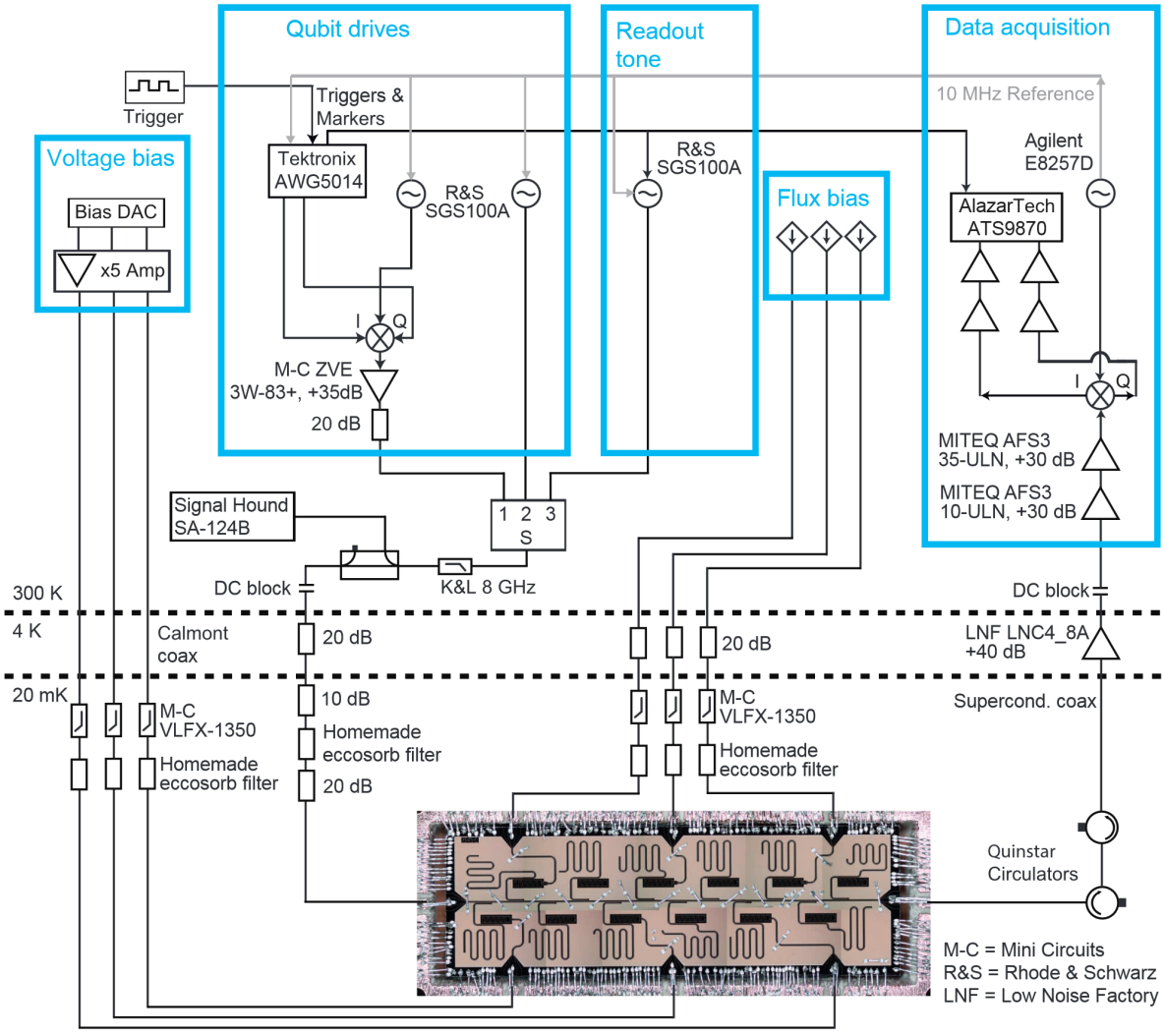

Figure B.1: The setup for measuring the qubit devices. Image from Florian Lüthi's PhD thesis [32].

Our setup, visible in Figure B.1, is build to create an environment at tens of mK with a controllable 3-axis magnetic field and microwave RF electronic connections. We use a Leiden Cryogenics CF-450 He_3/He_4-dilution refrigerator, which can deliver around $\sim 450\,\mu W$ of cooling power during operation. It has different temperature stages through which all wiring has to go, which contain attenuators or low temperature amplifiers. At

Table B.1: Properties of the Y and Z-axis magnets used. Data taken from datasheet.

	Y-axis	Z-axis
Inductance [H]	1.8	0.7
Coil constant [T/A]	0.0132	0.0496
Maximum current [A]	37.88	40.32
Maximum ramp rate [1] [A/s]	0.0543	0.677

the coldest stage, the Mixing Chamber (MC), it should be able to have a base temperature as low as 12 mK. However, in our experiments, a temperature of ≥ 22 mK has been measured. It can house different temperature or pressure sensors. The most unique quality of this particular fridge is its 3-axis magnet. These magnets can collectively deliver fields to the device in the MC. This allows a full characterization of magnetic effects on the superconductors or qubits on the device. To shield the chip from external magnetic fields, additional magnetic shields were added [2].
A typical measurement can be done using an Arbitrary Wave Generator (AWG) as an arbitrary pulse generator. The signal is mixed using IQ-mixing to upconvert the signal using a 10 MHz local oscillator, to protect the system to low-frequency noise. Between the mixer and the device is 45 dB attenuation (see Figure B.1). This should cause an average of one photon to arrive in the chip. After interacting with the chip, the output signal travels through circulators, preventing power to dissipate back into the chip. The signal is amplified in higher temperature stages by 100 dB through 3 sequential amplifiers. The resulting I and Q are digitized and sent to computer memory. Additionally, we can apply voltages biases and dedicated flux biases to certain chosen qubits. In total, 6 lines are available, where we have chosen 3 voltage bias lines and 3 flux bias lines (supplying current) as are visible in Figure B.2 as $V1-V3$ and $F1-F3$ respectively.

B.1. Magnets and magnet current sources

For a 3-axis magnet, 3 dedicated magnets are necessary, each supplying a field in an orthogonal direction. Any misalignments can be solved using the other magnets to correct for this. This is used later, since the devices will also not be perfectly aligned to the fields as expected.
The magnet perpendicular to the plane of the chip, from hereon dubbed the 'perpendicular coil', is a thin-wire coil resting immediately next to the chip holder. It has a wire diameter of ~ 0.1 millimeter, and is supplied by small currents (maximum 40 mA), providing small fields below 8 mT. This is by design, since thin-film superconductors create vortices at a perpendicular field, see Section C.2.1.
The Y and Z-axis magnets (supplying fields in-plane of the device), are encapsulated in a magnetic shield and surround the device. The Z-axis surrounds the chip and the Y-field is delivered by 2 coils on either side of the device. They simultaneously can deliver a field of 500 mT.
The Y and Z-axis magnets have a persistent current mode, in which they are disconnected from source current noise due to an internal superconducting loop. This loop contains a persistent switch. This is a device that, when heated, turns normalconducting and creates a resistance in the superconducting loop. This dissipates current and creates a link with any current source connected.
The relevant properties of the magnets used are listed in Table B.1. These values are e.g. used in Section 5.2 to calculate the participation of the current source noise on our measurements.
An effect of having the magnets in the MC, is the possibility of heat transfer through radiation and conduction into the MC. During rampup of the field, we noticed a significant increase in temperature. We use at least two magnets during ramping, to align the field. We have found the perpendicular coil as the main contributor for this heat load on the MC.

B.2. Magnet current source upgrade

The old current source was a Kepco current source. This current source did not have positive and negative current polarity, and was not software programmable. To resolve this, we installed two 4Q06125PS-430 power supply units, one for both the Y and Z-axis. This power supply works as follows: the current source supplies a current to the magnet through the leads. This current is controlled by the voltage that the AMI430 programmer outputs. The AMI430 programmer is the interface that connects through Ethernet with the computer and is programmable. It has connections for the persistent switch heaters and the voltage probes (hint: keep the voltage probes an open, do not connect them in any way, shape or form to the fridge). A short sum-

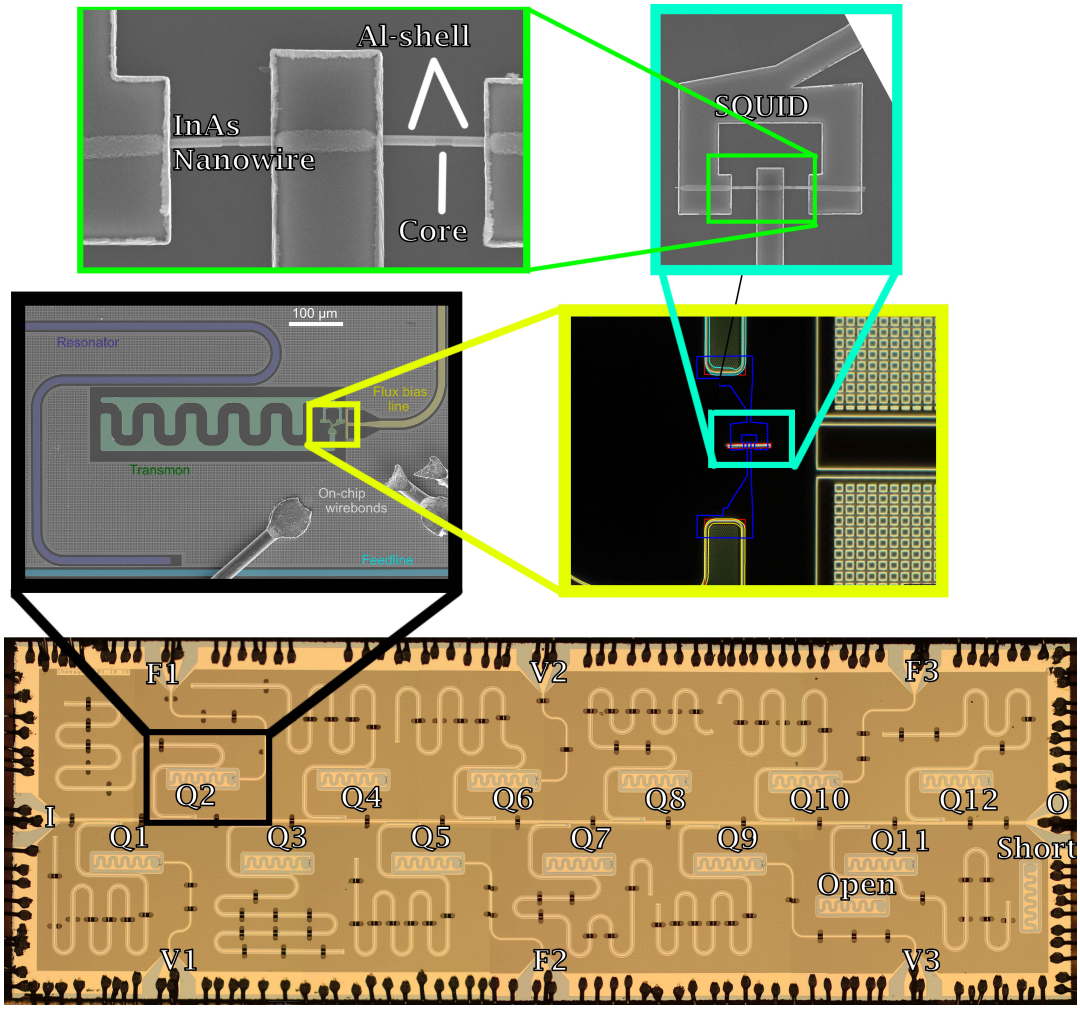

Figure B.2: A collection of greater magnitude zooms of the chip. The high level overview shows the chip with resonators, qubits Q1-Q12, the test qubits Qopen and Qshort, and labels for all electronic connections outside the chip. The second zoom level shows the transmon structure and its connection to the resonator and flux bias line, from [32]. The third zoom shows the contacts that will be etched on the junction area for a flux tunable qubit around the nanowire, the fourth zoom shows a Scanning Electron Microscope (SEM) picture of the SQUID loop that was made. This is used to tune the qubit frequency by applying a flux through the loop. The last zoom level depicts the InAs nanowire with the superconducting aluminium 2-facet shell, where a part of the shell is etched to create a Josephson junction.

mary of peculiarities can be found in Appendix J. A module has been written to interface this system with the Magnet class, a module written in Python which controls the fields and prevents sudden and unwanted changes in the field. It is also used to align the magnet to any misalignment as will be discussed in Section 2.4.

B.3. Qubit device

A zoom of a collection of chips is shown in Figure B.2. There are eight electronic connections to the chips. The feedline, represented as I and O for input and output, is the electronic wire through which all microwave pulses, gate control and readout is fed. The connectors labeled $V1/V2/V3$ are the voltage bias lines, providing a voltage side gate bias to the nanowire qubits, tuning the qubit frequency. The connectors, labeled $F1/F2/F3$ are the flux bias lines. On qubits with a SQUID loop, this tunes the qubit frequency through flux tunability as described in Section 1.5. The qubits can be found in the yellow inset , where the big curved pads create a capacitance, and the rightmost structure a SQUID loop containing a nanowire creating two weak-link Josephson junctions. The blue zoom shows the SQUID loop and the two nanowire junctions. The chip also contains two transmon structures, without nanowires. Q_{short} has instead of a nanowire junction, a small strip connected between the two pads. Q_{open} does not have a nanowire junction at all. The reason for this is elucidated in Section 6. Any perpendicular magnetic field creates vortices in the CPWs, changing the

resonator frequencies and losses. We create holes in the resonator, to prevent these from forming, due to unwanted misalignment and field inhomogeneities. The chips previously had on-chip wirebonds, connecting the grounds across the feedline and the coplanar waveguides. They had been superseded by airbridges, but we have returned to using on-chip wirebonds.

C

Chip design

The design of the chip needs to adhere to design constraints. In this thesis, we are going to focus on the resonator targeting, the effect of the holes to prevent Abrikosov vortices and the coupling quality targeting.

C.1. Shape of the resonator transmission

The readout resonator, through which we can couple with the resonator, can be characterized by the S_{21}-transmission. This is the transmission from the input port to the output port of the feedline. The resonator is sensitive to a certain frequency. At this frequency, the transmission goes to zero since all signal goes into the resonator. We can model this using [3]

$$S_{21} = \frac{S_{21,min} + iy}{1 + iy} \tag{C.1}$$

where $S_{21,min}$ is the minimum of the resonator and $y = 2Q_l \frac{\delta\omega_0}{\omega_0} = 2Q_l \frac{(\omega-\omega_0)}{\omega_0}$ the relative frequency deviation from the actual resonator frequency. Q_l is the total quality factor of the resonator and can be divided into an internal and external coupling quality component through $Q_l^{-1} = Q_i^{-1} + Q_c^{-1}$. The minimum transmission $S_{21,min}$ is

$$S_{21,min} = \frac{Q_c}{Q_i + Q_c}. \tag{C.2}$$

Ideally, we have a perfect dip $S_{21,min} \approx 0$. As such, we need $Q_c \ll Q_i$. Assuming the minimum to be $S_{21,min} = 0$, we find the absolute value of S_{21} in the form

$$|S_{21}| = \frac{y}{\sqrt{1+y^2}} \tag{C.3}$$

which means that the full width at half minimum (FWHM) of the dip can be described by $|S_{21}| = \frac{1}{2}$, for which we find the solution

$$FWHM = 2\delta\omega_0 \left(|S_{21}| = \frac{1}{2} \right) = 2\omega_0 \frac{1}{2\sqrt{3}Q_l} \approx \frac{\omega_0}{1.7Q_c} \tag{C.4}$$

It is favorable to increase the Q_c to obtain a thinner dip, means we can more easily measure a shift in the resonator frequency due to the dispersive shift, since the S_{21} changes more rapidly as ω_0 shifts. However, we still need to satisfy the requirement $Q_i \gg Q_c$. We can find a formula to estimate Q_c from the dimensions and properties of the resonator and feedline fabrication, as will be seen in Section C.3.
The internal quality factor is determined by material quality and the fabrication process. This is sufficiently high ($10^5 - 10^6$) and we will assume intrinsic losses to be negligible.

C.1.1. Measuring the coupling quality factor

Where does this coupling quality factor come from? The resonator is, in fact, not floating in air, but it is coupled to a feedline. This coupling is capacitative and we find that it shifts the resonator frequency a few percent as [35],[3]

$$\omega_{loaded} = \omega_{unloaded} \left(1 - \frac{2Z_0}{\pi Z_{0,feed} Q_c} \right) \tag{C.5}$$

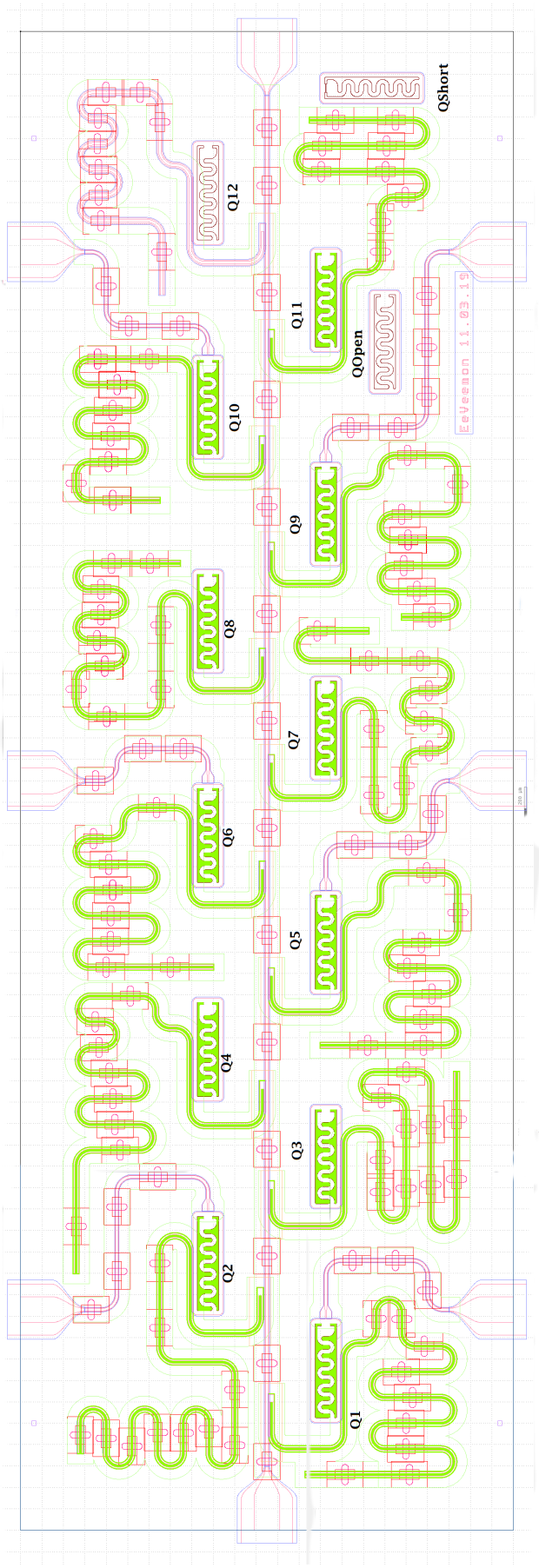

Figure C.1: Chip design made in January/February of 2019 to incorporate the nanowire transmons in pyQip 3. Annotated is the used convention of numbering resonators and qubits. The green colours indicate the holes in the coplanar waveguides (CPWs) serving as resonators. Only resonator 12 (only given as pink lines in the top right) does not have holes. In red, you can see the airbridges, creating a connection of the ground planes over the CPWs.

where ω_{loaded} is the same as the resonator frequency $\omega_{r,unload}$ used in the dispersive shift equation (1.4). [1] We have Z_0 the impedance of the resonator, $Z_{0,feed}$ the impedance of the feedline and Q_c the capacitative coupling quality factor of the resonator with the feedline.

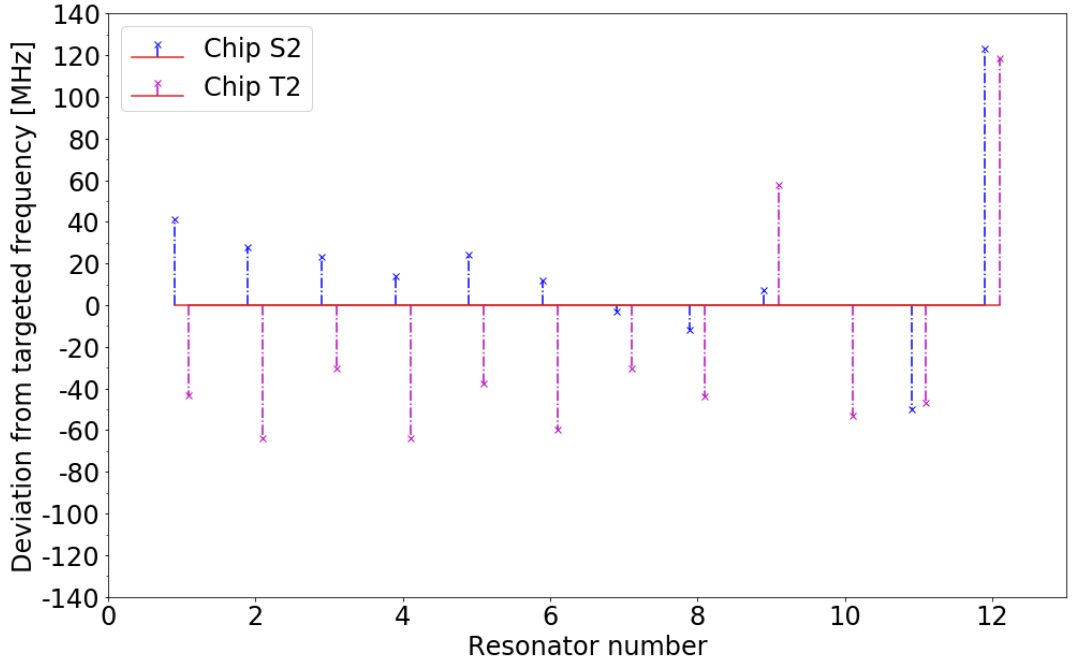

Figure C.2: The deviation of the resonator targeting ($f_{meas} - f_{pred}$) for all chips S2 and T2 for different resonators. The red line indicates no deviation. The blue crosses give the deviation in frequency for S2 and the magenta crosses the same, but for chip T2.

C.2. Chip design

We start by discussing the resonator targeting. This is important due to the readout only being sufficiently amplified between the $4-8$ GHz range. Also, the resonators need to be spaced in frequency so that there will be no overlap due to resonator mistargeting. A frequency spacing of 100 MHz is taken for every resonator $f_{res} < 6.2$ GHz and 200 MHz for $f_{res} > 6.2$ GHz. This is often sufficient.

The resonator targeting is influenced by the bare quarter wave resonator frequency and its loading by the feedline as described in Equation (C.5). As such, the parameters of interest are ℓ, C, L, Z_0 and Q_c, where ℓ is the length of the resonator, C the capacitance per unit length, L the total inductance per unit length ,Z_0 the impedance of the resonator and Q_c the coupling quality of the resonator to the feedline. Most importantly is describing the resonator frequency. This is, without coupling to the transmon and the feedline, given by $\omega_{unloaded} = \frac{1}{4\ell\sqrt{LC}}$ where ℓ is the length of the resonator, L is the inductance per unit length of the resonator and C is the capacitance per unit length of the resonator. We assume the feedline impedance to be $Z_{0,feed} = 50\,\Omega$. To use the benefits of impedance matching, we aim for $Z_0 := Z_{0,res} = L/C = 50\,\Omega$. This means that when either C or L is chosen, the other is fixed. Using the calculated L and C, we can change the length to get the targeted resonator frequency.

C.2.1. Abrikosov vortices

With a perpendicular field, Abrikosov vortices might form. The vortices are small traps of flux. These contain a multiple of Φ_0 flux, as dictated by flux quantization. They create additional loss channels in the resonator, degrading readout performance. To prevent these from forming, we make holes in the resonator. The holes in the resonators were designed by J. Assendelft [2]. An additional effect of the fabricated holes is an added kinetic inductance. Since the kinetic inductance goes $\sim \frac{1}{A}$ where A is the cross section of the central strip

[1] Note that in Equation (C.5), we mean 'loaded' to be 'the resonator is coupled to the feedline' and 'unloaded' the opposite, while in Equation (1.4) we mean 'loaded' to be 'the qubit is coupled to the resonator'

of the resonator, creating holes effectively reduces A and increases the kinetic inductance. For all resonator with holes, the value of the kinetic inductance is multiplied by $N_{magic} = 1.1$ to reflect this. For resonators with holes, the measured resonator frequency correspond to the targeted resonator frequency with an error $< 100\,\text{MHz}$, as is visible in Tables E.4 and E.5 and Figure C.2. However, for resonators numbered 12, where no holes are present, the resonator frequency is systematically off by 120 MHz. This is due to the magic number N_{magic} being a catch-all for even non-hole related miscalculations. Since resonator 12 will without holes not be suitable for this thesis' goal of non-zero magnetic fields, we have chosen to include holes into this resonator as well.

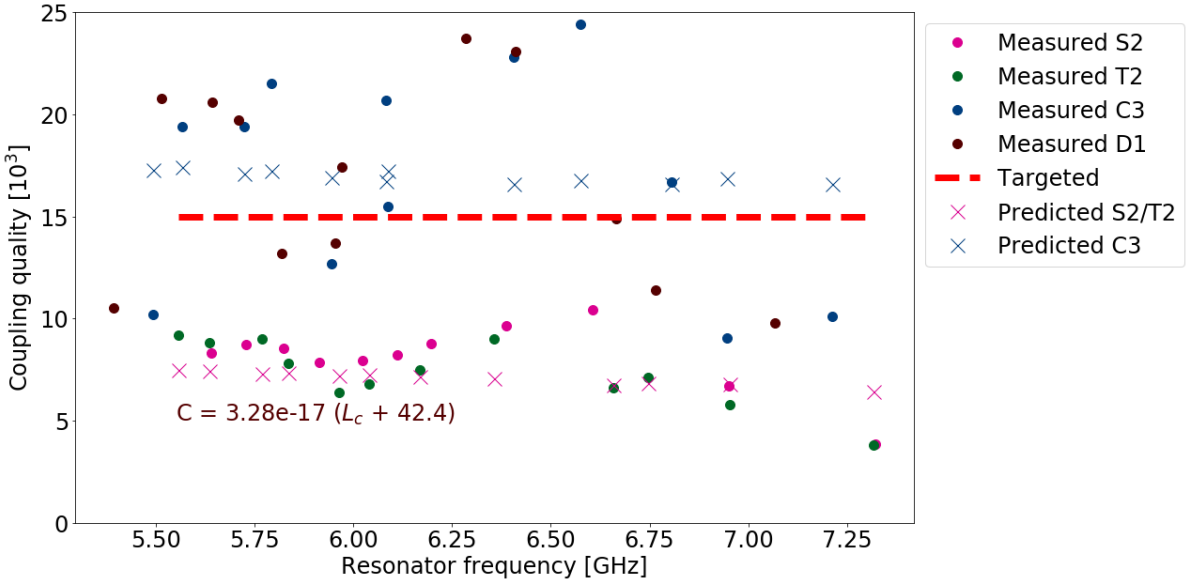

Figure C.3: The measured coupling quality factors of all resonators of four different fabrication cycles. The dashed line indicates the targeted coupling quality. The crosses indicate the predicted values for the quality factor given Equation (C.7) and the values derived for this equation. Chip S2/T2 are made before updating the coupling lengths, Chip C3/D1 were made after updating the coupling quality targeting.

C.3. Targeting the coupling quality

The coupling quality factor Q_c describes the radiation losses of the resonator into the feedline. Increasing the coupling quality increases sensitivity to small resonator frequency shifts, but also increases readout time. For targeting the coupling quality, we can use [35]

$$Q_c = \frac{1}{2}\frac{2\pi}{|S_{31}|^2} = \frac{\pi}{Z_0^2(\omega C)^2} \tag{C.6}$$

where $Z_0 \approx 60 - 70\,\Omega$, $\omega = 2\pi f_{res}$ the resonator frequency, C the capacitance of the resonator to the feed line. This follows an approximate relation:

$$C = A(L_C + L_{C,off}) \tag{C.7}$$

where A is a constant, L_C the length of the elbow coupler parallel to the feedline and $L_{C,off}$ the offset due to the elbow not being accounted for. The current problem is finding the appropriate constants $A, L_{c,off}$. Simulations were made by Marc Beekman giving $A, L_{c,off}$ for certain CPW gap and slot widths for the resonators, the feedline and strip that couples them[4]. However, the exact dimensions used in our chip design were not simulated. Because of that, we extrapolated the values for $A, L_{C,off}$ from all available simulation data and fit it to the measured coupling lengths presented in Tables E.4 and E.5. The extrapolated values are $A = 3.28 \cdot 10^{-17}\,\text{F/m}$ and $L_{C,off} = 42.4\,\mu\text{m}$. We have found that the prediction made by the extrapolated $A, L_{C,off}$ matches the measured Q_c better than its current implementation, as is seen in Figure C.3. This is implemented in the chip design for chips C3 and D1. There is a large fluctuation visible in the measured Q_c. This might be due to the Q_i being lower than expected and interfering with the fitting of the Q_c. We see that

the coupling quality is better on target.

C.4. Finalized chip design

Using the new coupling quality targeting and the programming framework of pyQip3 developed by Marc Beekman, a new chip design using the parameters of Table E.3 was created. The new chip design is shown in Figure C.1. The new resonator targeting values are tabulated in Table E.2.

D

Multiple damped oscillator Ramsey analysis

A typical Ramsey experiment is sensitive to most types of noise or fluctuations. Sometimes, there are two frequencies available due to a strongly coupled TLS switching the qubit frequency during the measurement time. Due to this, our results show a sum decay functions for two differing qubit frequency. These Ramsey experiments can be described by a set of multiple exponentially damped oscillators, one for each qubit frequency:

$$S(t) = \sum_{i=1}^{n} A_i \cos\left(2\pi f_i t + \phi_i\right) \exp(-t/T_i) \tag{D.1}$$

Using Eulers identity, decomposing $\cos\left(2\pi f_i t + \phi_i\right) = \frac{1}{2}\left(e^{i(2\pi f_i t+\phi_i)} + e^{-i(2\pi f_i t+\phi_i)}\right)$ up in exponentials:

$$S(t) = \sum_{i=1}^{n} B_{i,+} \exp\left(\lambda_{i,+} t\right) + B_{i,-} \exp\left(\lambda_{i,-} t\right) \tag{D.2}$$

where $B_{i,+} = \frac{A_i}{2}\exp\left(i\phi_i\right)$,$B_{i,-} = \frac{A_i}{2}\exp\left(-i\phi_i\right)$, $\lambda_{i,+} = 2\pi i f_i - \frac{1}{T_i}$, $\lambda_{i,-} = -2\pi i f_i - \frac{1}{T_i}$.
We now explore the case $n = 2$ of a double exponentially damped oscillator. First of all, when f_1, T_1 and f_2, T_2 are known, we can deduce the A_i and ϕ_i: for every data point $s[m]$ measured at index m,

$$s[m] = \mathbf{v}[m]\mathbf{b}$$

where $\mathbf{v}[m] = [e^{\lambda_{1,+} m\Delta t}, e^{\lambda_{1,-} m\Delta t}, e^{\lambda_{2,+} m\Delta t}, e^{\lambda_{2,-} m\Delta t}]$ and $\mathbf{b} = [B_{1,+}, B_{1,-}, B_{2,+}, B_{2,-}]^T$.
We now create a vector $\mathbf{s} = (s[0], s[1], \ldots, s[m], \ldots)^T$ and a matrix V, where each m'th row is $\mathbf{v}[m]$. We now can create the overdetermined matrix equation

$$\mathbf{s} = V\mathbf{b}$$

and we can estimate $\mathbf{b}$ using least squares

$$\hat{\mathbf{b}} = (V^H V)^{-1} V^H \mathbf{x}$$

We can transform back from $\hat{\mathbf{b}}$ to A_i and ϕ_i through $A_i = 2|B_{i,+}| = 2|B_{i,-}|$ and $\phi_i = \angle B_{i,+} = -\angle B_{i,-}$.

D.1. Finding f_i and T_i

This leaves only the problem of finding f_1, T_1, f_2 and T_2. We use the overview given in [57], using Bertocco's algorithm. However, due to lack of spectral resolution, we will extend this using the ZoomFFT algorithm.
We will start from the Fourier Transform of a discrete (uniformly sampled) signal $x[n]$:

$$X(\Omega) = \sum_{n=1}^{N} x[n] \exp(-i\Omega n) \tag{D.3}$$

If we define $x[n]$ to be: $x[n] = e^{i\phi_i} e^{\lambda n}$ where $\lambda = -D + i\omega = -\frac{1}{T_i} + 2\pi i f_i$:

$$\begin{aligned} X(\Omega) &= \sum_{n=0}^{N-1} e^{i\phi_i} e^{\lambda n} \exp(-i\Omega n) = \sum_{n=0}^{N-1} e^{i\phi_i} e^{-Dn} e^{i\omega n} \exp(-i\Omega n) \\ &= e^{i\phi} \sum_{n=0}^{N-1} \exp(-D + i(\omega - \Omega))^n = e^{i\phi} \frac{1 - \exp(-D + i(\omega - \Omega))^N}{1 - \exp(-D + i(\omega - \Omega))} \\ &= e^{i\phi} \frac{1 - \chi^N e^{-iN\Omega}}{1 - \chi e^{-i\Omega}} \end{aligned} \tag{D.4}$$

where $\chi = \exp(-D + i(\omega)) = \exp(\lambda)$ We can now find the value for a single damped oscillator (using that $e^{-iN\Omega} = 1$)

$$S(\Omega) = \frac{A}{2} \left(\frac{1 - \chi^N}{1 - \chi e^{-i\Omega}} + \frac{1 - \bar{\chi}^N}{1 - \bar{\chi} e^{-i\Omega}} \right) \tag{D.5}$$

where $\bar{\chi} = \exp(-D - i\omega)$.
Our algorithm relies on the fact that we can use ZoomFFT, where we can use several Fast Fourier Transforms (FFTs) to get the DFT for an arbitrary angular frequency Ω. This means that we can find all peaks coarsely in the positive spectrum of an FFT and subsequently zoom in using ZoomFFT for a better resolution. Since around this point $\Omega \approx \omega$, we can neglect the second term of $S(\Omega)$. We can now use a method called Bertocco's algorithm. This method involves defining and finding the ratio

$$R = \frac{X(\Omega + \delta\Omega)}{X(\Omega)} \approx \frac{\frac{A}{2}\left(e^{i\phi} \frac{1-\lambda^N}{1-\lambda e^{-i(\Omega+\delta\Omega)}} \right)}{\frac{A}{2}\left(e^{i\phi} \frac{1-\lambda^N}{1-\lambda e^{-i\Omega}} \right)} = \frac{1 - \lambda e^{-i\Omega}}{1 - \lambda e^{-i(\Omega+\delta\Omega)}} \tag{D.6}$$

such that

$$\chi = e^{i\Omega} \frac{1 - R}{1 - R e^{-\delta\Omega}}. \tag{D.7}$$

Then we can use $D = -\mathrm{Re}\{\ln(\chi)\} = \frac{1}{T_i}$ to find the relaxation time of the oscillator. This is called Bertocco's algorithm.

E

Collection of chip design parameters

Table E.1: Material parameters used to predict the inductance and the capacitance of the coplanar waveguides

Parameter	Value
Material CPW films	NbTiN
CPW thickness t	68 nm
NbTiN T_c at thickness t	13.5 K
NbTiN resistivity ρ at thickness t	0.911 μΩm
Material substrate	Silicon
Permittivity Silicon	11.45

Table E.2: Chosen or calculated parameters for the new chip influencing the resonator targeting, such as length and coupling length influencing the f_{res} and Q_c very strongly. The targeted Q_c is $15 \cdot 10^3$

Resonator nr.	L_{res}[μm]	L_{coup}[μm]	Targeted $f_{res}[GHz]$
1	4384	108.9	5.6
2	4307	106.2	5.7
3	4233	103.6	5.8
4	4161	101.2	5.9
5	4092	98.8	6.0
6	4025	96.5	6.1
7	3960	94.2	6.2
8	3836	89.9	6.4
9	3720	85.9	6.6
10	3610	82.1	6.8
11	3507	78.6	7.0
12	3409	75.2	7.2

Table E.3: Dimensions of the chip design. All these values were used to verify the dimensions in the .gds files in which the design is saved.

Parameter	Value[μm]
Chip width	7000
Chip height	2300
Min dist of structures to chip edge	250
Feedline center strip width	12
Feedline gap width	2.3
Feedline edge strip width	4
Resonator center strip width	12
Resonator gap width	6
Resonator edge strip width	4
Bias line center strip width	12
Bias line gap width	2.3
Bias edge strip width	2
Minimum curve radius	60
Strip width coupling feedline and resonator	1
Strip width coupling resonator and qubit	1
Straight length along resonator-qubit coupling	315
Lattice constant 'Abrikosov' holes	0.5
Radius 'Abrikosov' holes	0.05

Table E.4: Chosen or calculated parameters influencing the resonator targeting, such as length and coupling length influencing the f_{res} and Q_c very strongly. The measured values of S2 are given in this table. The targeted Q_c is $15 \cdot 10^3$

Resonator nr.	L_{res}[μm]	L_{coup}[μm]	Targeted $f_{res}[GHz]$	$f_{res}[GHz]$ S2	$Q_c[10^3]$ S2	$Q_i[10^5]$ S2
1	4378	185	5.6	5.641	8.31	1.5
2	4301	182	5.7	5.728	8.73	1.82
3	4226	179	5.8	5.823	8.55	5.73
4	4155	176	5.9	5.914	7.86	3.69
5	4085	173	6.0	6.024	7.95	0.76
6	4018	170	6.1	6.112	8.20	2.49
7	3952	167	6.2	6.197	8.76	1.0
8	3829	162	6.4	6.388	9.64	3.1
9	3713	157	6.6	6.607	10.42	0.59
10	3603	153	6.8	n.a.	n.a.	n.a.
11	3500	148	7.0	6.950	6.71	0.46
12 (no holes)	3346	144	7.2	7.323	3.85	2.7

Table E.5: Chosen or calculated parameters influencing the resonator targeting, such as length and coupling length influencing the f_{res} and Q_c. The measured values for chip T2 are given in this table. The targeted Q_c is $15 \cdot 10^3$

Resonator nr.	L_{res}[μm]	L_{coup}[μm]	Targeted $f_{res}[GHz]$	$f_{res}[GHz]$ T2	$Q_c[10^3]$ T2	$Q_i[10^5]$ T2
1	4378	185	5.6	5.557	9.2	1.68
2	4301	182	5.7	5.6368	8.8	0.58
3	4226	179	5.8	5.770	9.0	2.15
4	4155	176	5.9	5.836	7.8	0.47
5	4085	173	6.0	5.963	6.4	0.84
6	4018	170	6.1	6.04	6.8	0.11
7	3952	167	6.2	6.169	7.5	0.92
8	3829	162	6.4	6.356	9.0	0.89
9	3713	157	6.6	6.657	6.6	0.41
10	3603	153	6.8	6.767	7.1	0.083
11	3500	148	7.0	6.953	5.8	1.68
12 (no holes)	3346	144	7.2	7.318	3.8	0.18

Table E.6: Parameters and dimensions of other structures on the chip.

Parameter	Dimension [μm]
Transmon pad width	400
Transmon pad height	100
Width of finger	20
Width between fingers	20
Finger curve radius	30
Height of finger from base	60
Height from edge to base	10
Right finger middle to JJ attach block	50
JJ attach block width	10
JJ attach block height	20
JJ attach inner curve	5
JJ attach tip curve	2.5
Pad edge curve radius	5
Edge of transmon pads to edge strip	20
Edge strip width	5
Edge strip inner curve radius	20
Edge strip outer curve radius	25

Table E.7: Airbridge parameters. * indicates that the CPW must be included and a value of $2g + w$ must be added, where g is the gap width and w the strip width. This is 24 μm for the chosen resonator CPW and 16.6 μm for the feedline and bias line CPWs.

Parameter	Dimension[μm]
Airbridge width	30
Airbridge base height*	71
Airbridge rounding radius	15
Safe region width	170
Safe region base height*	100
Safe region gap width	20
Safe region gap base height*	90

F

Derivation of the spin-fluctuator spectrum

To model the effects happening to the spin particle, we assume a Markovian (memory-less) process. The spin particle is represented by being in the x_+ state or in the x_- state. When it is in the x_+-state, it has a probability of transitioning to the x_--state and vice versa. We call $\Gamma_\downarrow = \frac{1}{\langle t_- \rangle}$ the transition rate from x_+ to x_-. This system is also called random telegraph noise system (RTN). To find the power spectral density of this system, we want to find the autocorrelation function of this process.
The autocorrelation is defined as $r_{xx}(t) = \langle x(t)x(0) \rangle$ for stationary signal. The autocorrelation $r_{xx}(\tau)$ for a RTN is a measure of how long it will stay in (or transition back to) the same state. If we define the lower state $x_\downarrow = a$ and the higher state $x_\uparrow = b$, we can reason to find

$$r_{xx}(\tau) = a^2 P_\downarrow(0) P_{\downarrow\downarrow}(t) + ab(+) + b^2 P_\uparrow(0)(P_{\uparrow\uparrow}(t)) + ab(P_\uparrow(0)P_{\uparrow\downarrow}(t) + P_\downarrow(0)P_{\downarrow\uparrow}) \tag{F.1}$$

where $P_\downarrow(0)$ is the probability that the spin can initially be found in the x_- state and $P_\uparrow(0)$ to be found in the x_+-state. $P_{\uparrow\downarrow}(t)$ is the probability that we will find the state in the x_- state at time t, when we initially were in the x_+ state. Similar for $P_{\uparrow\uparrow}(t), P_{\downarrow\uparrow}(t), P_{\downarrow\downarrow}(t)$.
To find e.g. $P_{\uparrow\uparrow}(t)$, we will want to know the probability of a transition happening away or towards the x_+ state. We see that $P_{\uparrow\uparrow}(t)$ increases in time interval dt with rate $P_{\uparrow\downarrow}(t)\Gamma_\uparrow dt$ and decreases in the time interval with rate $P_{\uparrow\uparrow}(t)\Gamma_\downarrow dt$. We can find thus find the total change in a time interval dt:

$$P_{\uparrow\uparrow}(t+dt) = P_{\uparrow\uparrow}(1-\Gamma_\downarrow dt) + P_{\uparrow\downarrow}\Gamma_\uparrow dt \tag{F.2}$$

which in the limit $dt \to 0$ is

$$\frac{dP_{\uparrow\uparrow}}{dt} = \Gamma_\uparrow - P_{\uparrow\uparrow}(\Gamma_\uparrow + \Gamma_\downarrow) \tag{F.3a}$$

We can do the same procedure for the other probabilities:

$$\frac{dP_{\uparrow\downarrow}}{dt} = \Gamma_\downarrow - P_{\uparrow\downarrow}(\Gamma_\uparrow + \Gamma_\downarrow) \tag{F.3b}$$

$$\frac{dP_{\downarrow\uparrow}}{dt} = \Gamma_\uparrow - P_{\downarrow\uparrow}(\Gamma_\uparrow + \Gamma_\downarrow) \tag{F.3c}$$

$$\frac{dP_{\downarrow\downarrow}}{dt} = \Gamma_\downarrow - P_{\downarrow\downarrow}(\Gamma_\uparrow + \Gamma_\downarrow) \tag{F.3d}$$

Using initial conditions $P_{\uparrow\uparrow}(t=0) = 1$, $P_{\downarrow\uparrow}(t=0) = 0$ and similar for the others:

$$P_{\uparrow\uparrow} = \frac{\Gamma_\downarrow}{\Gamma_\downarrow + \Gamma_\uparrow} e^{-(\Gamma_\uparrow + \Gamma_\downarrow)t} + \frac{\Gamma_\uparrow}{\Gamma_\uparrow + \Gamma_\downarrow} \tag{F.4a}$$

$$P_{\downarrow\uparrow} = -\frac{\Gamma_\uparrow}{\Gamma_\uparrow + \Gamma_\downarrow} e^{-(\Gamma_\uparrow + \Gamma_\downarrow)t} + \frac{\Gamma_\uparrow}{\Gamma_\uparrow + \Gamma_\downarrow} \tag{F.4b}$$

$$P_{\uparrow\downarrow} = -\frac{\Gamma_\downarrow}{\Gamma_\uparrow + \Gamma_\downarrow} e^{-(\Gamma_\uparrow + \Gamma_\downarrow)t} + \frac{\Gamma_\downarrow}{\Gamma_\uparrow + \Gamma_\downarrow} \tag{F.4c}$$

$$P_{\downarrow\downarrow} = \frac{\Gamma_\uparrow}{\Gamma_\uparrow + \Gamma_\downarrow} e^{-(\Gamma_\uparrow+\Gamma_\downarrow)t} + \frac{\Gamma_\downarrow}{\Gamma_\uparrow + \Gamma_\downarrow} \tag{F.4d}$$

We use the fact that P_+ is the same as the average fraction that the RTN system resides in the x_+-state.

$$P_+ = \frac{\tau_+}{\tau_- + \tau_+} = \frac{\Gamma_\uparrow}{\Gamma_\uparrow + \Gamma_\downarrow} \tag{F.5a}$$

$$P_- = 1 - P_+ = \frac{\Gamma_\downarrow}{\Gamma_\uparrow + \Gamma_\downarrow} \tag{F.5b}$$

using that we defined $\Gamma_\uparrow = \frac{1}{\tau_-}$ and $\Gamma_\downarrow = \frac{1}{\tau_+}$. To gain more insight, we also calculate the time dependencies of $P_+(t)$ and $P_-(t)$, following the same intuition as in Equation (F.2). We find

$$P_+(t) = \left(P_+(0) - \frac{\Gamma_\uparrow}{\Gamma_\uparrow + \Gamma_\downarrow}\right) e^{-(\Gamma_\uparrow+\Gamma_\downarrow)t} + \frac{\Gamma_\uparrow}{\Gamma_\uparrow + \Gamma_\downarrow} \tag{F.6a}$$

$$P_-(t) = \left(P_-(0) - \frac{\Gamma_\downarrow}{\Gamma_\uparrow + \Gamma_\downarrow}\right) e^{-(\Gamma_\uparrow+\Gamma_\downarrow)t} + \frac{\Gamma_\downarrow}{\Gamma_\uparrow + \Gamma_\downarrow} \tag{F.6b}$$

We could now simplify Equations (F.4).
Now we investigate, using that we define $a := x_\downarrow$ and $b := x_\uparrow$ and substitute the found equations in (F.1):

$$r_{xx}(t) = a^2 P_\downarrow (P_\uparrow e^{-(\Gamma_\uparrow+\Gamma_\downarrow)t} + P_\downarrow) + ab(P_\uparrow(-P_\downarrow e^{-(\Gamma_\uparrow+\Gamma_\downarrow)t} + P_\downarrow) + P_\downarrow(-P_\uparrow e^{-(\Gamma_\uparrow+\Gamma_\downarrow)t} + P_\uparrow)) + b^2 P_\uparrow (P_\downarrow e^{-(\Gamma_\uparrow+\Gamma_\downarrow)t} + P_\uparrow) \tag{F.7}$$

This all can be simplified to

$$r_{xx}(\tau) = (a-b)^2 P_\uparrow P_\downarrow e^{-(\Gamma_\uparrow+\Gamma_\downarrow)t} + (aP_\downarrow + bP_\uparrow)^2 \tag{F.8}$$

Since this is a classical system $r_{xx}(t) = r_{xx}(-t)$, meaning that we substitute $t \to |t|$.
To simplify the derivation and come closer to our fluctuator system, we will use $a = -S$ and $b = S$. We get:

$$r_{xx}(\tau) = 4S^2 \frac{\Gamma_\uparrow \Gamma_\downarrow}{(\Gamma_\uparrow + \Gamma_\downarrow)^2} e^{-(\Gamma_\uparrow+\Gamma_\downarrow)t} + S^2 \left(\frac{\Gamma_\downarrow - \Gamma_\uparrow}{\Gamma_\downarrow + \Gamma_\uparrow}\right)^2 \tag{F.9}$$

Using the definition for the power spectral density $S_S(f) = \int_{-\infty}^{\infty} e^{2\pi i f t} r_{xx}(t)\,dt$ we get

$$S(f) = 4S^2 \frac{\Gamma_\uparrow \Gamma_\downarrow}{(\Gamma_\uparrow + \Gamma_\downarrow)^2} \frac{2(\Gamma_\uparrow + \Gamma_\downarrow)}{(\Gamma_\uparrow + \Gamma_\downarrow)^2 + (2\pi f)^2} + S^2 \left(\frac{\Gamma_\uparrow - \Gamma_\downarrow}{(\Gamma_\uparrow + \Gamma_\downarrow)}\right)^2 \delta(f) \tag{F.10}$$

where $\delta(f)$ is the Dirac delta distribution.
Now we introduce the physical side of the derivation. We are investigating a spin system in thermal equilibrium, so we can apply Boltzmann statistics. We will use the Zeeman Hamiltonian (4.5) to find the rates of a fluctuator. The energy levels of a $s = \frac{1}{2}$-system are $\pm\frac{g\mu_s B}{2}$. We define now $\tilde{B} = E_Z / k_B T = \frac{g\mu_S B}{2k_B T}$ for convenience. We can now find the canonical partition function

$$\mathcal{Z} = \exp(-\tilde{B}) + \exp(\tilde{B}) \tag{F.11}$$

Now we can find the probability of find a spin in the up state (which we define to be parallel to the magnetic field, and as such a higher energy):

$$P_\uparrow = \frac{\exp(\tilde{B})}{\mathcal{Z}} \tag{F.12a}$$

$$P_\downarrow = \frac{\exp(-\tilde{B})}{\mathcal{Z}} \tag{F.12b}$$

We now find the values of $\Gamma_\uparrow, \Gamma - \downarrow$ through Equations (F.5) and (F.12).

$$\Gamma_\downarrow = \Gamma P_\downarrow = \Gamma \exp(-\tilde{B}) \tag{F.13a}$$

$$\Gamma_\uparrow = \Gamma P_\uparrow = \Gamma \exp(\tilde{B}) = \Gamma_\downarrow \exp(-2\tilde{B}) \tag{F.13b}$$

where $\Gamma = \Gamma_\downarrow + \Gamma_\uparrow$ We now substitute $S = \frac{1}{2}$ and all Equations found above to find the eventual power spectral density of a spin-1/2 fluctuator

$$S(f) = \frac{1}{\cosh(\tilde{B})} \frac{\exp(-\tilde{B})\Gamma_\downarrow}{(2\exp(-\tilde{B})\cosh(\tilde{B})\Gamma_\downarrow)^2 + (2\pi f)^2} + \frac{1}{4}\tanh^2(\tilde{B})\delta(f) \tag{F.14}$$

G

Derivation of the linear spectrum contributions of the spin PSD

To find the power spectral density for Φ from spin fluctuations, we will start with equation (4.1) and try to find the autocorrelation function of $\langle\Phi(t)\Phi(0)\rangle$ through

$$\langle\Phi(t)\Phi(0)\rangle = \left\langle \left(\sum_n \mathbf{F}(\mathbf{R}_n)\cdot\mathbf{s}_n(t)\right)\left(\sum_m \mathbf{F}(\mathbf{R}_m)\cdot\mathbf{s}_m(0)\right)\right\rangle \tag{G.1}$$

Now we assume that the interaction between spins s_n and s_m is zero if $n \neq m$ (meaning there are no spin-spin interactions whatsoever) and the spins are independent. We can simplify

$$\langle\Phi(t)\Phi(0)\rangle = \left\langle \sum_n\sum_m \left(\mathbf{F}(\mathbf{R}_n)\cdot\mathbf{s}_n(t)\right)\left(\mathbf{F}(\mathbf{R}_m)\cdot\mathbf{s}_m(0)\right)\delta_{nm}\right\rangle = \left\langle \sum_n \left(\mathbf{F}(\mathbf{R}_n)\cdot\mathbf{s}_n(t)\right)\left(\mathbf{F}(\mathbf{R}_n)\cdot\mathbf{s}_n(0)\right)\right\rangle \tag{G.2}$$

Using Equation (G.2) in (4.2) we find

$$S_\Phi(f) = \int df e^{2\pi i f t}\sum_n \langle\left(\mathbf{F}(\mathbf{R}_n)\cdot\mathbf{s}_n(t)\right)\left(\mathbf{F}(\mathbf{R}_n)\cdot\mathbf{s}_n(0)\right)\rangle \tag{G.3}$$

working out the dot products for 3 dimensions $\hat{x},\hat{y},\hat{z}$ (considering the magnetic field direction later to be $\hat{z}$):

$$S_\Phi(f) = \int df e^{2\pi i f t}\sum_{\alpha,\beta=x,y,z}\sum_n F_\alpha(\mathbf{R}_n)F_\beta(\mathbf{R}_n)\left\langle s_{n,\alpha}(t)s_{n,\beta}(0)\right\rangle \tag{G.4}$$

realizing that $\left\langle s_{n,\alpha}(t)s_{n,\beta}(0)\right\rangle$ is the same for every independent and identical spin:

$$S_\Phi(f) = \int df e^{2\pi i f t}\sum_{\alpha,\beta=x,y,z}\sum_n F_\alpha(\mathbf{R}_n)F_\beta(\mathbf{R}_n)\left\langle s_\alpha(t)s_\beta(0)\right\rangle \tag{G.5}$$

Now taking the continuum limit $\sum_n F(\mathbf{R}_n) \to \int d^3\mathbf{R}F(\mathbf{R})\sigma(\mathbf{R})$ (which we could transform back by $\sigma(\mathbf{R}) = \sum_n \delta(\mathbf{R}-\mathbf{R}_n)$):

$$S_\Phi(f) = \iint df d^3\mathbf{R}\sigma(\mathbf{R})e^{2\pi i f t}\sum_{\alpha,\beta=x,y,z} F_\alpha(\mathbf{R})F_\beta(\mathbf{R})\left\langle s_\alpha(t)s_\beta(0)\right\rangle \tag{G.6}$$

Now we can find the spin power spectral densities or cross spectral densities using $S_{\alpha\beta}(f) = \int df e^{2\pi i f t}\left\langle s_\alpha(t)s_\beta(0)\right\rangle$ and we find

$$S_\Phi(f) = \int d^3\mathbf{R}\sigma(\mathbf{R})\sum_{\alpha,\beta=x,y,z} F_\alpha(\mathbf{R})F_\beta(\mathbf{R})S_{\alpha\beta}(f) = \sum_{\alpha,\beta=x,y,z} S_{\alpha\beta}(f)\int d^3\mathbf{R}\sigma(\mathbf{R})F_\alpha(\mathbf{R})F_\beta(\mathbf{R}) \tag{G.7}$$

We define now a total direct spin-to-SQUID coupling using

$$C_{\alpha\beta} := \int d^3\mathbf{R}\sigma(\mathbf{R})F_\alpha(R)F_\beta(R) \tag{G.8}$$

so that we find, all written out:

$$S_\Phi(f) = \sum_{\alpha,\beta=x,y,z} C_{\alpha\beta} S_{\alpha\beta}(f) \tag{G.9}$$

$$\begin{aligned} &= C_{xx}S_{xx}(f) + C_{yy}S_{yy}(f) + C_{zz}S_{zz}(f) + C_{xy}(S_{xy}(f) + S_{yx}(f)) \\ &\quad + C_{xz}(S_{xz}(f) + S_{zx}(f)) + C_{yz}(S_{yz}(f) + S_{zy}(f)) \end{aligned} \tag{G.10}$$

where we see that the flux noise spectral density can be written as the weighted sum of the spin spectral densities for all combinations of basis components.

H

Derivation of the Flux vector F

First of all, we can determine the flux added by one single spin $\mathbf{s}_n$ by considering the vector potential $\mathbf{A}_n$ that a electron undergoes while traveling on a closed loop around the SQUID. We need to sum over all possible closed loops

$$\Phi_n = \sum_{\mathscr{C}} \oint_{\mathscr{C}} A_n(r) \cdot d\ell \tag{H.1}$$

If we suppose that the current flows entirely in the direction of the wire, we find that $\sum_{\mathscr{C}} \oint_{\mathscr{C}} d\ell \rightarrow \iiint d^3 r J_{SC}(\mathbf{r})$ so that

$$\Phi_n = \iiint d^3\mathbf{r}\mathbf{A}_n(\mathbf{r}) \cdot \frac{J_{SC}(\mathbf{r})}{I_{tot}} \tag{H.2}$$

Now we find the equation for $\mathbf{A}_n$ using the spin-dipole expression for very small magnetic dipoles:

$$\boldsymbol{A}_n(\boldsymbol{r}) = -\frac{g\mu_s\mu_0}{4\pi} \frac{\boldsymbol{s}_n \times (\boldsymbol{r} - \boldsymbol{R}_n)}{|\boldsymbol{r} - \boldsymbol{R}_n|^3}$$

By supposing $\Phi_n = \mathbf{F}(\mathbf{R}) \cdot \mathbf{s}_n$ and using basic vector calculus identities, we find the resulting expression for $\mathbf{F}$.

$$\mathbf{F}(\mathbf{R}) = \frac{g\mu_s\mu_0}{4\pi} \nabla_{\boldsymbol{R}} \times \left[\int d^3 r \frac{\boldsymbol{J}_{\mathrm{SC}}(\boldsymbol{r})}{I_{\mathrm{SC}}|\boldsymbol{r} - \boldsymbol{R}|} \right] \tag{H.3}$$

For thin films, we can find $\boldsymbol{J}_{SC}$ analytically [15] when $b \leq \lambda, \tilde{\lambda} = \frac{\lambda^2}{bW} \ll 1$ and $\xi_{SC} \ll W$ where λ is the magnetic penetration depth, b is the thickness of the film, W is the width of the film and ξ_{SC} is the superconducting coherence length of the film. The solution reads

$$\boldsymbol{J}_{\mathrm{SC}}(\boldsymbol{r}) = \frac{2I_{\mathrm{SC}}}{\pi b W(1 - \gamma\sqrt{2\tilde{\lambda}})} \hat{\boldsymbol{v}} \times \begin{cases} \frac{1}{\sqrt{2\lambda}} \mathrm{e}^{-\frac{(1-\tilde{\lambda}-|u|)}{2\lambda}} & \text{for } (1-\tilde{\lambda}) < |u| \leqslant 1 \\ \frac{1}{\sqrt{1-u^2}} & \text{for } |u| \leqslant (1-\tilde{\lambda}) \end{cases} \tag{H.4}$$

where $\gamma = 2\left(2 - \mathrm{e}^{1/2}\right)/\pi = 0.2236$ and $u = 2x/W$. Now we can find the values of $\mathbf{F}$ inside, outside and on the wire surface. Using these values, we can find:

$$F_u(R_u, R_w) = -\frac{g\mu_s\mu_0 W}{8\pi} \int_{-1}^{1} dp \left\{ \frac{J_{\mathrm{SC}}(p)}{I_{\mathrm{SC}}} \ln\left[\frac{(x-R_u)^2 + R_w^2}{(x-R_u)^2 + (R_w+b)^2} \right] \right\} \tag{H.5a}$$

$$F_v(R_u, R_w) = 0 \tag{H.5b}$$

$$F_w(R_u, R_w) = \frac{g\mu_s\mu_0 W}{4\pi} \int_{-1}^{1} dp \left\{ \frac{J_{\mathrm{SC}}(p)}{I_{\mathrm{SC}}} \left[\arctan\left(\frac{R_w + b}{x - R_u} \right) - \arctan\left(\frac{R_w}{x - R_u} \right) \right] \right\} \tag{H.5c}$$

Derivation of the ensemble of spin fluctuators PSD

We start by looking at a general formula for the single fluctuator spectrum

$$S_{single} = g(\tilde{B}) \frac{\Gamma_i}{\Gamma_i^2 + h(\tilde{B})^2 (2\pi f - 2\pi f_0)^2} \tag{I.1}$$

where Γ_i are $\Gamma_\uparrow, \Gamma_\downarrow$ or Γ_{avg}, depending on use case, $g(\tilde{B})$ is any function of $\tilde{B}$, and $h(\tilde{B})$ a function of $\tilde{B}$ such that we can write Γ_i as one of the desired rates to integrate over. We suppose that the probability distribution goes as $P(\Gamma_i) = \frac{A}{\Gamma_i}$ and has a minimum and maximum flipping rate Γ_{min} and Γ_{max} such that $A = \frac{1}{\ln\left(\frac{\Gamma_{max}}{\Gamma_{min}}\right)}$. We then can solve for an ensemble of different fluctuators:

$$\begin{aligned} S_{ens} &= \int_{\Gamma_{min}}^{\Gamma_{max}} P(\Gamma_i) g(\tilde{B}) \frac{\Gamma_i}{\Gamma_i^2 + h(\tilde{B})^2 (2\pi f - 2\pi f_0)^2} d\Gamma_i = A g(\tilde{B}) \int_{\Gamma_{min}}^{\Gamma_{max}} \frac{d\Gamma_i}{\Gamma_i^2 + h(\tilde{B})^2 (2\pi f - 2\pi f_0)^2} \\ &= A \frac{g(\tilde{B})}{h(\tilde{B})(2\pi f - 2\pi f_0)} \left[\arctan\left(\frac{\Gamma_{max}}{h(\tilde{B})(2\pi f - 2\pi f_0)} \right) - \arctan\left(\frac{\Gamma_{min}}{h(\tilde{B})(2\pi f - 2\pi f_0)} \right) \right]. \end{aligned} \tag{I.2}$$

If the maximum (minimum) flipping rates are higher (lower) than typical frequencies $h(\tilde{B})2\pi f, h(\tilde{B}) f_Z$, we can take the limit $\left[\arctan\left(\frac{\Gamma_{max}}{h(\tilde{B})(2\pi f - 2\pi f_0)} \right) - \arctan\left(\frac{\Gamma_{min}}{h(\tilde{B})(2\pi f - 2\pi f_0)} \right) \right] = \pi/2$ to find

$$S_{ens}(f) = \frac{\pi}{2\ln\left(\frac{\Gamma_{max}}{\Gamma_{min}}\right)} \frac{g(\tilde{B})}{h(\tilde{B})(2\pi f - 2\pi f_0)} \tag{I.3}$$

For S_{zz}, integrating over $\Gamma_\downarrow$ we have $g(\tilde{B}) = \frac{1}{2\cosh^2(\tilde{B})(1+\exp(-2\tilde{B}))}$ and $h(\tilde{B}) = \frac{1}{1+\exp(-2\tilde{B})}$ and $f_0 = 0$. We find that

$$S_{zz}(f) = \frac{1}{\ln\left(\frac{\Gamma_{max}}{\Gamma_{min}}\right)} \frac{1}{2\cosh^2(\tilde{B})(2\pi f)} \left[\arctan\left(\frac{\Gamma_{max}(1+\exp(-2\tilde{B}))}{(2\pi f)} \right) - \arctan\left(\frac{\Gamma_{min}(1+\exp(-2\tilde{B}))}{(2\pi f)} \right) \right]. \tag{I.4}$$

Similarly for $S_{xx}(f)$ with $g(\tilde{B}) = \frac{1}{4} \frac{2}{(1+\exp(-2\tilde{B}))}$, $h(\tilde{B}) = \frac{2}{(1+\exp(-2\tilde{B}))}$, $f_0 = 2f_Z/2\pi$, we find:

$$S_{xx}(f) = \left(\frac{1}{4}\right)^2 \frac{1}{\ln\left(\frac{\Gamma_{max}}{\Gamma_{min}}\right)} \frac{1}{(2\pi f - 2f_Z)} \left[\arctan\left(\frac{\Gamma_{max} \frac{(1+\exp(-2\tilde{B}))}{2}}{(2\pi f - 2f_Z)} \right) - \arctan\left(\frac{\Gamma_{min} \frac{(1+\exp(-2\tilde{B}))}{2}}{(2\pi f - 2f_Z)} \right) \right]. \tag{I.5}$$

J

Magnet use: issues and step-by-step checklist

Since the installation of the AMI 430 Programmer and first uses, we have run into problems. There are three main issues:

1. The programmer supplying a voltage to the current source without reason, sourcing a current and heating up the fridge until the He-mix is all evaporated.
2. The magnet current source ramping to the wrong current (by ~ 1%)
3. Small oscillations of the current/field after ramping

The first problem is very pressing. We found that the source of these problem was the AMI430 programmer applying a large undesired charging voltage to the current source. This was found to be feedback from the AMI430 programmer to the magnet voltage measured by the magnet voltage probes. For example: if the magnet voltage probes measure a large voltage (meaning the current through the magnet changes rapidly), the AMI430 tries to counteract this by supplying a countercurrent. A faulty probe could unintentionally cause a big current in this way. Another failure mode is the voltage probe reading 0 V while the current is ramping. The AMI430 programmer might interpret this as the magnet not reacting, and as such tries to increase the current by using a higher charging voltage, while the current is already increasing. The solution to this problem is disconnecting the voltage probes such that a high resistance is measured. The AMI430 recognizes this and as a result, the probes will not be used for control.
The second problem: the unknown offset from the desired field can be traced back to the 'Paused'-mode of the AMI430 programmer. This mode is intended as pausing ramping and keeping the current/field the same as the last measurement. However, this mode creates an offset from the desired field ~ 0.5 mT, even while in steady state on a field. The solution is to use the 'Paused' mode as little as possible.
The last problem, the oscillations, can be found in Figure J.1. This can be attributed to the rate at which the field is changing. The characteristic time of the magnet to reach its desired value is $t_{RL} = \frac{R}{L}$ where R and L is the total resistance of the circuit and L the inductance of the magnet. We could find that by lowering the ramping rate of the magnet, these oscillations disappeared.

To ensure a good initialization of the magnet system, I have prepared a small step-by-step checklist on initializing the magnets using the AMI 430 programmer and AMI power supply:

If the current lead of the AMI power supply are not yet connected to the fridge:
1. Make sure the magnet leads are disconnected , the power supply is off and the Persistent Switch Heaters are off.
2. Turn on the AMI 430 Programmer, connect it using LAN and check the settings using the asserts in AMI power supply init python file.
3. Turn off the AMI 430 programmer.
4. Connect magnet leads.

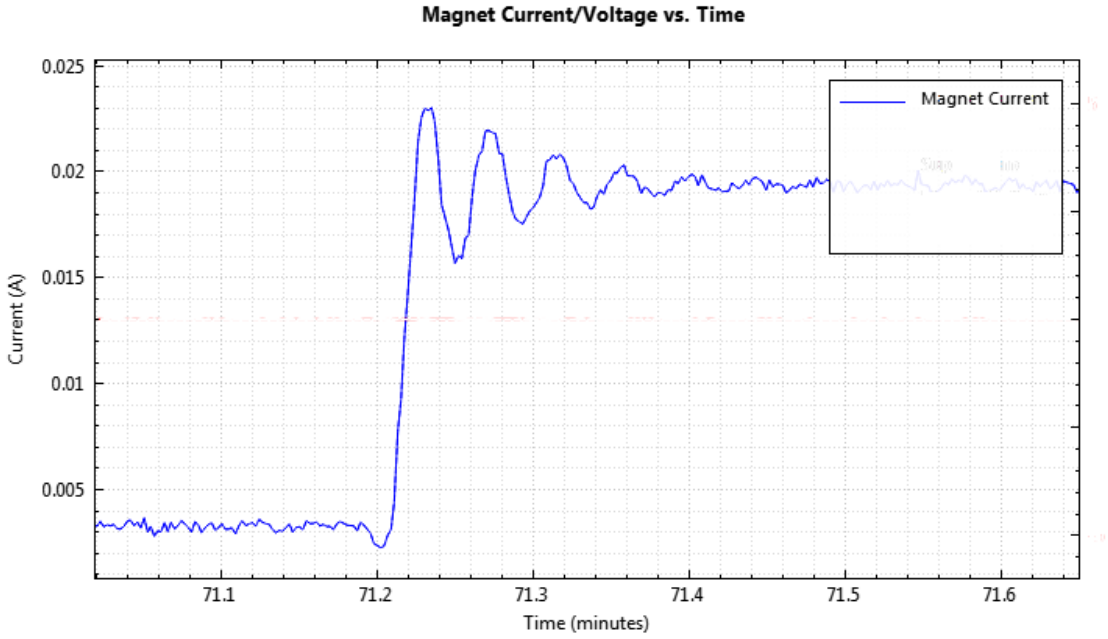

Figure J.1: Ramping the magnet from $I = 4\,\text{mA}$ to $I = 20\,\text{mA}$. We see that at the end of the ramp, the current oscillates. This is due to the RL-circuit having a delay (on the characteristic time scale R/L) and the AMI430 programmer trying to correct for it.

If the current leads are connected:
1. Make sure the magnet leads are connected, the power supply is off and the Persistent Switch Heaters are off.
2. Make sure the voltage probes are not connected and feel an open (connecting them to the matrix module on the 'GND' or 'Open' mode still makes a connection).
3. Turn on the AMI 430 Programmer, connect it using LAN.
4. Check the programmer settings using the asserts in ' AMI power supply init' python file and see if they compare to the datasheet.
5. Start up the data acquisition software (Magnet DAQ) supplied by AMI to get continuous programmer data for better debugging.
6. Check if the Persistent Switch Heaters are switched from 'Ground' to 'Measured' on the IVVI rack.
7. With the persistent switch heaters still off, turn on the AMI Power supply.
8. Ramp to zero if necessary.

If this is the first time the persistent switch heaters are activated after condensation:
1. Turn on Persistent Switch Heater Z and wait until the fridge pressures are stable.
2. Turn off the Persistent Switch Heater Z and make sure the field is zero.
3. Turn on Persistent Switch Heater Y and wait until the fridge pressures are stable.
4. Turn off the Persistent Switch Heater Y and make sure the field is zero.

If we have already turned on the persistent switch heaters once after condensation:
9. Turn on both Persistent Switch Heaters one after another.